NTNU – Trondheim
Norwegian University of
Science and Technology

Nonlinear Hydrodynamic Effects for Bottom-Fixed Wind Turbines

Even Rosenlund

Marine Technology
Submission date: June 2013
Supervisor: Marilena Greco, IMT

Norwegian University of Science and Technology
Department of Marine Technology

NTNU Trondheim
Norwegian University of Science and Technology
Faculty of Engineering Science and Technology
Department of MarineTechnology

MASTER THESIS IN MARINE TECHNOLOGY

SPRING 2013

FOR

Even Rosenlund

Nonlinear Hydrodynamic Effects for Bottom-Fixed Wind Turbines
(Ikkelinære hydrodynamiske effekter på bunnfaste offshore vindturbiner)

The need for alternative and greener energy is pushing toward greater investment on offshore wind turbines. Bottom-fixed wind turbines and floating wind turbines on spar, semi-submersible, and tension leg platforms represent relevant concepts and involve important challenges. Several arrangements for intermediate and deeper water depths are presently being examined. Aero-hydro-elastic coupling is in general of great concern. For bottom-fixed wind turbines in shallow water conditions a well recognized challenge in terms of safety and efficiency is represented by the interaction with very steep waves, especially when impacting as breaking waves against the cylindrical part of the platform. An important consequence could be ringing excitation, i.e. global transient elastic resonance oscillations of the structure. In the project, the hydrodynamic challenges connected with the general concept of offshore wind turbines were examined with focus on the concept of bottom-fixed platforms and their interaction with waves.

Objective
The aim of the thesis is to investigate the relevance of nonlinear wave loads on a bottom-fixed wind turbine. This will be done for the platform selected in the project thesis and within the FAST open-source solver. Both the influence of nonlinear effects in the wave-load formulas and in the incident waves will be examined.

The work should be carried out in steps as follows:

1. Summarize major findings from the project thesis in the context of bottom-fixed wind turbines highlighting the nonlinear wave induced-load effects relevant for the structure.
2. Select one or more improved wave-load models examined in the project thesis and implement them in FAST. Assume linear incident waves and compare the resulting loads against those obtained using the classical Morison equations for relevant operational conditions of the platform.
3. Use an available fully nonlinear incident wave solution, and/or a weakly-nonlinear incident wave solution, as input for the implemented wave loads and check the relevance of nonlinear effects in the sea.
4. Using the improved incident-wave and wave-load models, investigate occurrence and features of ringing for the selected platform.
5. Assess the improved solver by comparing with results from fully-nonlinear numerical solvers or experiments on a circular cylinder.

The work may show to be more extensive than anticipated. Some topics may therefore be left out after discussion with the supervisor without any negative influence on the grading.

The candidate should in her report give a personal contribution to the solution of the problem formulated in this text. All assumptions and conclusions must be supported by mathematical models and/or references to physical effects in a logical manner.

The candidate should apply all available sources to find relevant literature and information on the actual problem.

The thesis should be organised in a rational manner to give a clear presentation of the work in terms of exposition of results, assessments, and conclusions. It is important that the text is well written and that tables and figures are used to support the verbal presentation. The thesis should be complete, but still as short as possible. In particular, the text should be brief and to the point, with a clear language. Telegraphic language should be avoided.

The thesis must contain the following elements: the text defining the scope (i.e. this text), preface (outlining project-work steps and acknowledgements), abstract (providing the summary), table of contents, main body of thesis, conclusions with recommendations for further work, list of symbols and acronyms, references and (optional) appendices. All figures, tables and equations shall be numerated.

The supervisor may require that the candidate, in an early stage of the work, present a written plan for the completion of the work. The plan should include budget for the use of computer and laboratory resources that will be charged to the department. Overruns shall be reported to the supervisor.

From the thesis it should be possible to identify the work carried out by the candidate and what has been found in the available literature. It is important to give references to the original source for theories and experimental results.

The thesis shall be submitted in two copies:
- The copies must be signed by the candidate.
- This text, defining the scope, must be included.
- The report must appear in a bound volume or a binder.
- Drawings and/or computer prints that cannot be included in the main volume should be organised in a separate folder.
- The bound volume shall be accompanied by a CD or DVD containing the written thesis in World or PDF format. In case computer programs have been made as part of the thesis work, the source codes shall be included. In case of experimental work, the experimental results shall be included in a suitable electronic format.

Supervisor :Marilena Greco
Submitted :16 January 2013
Deadline :10 June 2013

Marilena Greco
Supervisor

Preface

This master thesis was prepared at the Department of Marine Technology at the Norwegian University of Science and Technology. The thesis is supposed to reflect the work load of one semester, and is a continuation of a project thesis written last semester.

I would like to express my sincere gratitude towards my supervisor Prof. Marilena Greco, who has been available for my many questions throughout the semester. She has constantly given me another point of view on the results obtained, and thereby encouraged me to constantly investigate deeper into their origin. Without her help this thesis would have been considerably much smaller, and not nearly as interesting to write.

Special thanks to Enzo Marino and Claudio Lugni, for giving me the possibility to use their fully nonlinear wave model in my simulations. They have both been available for my many questions regarding both the use of the model, and the results obtained.

Finally I am very grateful to my girlfriend who took her time to proofread this thesis.

Even Rosenlund

Even Rosenlund

Trondheim June 3, 2013

Abstract

This master thesis investigates possible effects from nonlinear wave loading on bottom fixed offshore wind turbines. The resonant phenomena springing and ringing are reviewed with focus on their cause, and their possible occurrence in a bottom fixed wind turbine.

To investigate the effect of a nonlinear wave load model on a wind turbine, the calculation scheme in the wind turbine design-tool FAST has been extended with a new wave load model. The proposed load model was chosen because it could be coupled with fully nonlinear incident waves, and it is also expected that it can predict some aspects of the loads leading to ringing in a structure. The load model was developed by Rainey, and is based on conservation of energy arguments.

The new load model is compared with experiments on a cylinder in regular waves, and with the existing load model in FAST (Morison's equation). The numerical wave generation has been performed with a nonlinear Fourier approximation method, developed by Fenton. Results show similar prediction of the first harmonic load, which is slightly underpredicted by both. Good comparison is present for the second harmonic for low kr-values for both models. However, for larger kr-values significant overprediction is present, with Rainey predicting the largest values. Reasonably good agreement is found or the high kA-values for the third harmonic, when calculated by Rainey, while some underprediction is present when calculated by Morsion. The results also indicates that for slender structures, the nonlinearities in the incident waves, give a larger contribution to the loads than nonlinearities originating in the load formulation.

Simulations performed on a full scale turbine, have shown small differences between the two load models for turbine with a running rotor. Differences between results with a linear irregular sea and a fully nonlinear irregular sea are somewhat larger, but still the effect on improving the wave model is limited. This is due to the fact that the motion of the turbine is governed by the aerodynamic forces.

When the rotor has been set in a parked condition, sever springing occurs for all sea states investigated. The springing in a parked condition sometimes has a burst-like increase in amplitude, and time evolution of the tower top deflection is close to the one observed for ringing. However, no clear cases of ringing have been observed in these simulations. Both load models predicts the resonant oscillations, when used with either linear or fully nonlinear waves. The amplitude of the resonant oscillations are however dependent on the incident wave model. In general the fully nonlinear incident wave model leads to larger amplitudes in the resonant oscillations. For the case of fully nonlinear waves, there is a difference between the two load models, which is not present when linear waves are used.

Wave induced resonant oscillations have not been encountered when the turbine is running, which indicates that the reason for the resonant oscillations in a parked condition is the lack of aero-elastic damping. Some signs of a transient resonant phenomena is seen in strong winds, with additional indication that it is not triggered by waves, but the amplitude of the oscillations might be affected by the wave loading.

Sammendrag

Denne masteroppgaven undersøker mulige effekter fra ikkelinære bølgekrefter på en bunnfast offshore vindturbin. De resonante fenomenene “springing” og “ringing” blir undersøkt med tanke på kjennetegn og årsaker som kan skape dem. Videre blir muligheten for at de inntreffer i en bunnfast offshore vindturbin undersøkt.

For å undesøke effekten av ikkelinære bølgelaster på en vindturbin, har bølgelastmodellen i beregningsprogrammet FAST blitt utvidet med en ny lastmodell. Den nye lastmodellen er basert på bevarelse av energi i fluiden, og har blitt valgt på bakgrunn av dens mulighet til å bli brukt med fullstendig ikkelinære innkommende bølger, og dens mulige evne til å produsere laster som fører til ringing i strukturen.

Den nye lastmodellen har blitt sammenlignet med eksperimentelle data for en sylinder i regulære bølger, og også med den eksisterende lastmodellen i FAST, som er Morisons ligning. De innkommende bølgene har i simuleringene vært en bølgemodell basert på Fourier-rekker, utviklet av Fenton. Resultater viser at de to estimerer like laster for den første harmoniske lastkomponenten, og at begge underestimerer denne lastkomponenten sammenlignet med eksperimentelle resultater. For den andre harmoniske lastkomponenten er det forholdsvis bra samsvar mellom eksperiement og estimat fra begge lastmodellene, for sylindere med liten diameter relativt til bølgelengden. En betydelig overpredikasjon er tilstede etterhvert som bølgelengden minker, og Rainey overpredikerer mest. Rimelig bra samsvar er tilstede for den tredje harmoniske lastkomponenten for simuleringer med Rainey, mens Morison underestimerere noe for denne lastkomponenten. Resultatene synes å indikere at for slanke strukturer, er ikkelinearitetene i de innkommende bølgene viktigere enn ikkelinære komponenter som oppstår som følge av lastmodellen som brukes.

Simuleringer utført på en fullskala vindturbin med fungerende rotor, har vist små

forskjeller i resultatene fra de to ulike lastmodellene når man studerer bevegelsene til toppen av vindturbintårnet. Forskjellene mellom å bruke linære irregulære bølger og fullstendig ikkelinære irregulære bølger er derimot større, selv om også disse er små. Årsaken til de små forskjellene skyldes at når rotoren fungerer(dvs. ikke er parkert) er det de aerodynamiske kreftene som dominerer tårntoppens bevegelser.

Dersom rotoren parkeres, oppstår springing i alle undersøkte sjøtilstander. Amplituden i de resonante oscillasjonene gjennomgår enkelte ganger en voldsom økning, hvor amplituden nærmest dobles fra en oscillasjon til den neste. Dette er den observerte oppførselen som er nærmest tidsforløpet til ringing. Ingen tilfeller er observert der tidsforløpet er likt det klassiske ringingforløpet. Amplituden på de resonante oscillasjonene har vist seg å være avhengig av både bølgemodell og lastmodell.

Bølgeinduserte resonante oscillasjoner har ikke blitt observert når rotoren er virksom, noe som indikerer at oscillasjonene observert i parkert tilstand skyldes mangel på aero-elastisk demping. Små tegn til kortvarige resonante oscillasjoner er observert i sterk vind, med videre indikasjoner på at de ikke skyldes bølger, men at bølgelasten kan påvirke amplituden i oscillasjonene.

Contents

List of Figures

List of Tables

Nomenclature

ϕ	Velocity Potential
α	Angle between incident wave and cylinder axis
$\bar{r}$	Lagrangian position vector for free surface
$\bar{u}$	mean velocity in x direction
β	Incident wave propagation direction, relative to global coordinate system
$\cdot$	Dot product
ϵ	Perturbation parameter
Γ	Domain boundary
γ	Peakedness parameter JONSWAP
λ	Wave length
$\mathcal{F}(f_n)$	Value of Fourier transform at frequency f_n
Ω	Domain
ω	Frequency of incident wave [rad/s]
ω_p	Angular frequency corresponding to peak in wave spectrum
ρ	Density water = 1025 $[kg/m^3]$
σ	Constant used in JONSWAP
$\times$	Cross product
ζ	Instantaneous free surface elevation[m]
ζ_A	Amplitude of incident wave[m]

ζ_{max}	Maximum free surface elevation
B_j	Fourier coefficient of domain solution in Fenton for component j
C_A	Added mass coefficient
C_D	Drag coefficient
C_M	Mass coefficient equal to $1 + C_A$
E_j	Fourier coefficient of free surface elevation in Fenton for component j
F_N	Froude number
F_n	n't harmonic force
H_s	Significant wave height
M'_{max}	Nondimensional maximum bending moment
m_x	Added mass in x-direction
m_y	Added mass in x-direction
p_0	Atmospheric pressure
T_M	Modal wave period
T_P	Peak period of wave spectrum
T_z	Zero crossing period
u_1	Velocity in x direction of incident wave[m/s]
u_2	Velocity in y direction of incident wave[m/s]
u_3	Velocity in z direction of incident wave[m/s]
U_x	Velocity in x direction of structure[m/s]
U_y	Velocity in y direction of structure [m/s]
U_z	Velocity in z direction of structure [m/s]
x_1	x-coordinate
x_2	y-coordinate
x_3	z-coordinate
$\mathbf{W}$	Relative velocity vector between water and structure
$\mathbf{a}$	Acceleration vector of particle accelerations
$\mathbf{F}$	Force vector

$\mathbf{l}$	Vector tangential to cylinder axis
$\mathbf{M}$	Added mass matrix
$\mathbf{n}$	Normal vector of body, pointing outwards into the fluid
$\mathbf{t}$	Vector perpendicular to cylinder axis, pointing out of fluid
$\mathbf{U}$	Velocity vector of moving body
$\mathbf{V}$’	Velocity gradient matrix
$\mathbf{V}$	Velocity vector of particles in wave
$\mathbf{X}$	Positional Vector
A	Wave amplitude
c	Wave celerity
D	Diameter structure
DOF	Degree of freedom
EMD	Empirical mode decomposition
f	frequency [Hz]
FNV	Faltinsen - Newman - Vinje
g	Gravitational constant
H	Wave Height
h	Water depth
HOBEM	Higher order boundary element method
Ht	Height over the mean free surface [m]
i	Imaginary unit
IMF	Intrinsic Mode function
k	Wave number
KC	Keuligan-Carpenter number
L	Length
MEL	Mixed-Eulerian-Lagrangian
MM	Malenica & Molan
N	General number of components

n	General symbol for integer
OC3	Offshore Code Comparison Collaboration
p	Pressure
r	radius structure
SS	Sea state
T	Wave period
t	time
TLP	Tension Leg Platform
u	Velocity in x direction of incident wave[m/s]
u’	Velocity in x’ direction of incident wave[m/s]
v	Velocity in y direction of incident wave[m/s]
w	Velocity in z direction of incident wave[m/s]
w’	Velocity in z’ direction of incident wave[m/s]
x	x-coordinate
y	y-coordinate
z	z-coordinate

1 | Introduction

The need for greener energy sources is pushing investments towards renewable energy sources, e.g. wind power, solar power, wave power etc. According to Sclavounos et al. (2007) wind is the fastest growing renewable energy source, increasing with an annual rate of 25%. In 2007 a worldwide installed capacity of wind energy was approximately 74 [GW]. The vast majority of this came from onshore wind farms.

The growth of wind power is limited by the availability of areas where it is possible to place a wind farm, as well as the visual impairment they make on the landscape. Wind farms need large areas, with good wind conditions, but still close to where the energy is needed e.g. big cities.

The possibility of placing wind turbines offshore removes most of the problems with onshore turbines. A 5 [MW] wind turbine placed 30 [Km] from shore will be beyond the horizon, and will also be subject to stronger and steadier winds (Sclavounos et al., 2007).

However, the effect of higher order wave loads on offshore wind turbines has been of some concern. More specifically the phenomena springing and ringing might be important for both the maximum wave loads and for fatigue of the structure. Springing is usually considered to be steady state resonant oscillations in a structure, and ringing is transient resonant oscillations. These phenomena are normally governed by nonlinear effects, since most structures are designed so the natural frequencies lies well outside the range of linear wave forcing. Usually a ringing response is triggered by very steep waves that are on the verge of overturning or have already broken.

It is of interest to investigate the existing models developed in order to predict ringing, and try and couple one of them with the framework of a wind turbine design tool. If this can be performed, it will lead to better predictability of resonant phenomena in offshore wind turbines.

Further, it is interesting to investigate the effect of nonlinear loads on a turbine and the differences between nonlinear calculations and the existing scheme of linear theory.

The problem can be split into two parts; Formulating a load model that will be able to predict the loads that produce ringing, and predicting the wave kinematics so waves can be correctly modelled, also for the steepest waves.

The current practice in wind turbine simulation tools is to use linear irregular sea with a stretching technique to obtain wave kinematics, or alternatively weakly nonlinear regular waves to model incident waves. Highly nonlinear effects in the incident waves might be important for the ringing phenomenon and for the wave loads in general.

This thesis takes aim at implementing an improved load formulation into an already existing wind turbine simulation tool. The load formulation will be compared with the existing load formulation, and also with reports from experiments with a cylinder in waves. The effect of the higher order wave forcing will also be investigated, and if ringing is predicted, the phenomena will be further investigated.

In this thesis the effect from breaking waves that induce a slamming load on the structure will not be considered.

This Master thesis is a continuation of a project thesis I wrote last semester. In the project thesis several aspects of hydrodynamic loads on a offshore turbine was investigated. For completion it is necessary to repeat some of the topics previously covered.

1.1 Outline of Thesis

It has been an attempt at to structure this thesis so that it follows a natural progression of the topic, with increasing complexity.

Firstly the wind turbine structure is defined in terms of dimensions and weights. The environmental loads that it can be subjected to are defined. The structure is also defined in terms of which wave loads that dominates the force.

Secondly a short summary of how simulations on wind turbines are performed are given. This is a summary of the same topic covered in my project thesis.

Thirdly a review of nonlinear effects are given, in terms of the origin of nonlinear wave loads, and the possible responses in the structure of ringing and springing.

Fourthly improved load models are investigated, and a choice of one model to be implemented in the open source wind turbine design-tool FAST is performed, based on what is needed in order to predict ringing. Two improved wave models are presented, which both have been implemented in FAST.

Fifthly the changes made to FAST are verified, before the load model is compared with the present load model, and experiments on a cylinder in regular waves. The comparison is performed over a range of kA and kr-values. The goal of such simulations is to have a impression of the possible error present in the simulations.

Lastly a set of fully coupled simulations are performed. The main goal of these simulations is to investigate the differences between the two load models in a realistic load condition. Both linear irregular waves, and a fully nonlinear irregular sea are used to generate the incident waves. A secondary goal is to investigate any eventual resonant phenomena more in depth.

Throughout these steps I try to answer the following questions:

- Are there any significant differences between a linear incident wave model, and a fully nonlinear wave model
- Are there any significant differences between the load formulation used to calculate the wave force
- How good is the prediction of loads from the different wave models, when compared to idealised experiments with a cylinder in waves
- How important are the nonlinear effects for the operation of a offshore wind turbine
- Can the investigated structure experience the resonant phenomena ringing and springing

2 | Problem Description

This chapter is devoted to defining the wind turbine and the environment it might be subjected to.

2.1 Geometry

In this thesis, the structure of interest is a 5 [MW] reference turbine defined by National Renewable Energy Laboratory(NREL). It is a much used turbine in research due to it's specifications being openly available.

The reference wind turbine consists of a monopile which is driven into the seabed, the tower which sits on top of the monopile, the rotor which consists of the blades which is fastened to a hub, and a nacelle which is the connection between the tower and rotor. It is in the nacelle the generator is placed, which means that the structure will have a significant amount of weight on the tower top. In this thesis the boundary condition at the seabed will be assumed clamped. The dimensions of the structure can be summarised by figure 2.1.

All the properties of the structure will not be discussed in detail in this thesis, since they are not relevant for the wave loading and the structural response. The most important features are summarised in table 2.1.

More detailed data can be found in Jonkman et al. (2009) or in Jonkman and Musial (2010).

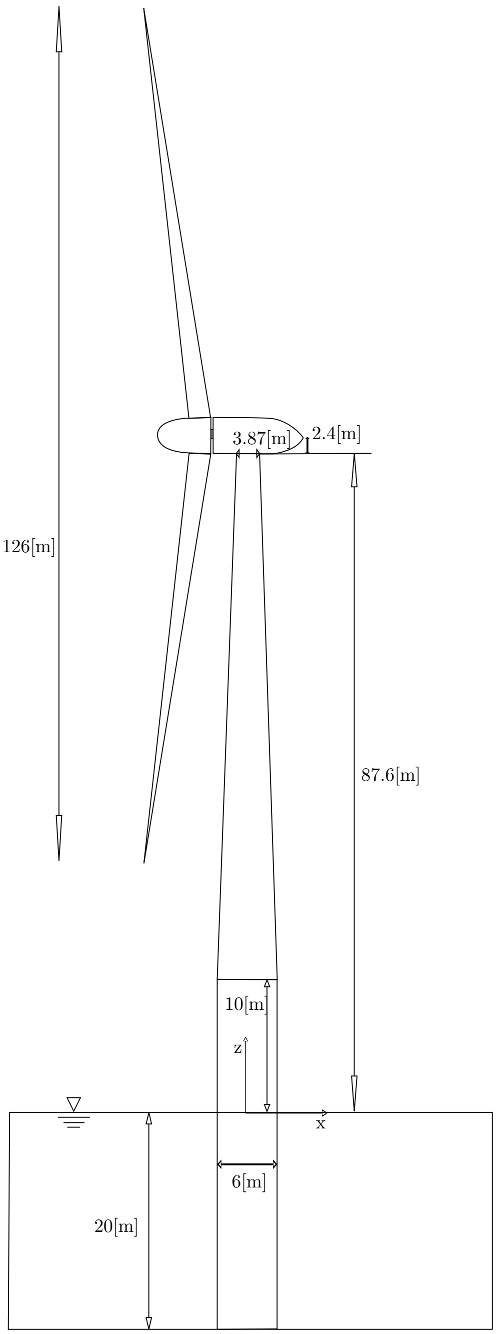

Figure 2.1: Dimensions of the wind turbine structure.

Rating	$5[MW]$
Rotor orientation, configuration	Upwind, 3 blades
Control	Variable speed, collective pitch
Drivetrain	High speed, multiple-stage gearbox
Rotor, hub diameter	$126[m], 3[m]$
Hub height	$90[m]$
Cut-in, rated, cut-out wind speed	$3[m/s], 11.4[m/s], 25[m/s]$
Cut-in, rated rotor speed	$6.9[rpm], 12.1[rpm]$
Rated tip speed	$80[m/s]$
Overhang, shaft tilt, precone	$5[m], 5[°], 2.5[°]$
Rotor mass	$110,000[kg]$
Nacelle mass	$240,000[kg]$
Tower mass	$347,500[kg]$
Coordinate location of overall center of mass (CM)	$(-0.2, 0.0, 64.0)[m]$

Table 2.1: Summary of wind turbine characteristics taken from (Jonkman and Musial, 2010)

2.2 Axis Definition

The origin of the coordinate system is chosen to be at the still water level, at the centre of the structure. The positive z-direction is upwards, and the positive x-direction is downwind as shown in figure 2.1.

2.3 Environment

The focus of this thesis is not to investigate site specific loads on a turbine, but to investigate of higher-order effects, so no exact location is used. However, it is necessary to have input regarding the environment it might be subjected to.

To have some wave statistics, a location somewhere between Norway, Great Britain and Denmark in what is known as the North Sea has been chosen. In parts of this area the water is shallow, so a bottom fixed solution is possible. In addition there is also a fairly short distance to major cities and power consumers, so it is not an unrealistic placement of such a turbine.

When one describes the sea environment it is common to divide it into short-term and long term sea states. Short-term is one sea state where one assumes stationary significant wave height (H_s) and Peak period (T_P). According to Veritas (2010) the duration of a sea state can be from 20 [min] to 3-6 [hours]. In order to say something about the wave conditions that the structure will be subjected to over time, long term statistics for the area is needed. Values from the long terms statistics may be used as input to a short term wave statistics model to simulate one sea state.

For short term statistics, irregular seas may be represented with a suitable wave spectrum. The North sea is usually described with the JONSWAP spectrum, defined mathematically as:

$$S(\omega) = \frac{\alpha g}{\omega^5} e^{-\frac{5}{4}(\frac{\omega_p}{\omega})^4} \gamma^{e^{-\frac{(\frac{\omega}{\omega_p}-1)^2}{2\sigma^2}}} \tag{2.1}$$

where γ is a peakedness parameter between 1 and 7, $\sigma = \begin{cases} 0.09, & \text{for } \omega \leq \omega_p \\ 0.07, & \text{for } \omega > \omega_p \end{cases}$ and α is a constant related to the wind speed and fetch length, typically in the region of $\alpha = 0.0081 - 0.016$ (Myrhaug, 2007).

This spectrum has been developed based on data from a relatively shallow area close to the shore, and it has been developed to describe sea states that are not fully developed (Myrhaug, 2007).

According to Veritas (2010) the mean value for γ is 3.3, but if this is not known for a specific location, some relations exist that might be used:

$$\gamma = \begin{cases} 5 & \text{for} \quad \frac{T_p}{\sqrt{H_S}} \leq 3.6 \\ e^{5.75-1.15\frac{T_P}{\sqrt{H_S}}} & \text{for} \quad 3.6 < \frac{T_P}{\sqrt{H_S}} < 5 \\ 1 & \text{for} \quad 5 \leq \frac{T_P}{\sqrt{H_S}} \end{cases} \tag{2.2}$$

This relations will be used in FAST to generate linear irregular sea.

Long terms statistics of H_s(Significant wave height) and T_z(Mean zero-crossing period) in the area where the turbine is located, has been gathered from Hogben et al. (1986), and is presented on an annual basis, with incident waves from all directions, in table 2.2. The data has been gathered somewhere in the North-sea, and is expected to be a reasonably realistic choice for the wave environment the turbine might be subjected to.

This table is based on the zero crossing period, and not the peak period which is used in the JONSWAP spectrum. The two can be related by the following relation, taken from Veritas (2010)

$$\frac{T_z}{T_P} = 0.6673 + 0.05037\gamma - 0.006230\gamma^2 + 0.0003610\gamma^3 \tag{2.3}$$

$H_s[m]\|T_z[s]$	< 4	$4-5$	$5-6$	$6-7$	$7-8$	$8-9$	$9-10$	$10-11$	$11-12$	$12-13$	> 13	Total
0-1	19	86	94	41	10	2	-	-	-	-	-	252
1-2	3	49	121	99	40	10	2	-	-	-	-	324
2-3	1	17	63	73	40	13	3	1	-	-	-	211
3-4	-	6	27	39	26	10	3	1	-	-	-	112
4-5	-	2	11	19	14	6	2	1	-	-	-	55
5-6	-	1	4	9	7	4	1	-	-	-	-	26
6-7	-	-	2	4	4	2	1	-	-	-	-	13
7-8	-	-	1	2	2	1	1	-	-	-	-	7
8-9	-	-	-	1	1	1	-	-	-	-	-	3
9-10	-	-	-	1	1	-	-	-	-	-	-	2
10-11	-	-	-	-	-	-	-	-	-	-	-	0
11-12	-	-	-	-	-	-	-	-	-	-	-	0
12-13	-	-	-	-	-	-	-	-	-	-	-	0
13-14	-	-	-	-	-	-	-	-	-	-	-	0
>14	-	-	-	-	-	-	-	-	-	-	-	0
Total	23	161	323	288	145	49	13	3	0	0	0	1005

Table 2.2: Wave Statistics for the North Sea, taken from (Hogben et al., 1986), area 11.

By using this relationship with the mean value of $\gamma = 3.3$, then the ratio between T_P and T_z is given as:

$$\frac{T_p}{T_z} = 1.2843 \tag{2.4}$$

Which gives the following table for T_P

$T_z[s]$	4	5	6	7	8	9	10	11
$T_p[s]$	5.137	6.421	7.706	8.990	10.274	11.558	12.843	14.127

Table 2.3: Peak periods of the observed sea states

The waves and the local wind is considered to be uncorrelated, but some kind of relationship must be used. It is for instance unrealistic with large waves, and low wind speed. Here it is possible to utilise the values for sea states and the corresponding wind in the North Atlantic ocean given in Faltinsen (1990), and reproduced in table 2.4. This is not in the same area as the wave statistics have been gathered from, so care should be used when utilising it.

T_M is the modal wave period, which is equal to the period of the peak in the wave spectrum, i.e. $T_M = T_P$. The mean sustained wind velocity is given at 19.5 [m] above the sea surface, to convert to another amplitude Ht_2, the following relation can be used(Faltinsen, 1990):

$$V_2 = V_1 (\frac{Ht_2}{19.5})^{\frac{1}{7}} \tag{2.5}$$

Sea State	Range H_s [m]	Mean H_s [m]	Range T_M [s]	Most prob. T_M [s]	Mean Sust. wind vel.[kn]
0-1	0-0.1	0.05	-	-	3
2	0.-0.5	0.3	3.3-12.8	7.5	8.5
3	0.5-1.25	0.88	5.0-14.8	7.5	13.5
4	1.25-2.5	1.88	6.1-15.2	8.8	19
5	2.5-4	3.25	8.3-15.5	9.7	24.5
6	4-6	5	9.8-16.2	12.4	37.5
7	6-9	7.5	11.8-18.5	15	51.5
8	9-14	11.5	14.2-18.6	16.4	59.5

Table 2.4: Annual sea state occurences in the North Atlantic, reproduced from Faltinsen (1990)

The main purpose of table 2.4 is to obtain some relationship between the wind speed and the sea state. This will be used in chapter 10 to run realistic load cases on the turbine. By comparison it appears to be some difference in the range of T_P for the wave heights, with the data in table 2.2 shows somewhat lower periods (Note that the period in table 2.2 is with the mean zero crossing period, so comparison needs to be done with the periods calculated in table 2.3).

This means that the two tables are not totally compatible with each other, so care should be taken when utilising table 2.4 to obtain wind speeds for the data in table 2.2. Nevertheless, since the the reported range of T_P in table 2.4 contains elements of the data in table 2.2, the reported relations between sea state and wind speed will be used. It is believed that the wind speeds at the chosen location will be lower than the reported values, since the wind speed is gathered from the North Atlantic Ocean and the turbine is placed in the north sea, reasonably close to shore. This means that using the relationship between waves and wind in table 2.4 will be conservative.

2.4 Natural Frequencies of Structure

The natural frequencies of the structure, can give valuable information of the sensitivity of the structure to wave loading. If for instance the natural frequency of the tower is close to the wave frequencies, it might experience large deflections.

The open source wind turbine design tool FAST will be used to calculate the natural frequencies of the structure. For the theory on the workings of how FAST does this, the reader is referred to the user guide Jonkman and Buhl (2005).

The rotor speed will affect the natural frequencies of especially the blades, but other coupling effects might also occur. Therefore, in order to investigate the

Degree of freedom	**Natural Frequency [Hz]**
1st tower side-to-side bending mode DOF	0.2764
1st tower fore-aft bending mode DOF	0.2800
1st Blade Collective flapwise	0.6955
1st Blade Asymmetric flapwise pitch	0.6690
1st Blade Asymmetric flapwise yaw	0.6660
1st Blade Collective edgewise	3.6227
1st Blade Asymmetric edgewise pitch	1.0891
1st Blade Asymmetric edgewise yaw	1.0787
2nd Blade Collective flapwise	2.019
2nd Blade Asymmetric flapwise pitch	1.8845
2nd Blade Asymmetric flapwise yaw	1.9326
2nd tower side-to-side bending mode DOF	2.3562
2nd tower fore-aft bending mode DOF	2.3965
Nacelle yaw DOF	6.1344
Drivetrain	0.6174

Table 2.5: Results of eigenvalue analysis(frequencies are undamped)

basis of the structure, the rotor speed is set to zero. The natural frequencies of the degrees of freedom are reported in table 2.5

The bending modes for the blades are defined with respect to the local structural twist. That means that the mode shapes twist with the blade, are given in three dimensions and will generally not lie withing a single plane. Therefore a pure flapwise deflection of the blade will lead the tip to deflect both in the edgewise direction and in the flapwise direction. Thus, there will be natural frequencies relating these motions for a pure flapwise/edgewise bending.

By blade assymetric flapwise/edgewise pitch/yaw it is meant that these blade asymmetric modes will couple with the nacelle yaw and pitch motion, i.e the tower top deflection.

Since tower and support structure are isotropic, the source of the difference between the side-to-side and front-to-aft could be either coupling between the blades and the tower, or the fact that the mass of the rotor is not at the centre-line.

The results calculated here might be validated against the results obtained as part of a major validation project in Jonkman and Musial (2010), because the structure is the same as in their study and also one of the solvers studied there has been used. By comparison with Jonkman and Musial (2010, figure 6) the results seems quite similar, which is a clear indication that the solver has been used correctly.

By comparing with the long term statistics in table 2.2 it is observed that all frequencies are well outside the frequency range of most incident waves. This means that the natural frequencies should not be significantly excited by linear wave forces. The natural frequencies of the tower should however be within the range of second or higher order sum forces. This is an indication that it is important to investigate how the turbine behaves when nonlinear wave loads are taken into account.

2.5 Theoretical Basis

The governing equation for the motion of water is Navier-Stokes' equation. This equation has no general analytical solution, and to solve it directly using numerics is very time consuming, and also needs large computer resources.

Hence it is common to assume an incompressible, irrotational and invicid fluid, which is called an ideal fluid. This reduces the governing equation of the fluid domain to the continuity equation, and conservation of momentum. For completeness some aspects of the basic theory is covered here, but for a thorough treatment the reader is referred to e.g White (2008) or Newman (1977)

The velocity $\boldsymbol{V} = (u, v, w) = (u_1, u_2, u_3)$ must satisfy the two mentioned equations, written as (Einstein notation is used throughout this section where it is convenient, meaning that a repeated index implies summation over all indexes):

$$\frac{\partial u_i}{\partial x_i} = 0 \tag{2.6}$$

$$\rho \frac{\partial u_i}{\partial t} + u_j \frac{\partial u_i}{\partial x_j} = -\frac{1}{\rho}\frac{\partial p}{\partial x_i} + \frac{1}{\rho} F_i \qquad for\ i = 1, 2, 3 \tag{2.7}$$

It is possible to define a mathematical function which we call velocity potential

$$\phi = \phi(\boldsymbol{X}, t) \text{ where } \boldsymbol{X} = (x, y, z) = (x_1, x_2, x_3) \tag{2.8}$$

The velocity potential is defined as follows:

$$\frac{\partial \phi}{\partial x_i} = u_i \tag{2.9}$$

By using the definitions above in the continuity equation, eq. (2.6):

$$\frac{\partial u_i}{\partial x_i} = \frac{\partial}{\partial x_i}\frac{\partial \phi}{\partial x_i} = \frac{\partial^2 \phi}{\partial^2 x_i} = 0 \tag{2.10}$$

This is the Laplace equation which describes the conservation of mass for the fluid domain. In vector notation it reads :

$$\boldsymbol{\nabla}^{\mathbf{2}}\phi = 0 \tag{2.11}$$

Laplace's equation governs the solution in the fluid domain, and the theory of ideal fluid flow is usually called potential theory, named after the velocity potential ϕ. By using the velocity potential to express the velocities in Euler's equation (eq. 2.7), and integrate over the spatial coordinates, it is possible to show (see Newman (1977)) that it reduces to:

$$\frac{\partial \phi}{\partial t} + \frac{1}{2}(\frac{\partial \phi}{\partial x_j})^2 = -\frac{1}{\rho}(p + \rho g x_2) + C(t) \tag{2.12}$$

Equation 2.12 is more commonly known under the name Bernoulli's equation and is a relation between the pressure, and the velocity potential in the fluid. When the pressure in the fluid is known, forces can be found by integrating the pressure over the area, and since ϕ is a function of t the time variation of the forces can be found.

This method is by far the most utilised way to obtain the forces on a body, but there exists another way, which takes conservation of energy in the fluid as a base for force calculations.

In order to satisfy the physics of what is happening on the boundaries of the fluid domain, a set of conditions must be imposed on the boundaries. The physical conditions that needs to be satisfied are:

1. No flow through an object that is moving or is stationary in the fluid
2. No flow through the seabed
3. Fluid particles on the surface, stays on the surface
4. The pressure on the sea surface is constant and equal to the atmospheric pressure p_0

The mathematical description of the first item means that the velocity normal to the surface needs to be the same velocity as the surface itself has, i.e.

$$\frac{\partial \phi}{\partial n} = \boldsymbol{U} \cdot \boldsymbol{n} \quad \text{on } S_{Body} \tag{2.13}$$

$\boldsymbol{U} = (U_x, U_y, U_z) = (U_1, U_2, U_3)$ is the velocity of the structure in the principal directions (x, y, z) of a point on the structure. The normal vector $\boldsymbol{n} = (n_1, n_2, n_3)$, has different conventions, some use the convention of it pointing into the fluid, and others pointing into the body. Throughout this text the definition is that it is pointing into the fluid domain, unless otherwise stated.

The second boundary condition follows straight from the first, except that the seabed is not moving.

$$\frac{\partial \phi}{\partial n} = 0 \quad \text{on } S_{Seabed} \tag{2.14}$$

The third condition is usually called the kinematic free surface condition and can be described mathematically by the following (see e.g. Newman (1977) or Faltinsen (1990) for derivation).

Let $\zeta(x, y, t)$ be the free surface, then the following condition must be satisfied:

$$\frac{\mathrm{D}(z-\zeta)}{\mathrm{D}t} = \frac{\partial \zeta}{\partial t} + \frac{\partial \phi}{\partial x}\frac{\partial \zeta}{\partial x} + \frac{\partial \phi}{\partial y}\frac{\partial \zeta}{\partial y} - \frac{\partial \phi}{\partial z} = 0 \quad \text{On } z = \zeta \tag{2.15}$$

The last boundary condition can be obtained by utilising Bernoulli's equation for the pressure, and setting that equal to the atmospheric pressure on $z = \zeta$,

$$-\frac{1}{\rho}(P - P_a) = \frac{\partial \phi}{\partial t} + \frac{1}{2}(\nabla \phi)^2 + gz = 0 \quad \text{on } z = \zeta \tag{2.16}$$

This is the exact dynamic free surface condition, to be satisfied on the free surface.

In marine hydrodynamics, these boundary conditions are where the problems stems from, the equations are nonlinear, and must be applied on the unknown surface $z = \zeta$. The process of obtaining a velocity potential that satisfy all boundary conditions exactly is very difficult, but some techniques exists that makes the problem more manageable. This topic will be further discussed in section 4.1.

Laplace's equation is linear, which is important, because this makes it possible to create the total solution as a sum of solutions to different sub-problems. The solution is then usually made up of two contributions: The diffraction, where the incident waves and the diffraction flow satisfy the impermeability of the body, and the radiation where the structure is forced to oscillate, and it creates radiating waves.

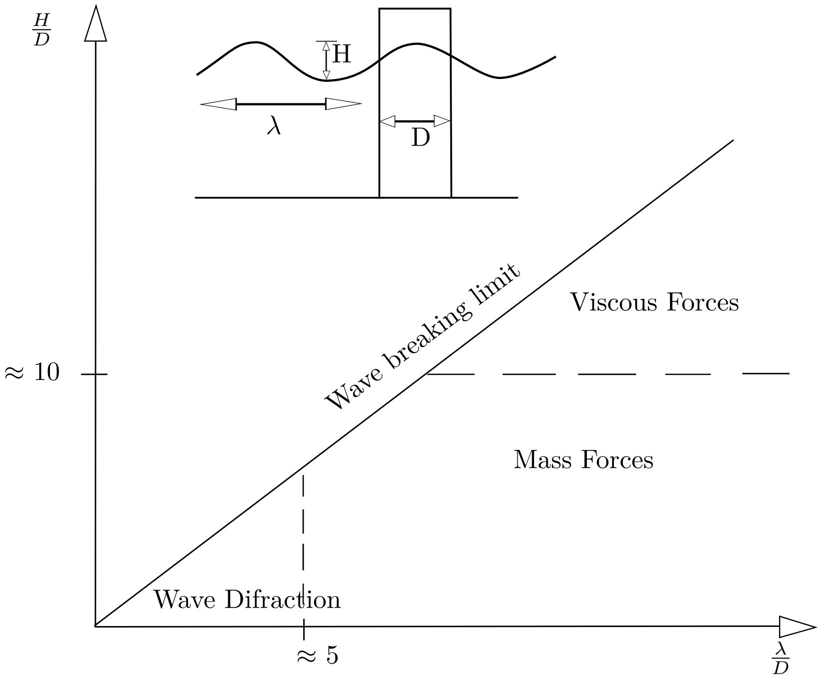

Figure 2.2: Relative importance of mass, viscous drag and diffraction forces, reproduced from (Faltinsen, 1990).

2.6 Load Regime

The last section stands as the theoretical introduction to the equations that governs the problem. In this section simple engineering approximations is used to gain some insight into the load regime such a wind turbine might be subjected to.

To obtain some initial information about which kinds of loads that are dominating, it is possible to look at the ratio between wave length(λ) and cylinder diameter(D), in addition to the ratio between wave height(H) and cylinder diameter. Figure 2.2 is reproduced from Faltinsen (1990) and shows where the various components of wave forces dominates. The ratio $\lambda/D \approx 5$ is the usual border between the long wave length regime and the diffraction regime.

To obtain the wavelength from this it is possible to utilise the linear dispersion relation (equation 2.19), along with the definition of the wave number k and wave

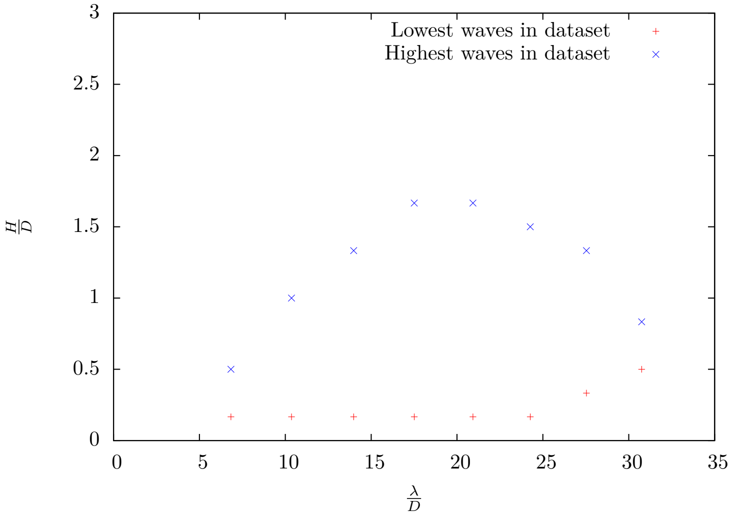

Figure 2.3: Classification of structure using realistic wave conditions.

frequency ω.

$$k = \frac{2\pi}{\lambda} \tag{2.17}$$

$$\omega = \frac{2\pi}{T} \tag{2.18}$$

$$\frac{\omega^2}{g} = k\tanh(kh) \tag{2.19}$$

The last equation is the linear dispersion relation for finite water, h being the water depth in meters. A bit of algebra produces the following implicit equation for the wave length at a water depth of 20 [m]:

$$\lambda = g\tanh(\frac{2\pi}{\lambda}20)\frac{T^2}{2\pi} \tag{2.20}$$

By solving this with an iteration process, it is possible to obtain the wavelength of a linear wave with wave period T.

With the values for T_P from table 2.3, and also the wave heights from table 2.2 the two ratios have been plotted in figure 2.3.

From the peak frequency plots it appears that all waves gives $\frac{\lambda}{D} > 5$. However in an irregular sea state, there also exists waves that have a smaller period than the peak frequency, so the structure will also be subjected to even shorter waves, which will have $\frac{\lambda}{D} < 5$. It is however noted from the wave statistics that there are relatively few sea states with such a low period. In addition the significant wave height is also quite small which indicates that forces should be small. It is thereby assumed that a long wave approximation is valid, and the structure will be dominated by mass forces.

A structure in the long wavelength regime is beneficial from a force calculation point of view. This is true, since the wavelengths are much longer than the diameter of the structure, the incident waves will be more or less unaffected by the structure.

This simplification means that it is not necessary to model the wave-structure interaction that distorts the free surface, since it can be assumed that this does not happen. The forces on the structure can then be found by integrating the pressure in the waves as the structure was not there. In addition there comes a force contribution from the diffraction potential which the structure sets up to ensure impermeability. If these assumptions are used to find the solution to a cylinder in linear regular waves, it will result in the inertia term in Morison's equation which is the current way of calculating wave forces in wind turbine tools for bottom fixed turbines.

3 | Simulation Tools

The art of performing accurate simulations on offshore wind turbines deserves a small introduction. In this chapter a resumé of special aspects of a wind turbine is given.

3.1 Coupled Nature of Wind Turbines

For secure operations of any structure, it is important that the environment can not significantly excite any part of the structure at it's natural frequency. If a structure is constantly excited at it's natural frequency it may collapse, like the widely known Tacoma Narrows Bridge accident.

The wind turbine is in that aspect no different, as system of different components, each with it's particular weight and stiffness causing a range of natural frequencies in the structure. The difference between a wind turbine and other offshore structures, is the highly coupled nature of the wind turbine. An example might be that large and fast oscillations of the tower will produce loads at the blade root, and alter the loads on a blade from the incident wind. This is also true the other way, where large oscillations of the blade may cause resonant oscillations in the tower.

For onshore wind turbines these possible effects are recognised, and design tools are labeled as “Aero-servo-elastic” codes, meaning that they use a fully coupled system to incorporate effects from the aerodynamics, the control system and the structural response to the applied loads. In an offshore environment there is an additional load contribution from the sea, hence a simulation of such a turbine would necessary need a fully coupled “Aero-hydro-servo-elastic” simulation.

Around the year 2004 the IEA-Wind (International Energy Agency - Wind) recognised that there was a growing interest in offshore wind turbines, along with big challenges needed to be solved in order to have a safe development of turbines located offshore. In order to gain knowledge and develop new technology, IEA-Wind approved the startup of annex 23 (Jonkman and Musial, 2010). One of the main purposes of this task, was to compare different solvers so the coupling effect between the various elements of the turbine could be understood. This was done in a subtask called OC3 - Offshore Code Comparison Collaboration. The effort has been continued into a new task, including code comparison for more advanced structures, called OC4.

OC3 is compromised by four phases, with a different structure to be compared in each. Starting with a rigid foundation monopile in phase I, continuing with a flexible foundation in phase II, a floating tripod turbine in phase III, and a floating spar-like wind turbine in phase IV.

For phase I, which is the structure of interest in this thesis, all solvers used Morison's equation with linear incident waves with the possibility for using various stretching methods. In later phases the ability to use stream theory has been included in some codes, so it can be assumed that this is also valid for bottom fixed turbines. For details regarding stream theory see e.g. Dean and Dalrymple (1984).

OC3 is by no means a complete overview of what theories the solvers use, but it is a good indication of what seems to be the established standards for calculations on offshore wind turbines.

When solving problems of motion, there are two different approaches possible; solving the motion in the frequency domain or in the time domain. The first possibility means that the solution to the problem is assumed to be steady state. This makes it possible to separate the time dependence of the problem, from the frequency of the applied loads. The oscillation frequency of the solution is then the same as the frequency of the applied load. This approach is much utilised for the motion of different offshore structures, meaning that several well developed tools for such calculations exists. The downside of the technique is that one assumes that the solution is steady state, so the information about transient events are not included.

The other approach is to solve the problem in the time domain. For this approach there is not placed any limitation on the solution, but it needs to be found by marching forward in time. If properly implemented, it will simulate transient events, nonlinearities in the response and loads etc.. The solution will naturally be more like a real world situation. The downside of this method is the increased time spend on performing a simulation.

According to Cordle and Jonkman (2011) frequency domain tools has been used as a proof of concept, to show that floating offshore wind turbines could be designed so that the natural frequencies are outside the range of wave forcing. However, as the following quote from the paper states, the technique is not acceptable in a realistic design tool:

“ ...Frequency-domain calculations, however, also have important limitations. They cannot capture nonlinear dynamic characteristics and cannot model transient loading events — both of which are important for wind turbines because the nonlinear dynamics introduced through transient events and control system actions are significant for loads analysis. ” (Cordle and Jonkman, 2011, page 1)

It is concluded that the solver to be used in wind turbine analysis needs to solve the problem in the time domain. Regarding nonlinear wave effects, the need for a fully coupled simulation in the time domain is advantageous, since it means that as long as the forces from the waves are properly modelled, the different nonlinear effects will be taken directly into account in the equation of motion. This means that the global effect on the turbine from the waves are accurately modelled, given that one manages to describe the forces accurately.

Common for all solvers in OC3 is that the possibility of nonlinear loads from the waves are not completely taken into account. Morison’s equation will predict higher order loads, if nonlinearities are present in the incident waves, or if integrated to a moving free surface. Since the solvers allow for stretching to the free surface, the current load formulation will provide some weakly nonlinear wave loads. However, since linear incident waves are usually derived assuming kA to be small, so that all terms dependent on $(kA)^2$ are dropped, they depend on a small wave steepness in order to be accurate. For steep waves this is not satisfied, so linear waves will fail to accurately predict wave loads for the steepest waves. Marino et al. (2013) has investigated the difference between the loads from a linear incident wave, and a fully nonlinear incident wave. They find large differences between the two in steep incident waves.

When it comes to the load formulation, there also exists alternatives to Morison’s equation which contains higher order correction terms to increase the accuracy of the load calculations. The effects of using more accurate wave and load models are uncertain. Through experience gained in my project thesis, it was found that the aerodynamics seems to be more important for the motion than the wave loads. An improved wave load model might then not have such a large effect for a running turbine. This is one of the aspects this thesis tries to address.

In appendix A a small introduction to Morison’s equation and wheeler stretching are given. It is noted that FAST uses a formulation of Morison’s equation that takes the relative velocity between the structure and the water particles into account. It also implements a term that gives added mass loads from the acceleration of the structure. The implementation can be written as:

$$\mathrm{d}F = \rho\pi\frac{D^2}{4}(1+C_A)dza_x - \rho C_A\pi\frac{D^2}{4}dz\dot{U}_x + \frac{\rho}{2}C_D Ddz|u-U_x|(u-U_x) \quad (3.1)$$

Where u is the horizontal velocity of the water particles, $\dot{U}_x$ is the local structure acceleration in and U_x is the local structure velocity. C_A is the added mass coefficient, C_D the drag coefficient.

It can be shown by writing the drag term as a Fourier series, that the drag term will include odd harmonics ($\omega, 3\omega, 5\omega,...$) and is thereby a source of nonlinear forcing.

The procedure of stretching the kinematics, so one can integrate the the instantaneous free surface is in reality a nonlinear extension of the linear theory. This is because an integration to a moving free surface will cause second order loads, a feature that is shown analytically for a linear incident wave, wheeler stretching and forces by the inertia term in Morison's equation, in appendix A. The result from this derivation is given in equation 3.2:

$$F = \rho\pi r^2(1+C_A)\omega^2\frac{\zeta_A}{k}\cos(\omega t) + \rho\pi r^2(1+C_A)\omega^2\frac{\zeta_A^2}{2kh}\sin(2\omega t) \quad (3.2)$$

By virtue of the current practise of stretching the kinematics, wind turbine solvers includes some nonlinear wave loads. However, it is important to see how these terms compare to the higher order forces if a more accurate load model is used. Because the interest is in how the nonlinear wave loads affects the global system, these comparisons must be performed within the fully coupled framework.

4 | Nonlinear Effects

Since this thesis focuses on nonlinear effects on offshore wind turbines, it is of interest to investigate where the nonlinear effects come from, and what the effect on the structure might be. In this chapter a review the phenomena springing and ringing is performed, along with an introduction into nonlinear effects.

4.1 Higher-Order Effects

As discussed in section 2.5 the governing equation for the fluid flow is Laplace's equation, which is a linear equation. That would usually mean that it is simple to solve. However, the boundary condition on the free surface is nonlinear. This means that it will cause nonlinear effects in the solution for a velocity potential that satisfies both Laplace's equation and the prescribed boundary conditions. Due to the fact that it is nonlinear and valid on a unknown position it is not easily solved, hence a simplification is usually introduced.

To overcome the nonlinearity introduced by the boundary condition, a common approach is to replace the problem with a set of equations that are linear. The approach will be described shortly here in order to obtain a basic understanding of nonlinearities.

The first step is to use a perturbation technique. Here we assume that the solution can be written as a power series of $\epsilon = k\zeta_A$, shown here for the velocity potential and the free surface elevation:

$$\phi = \phi_1\epsilon + \phi_2\epsilon^2 + \phi_3\epsilon^3 + ...$$

$$\zeta = \zeta_1\epsilon + \zeta_2\epsilon^2 + \phi_3\epsilon^3 + ...$$

Where $\epsilon = k\zeta_A$ is the wave steepness, which must be assumed to be small for this to be valid (e.g. the series converges). The classical assumption in a perturbation approach is that the wave amplitude is much smaller than all other length scales. ϵ will then be a measure of the nonlinearities in the problem (Greco, 2011). As the order of ϵ is increasing for each term, the order of the wave amplitude dependence will also increase for each term. When talking about higher order terms, it is usually referred to terms which are dependent on $(k\zeta_A)^n$, or just ζ_A^n, where $n > 1$. An mathematical effect of this procedure is that for each order, another harmonic will be introduced, so that by the order n the solution will contain a load contribution which oscillates with the n^{th} harmonic of the base frequency(e.g. the frequency of the incident waves).

Still we do not know the position of the free surface elevation where the boundary condition is to be satisfied. To overcome this problem a Taylor expansion can be used to transfer the free surface boundary condition from the free surface to the mean sea level, i.e $z = 0$.

$$\phi(x, y, \zeta, t) = \phi(x, t, 0, t) + \zeta(\frac{\partial \phi}{\partial z})_{z=0} + \frac{1}{2}\zeta^2(\frac{\partial^2 \phi}{\partial^2 z})_{z=0} + ... \tag{4.1}$$

When using the Taylor expansion we express the needed quantities at the free surface by their value at the $z = 0$. In this way the position where the boundary condition must be satisfied is constant, and thereby it is possible to find solutions.

Further by substituting the perturbation series into the resulting expression, we will end up with a set of linear equations for the boundary condition. The first equation is a homogenious equation, and when solved it gives the first order/linear solution to the problem. The second equation is inhomogenious and needs the solution to the first order potential in order to be solved, and so on for each successive term. This tells us that the linear solution does not depend on the solution of the higher order potentials, but all the higher order potentials depend on the solutions to all the lower order potentials.

The nonlinear boundary value problem has by the introduction of a perturbation series and a Taylor expansion ended up as a linear boundary value problem for each potential in the perturbation series. This makes it possible (at least in theory) to find a solution to the velocity potential accurate to any given order.

The disadvantage of this solution scheme is that the equations become more algebraically advanced, which leads to increasing difficulty in finding the analytical solution to the higher order terms.

Since the governing equation of the problem(Laplace equation) is linear, it means that the velocity potential for each order is a sum of the potential from incident waves, the potential the structure sets up in order to enforce impermeability and the potential generated by oscillations of the structure. This means that nonlinear loads can originate from the incident waves, the presence of the structure in waves or the motion of the structure.

The nonlinear analytical solution to incident waves, based on a systematic power series expansion in the wave amplitude, is called a Stokes expansion. These waves satisfies the boundary conditions better than a linear incident wave. Newman (1977) notes that already by including the second order corrections to the free surface elevation, the wave obtains an appearance closer to what can be observed in nature.

The biggest uncertainty with this procedure is the convergence of the perturbation approach. If this converges then each successive term will be smaller than the previous, and the sum will converge to a given value. When dropping terms of say order ϵ^n it is certain that all dropped terms are small and only a small error is introduced. If on the other hand the power series diverges, then the series will not tend towards a given value, and the whole procedure is invalid.

The question of diverging in the Stokes expansion is important, as it will be shown, ringing is believed to be caused by steep waves. These waves will contain significant nonlinearities, which may not be represented suitably by a series solution. According to Rainey (1995a, Appendix B) the stokes expansion seems to have diverged for incident waves once the wave height is of comparable size to the structural diameter. For the case of offshore wind turbines in steep waves it might then be questionable if higher order load formulations based on a conventional perturbation technique will give accurate forces.

Regarding the nonlinear forces on a structure, they are really a result of several factors. The force on a structure might be found by integrating the pressure over the surface, and the pressure can be found from Bernoulli's equation. This equation contains one linear term in the velocity potential, and one term with the square of the potential. The first source of nonlinear forces is then the square dependence on the first order potential, which causes second order effects. The next source is the pressure from higher order potentials, which causes both forces dependent on the same order as itself, and also forces of the squared order of itself.

When the body moves, it will modify the pressure over the surface of the structure. Since the motion of the structure is in turn dependent on the pressure, it is clear that when the structure is allowed to move, a higher order dependence is present.

The last source mentioned here is a varying wetted surface. This means that when integrating the pressure over the free surface, the surface is dependent on the incident wave elevation. This will lead to a higher order term, since the pressure is dependent on the incident waves and so is the integration limits. Other sources of nonlinear effects might exist, but it is believed that the mentioned ones are the most important for a general structure.

For a bottom fixed wind turbine, very small deflections are expected at the free surface intersection. This is mainly due to the relatively short distance to the seabed where the structure is fastened, and the stiffness of steel. Simulations performed in chapter 10 shows maximum deflection of the tower top of ≈ 0.6[m] in the most severe sea states. With such small deflections at 90[m] above the mean sea level, even smaller deflections are present at the mean sea level. This means that the motion of the structure can be neglected when the kinematics of the incident waves are calculated.

When it comes to nonlinear effects from the higher order potentials, it is believed that the most important nonlinearities are in the incident waves, because the structure can be considered slender and only small contributions should originate from it's presence.

The effect of a changing wetted surface is currently enabled through the ability to stretch the wave kinematics to the instantaneous free surface elevation.

When it comes to the potential effect of the nonlinear loads on the structure, it is mainly two phenomena of interest for a wind turbine; Springing and ringing. Common for both is the possible lack of ability to accurately predict them in the existing design tool. The two following sections will review the two phenomena, and investigate if the structure can be prone to these effects.

4.2 Springing

Springing is commonly defined as steady state resonant oscillations. The interest here is to investigate if the waves can cause steady state resonant motion in the structure.

As earlier stated, offshore structures are usually designed so that the natural frequency lies well outside the range of linear wave forcing. This means that resonant oscillations usually are the result of higher order forces. Springing is often contributed to second order loads, since these can be large enough to be significant all the time.

In this thesis the term steady state will be used slightly loosely; with steady state resonant oscillations it is meant oscillations where the frequency is at the natural frequency, but the amplitude can vary. The oscillations will naturally need to have a start and a finish, so they are not steady state in the term of infinite duration. However, for the oscillations to be steady state it is assumed that they are present for a long time, and that they do not show a clear decay pattern from the start as a transient event would. The reason for such a definition is that it is of interest to study how the turbine behaves in irregular sea. Naturally the load on the structure will not be steady state, and so the response of the structure can never obtain a truly steady state oscillation where the amplitude is constant, and the oscillations goes on indefinitely.

The reference turbine studied in this thesis, has as shown a natural frequency outside the range of linear wave forces. This is quite normal, but it also indicates that it can only be excited by higher order sum-frequency forces. This makes it important to accurately model such forces, in order to determine if the structure can be prone to springing. With the natural frequency of the first bending mode of approximately 0.28 [Hz] it is believed that the structure might in fact experience springing.

4.3 Ringing

Sometime around the end of the 1980's, transient oscillations at the natural frequency in some of the tension leg platforms (TLP), and monotower platforms in the North Sea were observed. The phenomenon was named ringing. It appeared that ringing occurred when the structure was interacting with very steep waves, and the wave amplitude was of the same order as the radius of the structure (Grue, 2002) (Faltinsen et al., 1995). The natural frequency of the structures was approximately three times the frequency of the waves, leading to the belief that it was caused by third order effects. The classical shape of a ringing event is presented in figure 4.1

Since it was believed that the cause was due to third order wave effect, effort was put into obtaining a theory capable of handle such non-linearities. One such example made by Faltinsen, Newman and Vinje (Faltinsen et al., 1995). They performed a perturbation technique to the third order for wave loads in the long wavelength regime. Their technique is not following the standard way of assuming wave height being small compared to all other length scales. Instead they assumed that the wave height was of the same order as the cylinder radius. Malenica and Molin (1995) presented a conventional perturbation technique to the third order with the regular assumptions of wave height small with respect to all other length scales. Rainey (1989) presented a force formulation based on

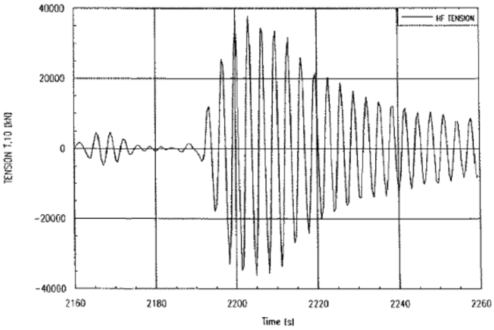

Figure 4.1: Classical shape of a ringing event, copied from Grue and Huseby (2002).

slender body theory, but instead of pressure integration it is utilising conservation of energy arguments.

Welch et al. (1999) investigated the response of a vertical cylinder in breaking waves, and suggest that the phenomenon might be excited by impact from a plunging jet or a splashing jet(see original paper for definitions on the types). In Grue and Huseby (2002) it is documented that ringing in the form of a tuned resonant build up occurred even for the moderately steep waves in an irregular sea environment. They report that the wave induced resonant oscillations are characterised by a resonant build-up during a time interval of the order of one wave period. This is not compatible with an impact from the waves, which should give the largest oscillation at the beginning. This means that there is in fact at least two different phenomena that may cause transient resonant oscillations in the structure; an impact like wave force from steep to vertical waves that excites a wide spectrum of structural modes, and a higher harmonic wave load from waves, causing a resonant build up of the oscillations. To further confuse the picture, several papers, among others Chaplin et al. (1997) and (Huseby, 2000, part 3), reports of observations of a secondary load cycle shortly after the load from the wave crest when ringing is observed.

In this thesis ringing is defined as wave induced transient resonant oscillations in a structure, so both oscillations caused by a wave impact and those caused by higher harmonic wave forces are considered as ringing.

The effect of a wave slamming into a structure, contains the same mechanics that gives rise to the phenomena called whipping in ships. Whipping is caused by an impact in the bow or stern of the ship causes the hull girder to vibrate at it's resonant frequency. Since breaking waves are not considered in this thesis, little attention will be given to ringing induced by a slamming load.

The secondary load cycle seems to have gained much attention in several papers, and Grue and Huseby (2002) states that it might have an important contribution to the build up of the resonant oscillations in the body. They also found some indication that when a pronounced secondary load cycle is present, ringing occurs.

From experiments in moderate scale they report that the secondary load cycle seems to appear if $kr < 0.33$ and the following criterion for the Froude-number.

$$F_N = \frac{\omega\zeta_{max}}{\sqrt{gD}} > \approx 0.4 \tag{4.2}$$

In the small scale experiments it appears if $kr < 0.33$ and $0.3 < k\zeta_{max}$. According to the same paper, the secondary load cycle is more pronounced in single waves than in regular waves, but is has also occurred in regular waves.

According to Chaplin et al. (1997) the secondary load cycle has an amplitude of up to 8% of the main peak for the smallest cylinders, and up to 12% in the case of the larger cylinder. Grue and Huseby (2002) reports that the peak of the secondary load cycle seems to appear $\approx \frac{1}{4}$ wave period later than the peak.

In Rainey (2007), the ringing phenomenon is contributed to hydraulic jumps travelling around the cylinder. When waves are steep enough, the two hydraulic jumps seems to be created at each side of the cylinder. These ride the wave front and crash into each other on the rear side of the cylinder, causing large negative pressure forces and the reported secondary load cycle.

If ringing is solely caused by hydraulic jumps, it is not feasible to solve the problem using a perturbation technique. This is due to the strong non linearities present in hydraulic jumps of this kind (Rainey, 2007). In the conclusion of Grue and Huseby (2002) it is recommended that further work on the subject of a secondary load cycle should allow for a local breaking phenomenon.

It is difficult to say exactly if this kind of ringing is only a result of higher order forces, if it is a combination of higher order wave loads and hydraulic jumps or if it is solely due to these hydraulic jumps. If indeed the case that two local breaking waves are the true cause of the phenomenon, then the current theories should not be able to predict it. This is due to the fact that such an interaction needs to be modelled by a wave-structure technique, which allows for fully nonlinear effects.

Tromans et al. (2006) have performed an in-depth review of the existing knowledge about ringing and nonlinear loads on gravity based structures. They have reviewed the load formulation by FNV, and also Rainey's slender body theory.

They conclude that neither of the two model the nonlinear force components adequately. They also show that the nonlinearities in the incident wave field plays an important role. Further they conclude that in the absence of a possibility to accurately model both the nonlinearities in the incident wave field and the wave-structure interaction, the single most important step is to incorporate the best possible description of the incident wave field. Regarding the secondary load cycle they state:

“ *The rapid force reversals are, in large part, dependent upon the time taken for the fluid to move around the column. This is independent of the incident wave frequency and, consequently, the applied forces will not be well modelled by a series expansion based solely on the harmonics of the incident wave motion. Indeed, such an approach would be expected to give miss-leading results.” (Tromans et al., 2006, page 101)*

It appears then that the cause of transient resonant oscillations in the structures can be caused by either of the three; Higher order forces, usually said to be above third order, a breaking wave that hits the structure or the secondary load cycle that occurs.

It has been some concern, if offshore wind turbines might be subjected to ringing oscillations which may affect the maximum loads on the structure, and possibly affect the fatigue as well. The progress made to understand the phenomenon on gravity based structures, can more or less be transferred directly to the case of wind turbines.

In DNV - Design of Offshore Wind Turbine (Veritas, 2011) it is stated:

“ *For evaluation of load effects from wave loads, possible ringing effects shall be included in the considerations. When a steep, high wave encounters a monopile, high frequency nonlinear wave load components can coincide with natural frequencies of the structure causing resonant transient response in the global bending modes of the pile. Such ringing effects are only of significance in combination with extreme first order wave frequency effects. Ringing should be evaluated in the time domain with due consideration of higher order wave load effects.*” (Veritas, 2011, page 77)

It is thus clear that ringing must be accounted for in the design of offshore wind turbines, by demand from classification societies. As the quote states, the nonlinear wave load effect is considered to be important to the ringing response.

At only 20 [m] water depth, it is expected that the turbine might be subject to breaking waves. A breaking wave that hits the turbine, giving large slamming forces, can excite a broad range of frequencies. This kind of wave loads will correspond to the type of loading studied in Welch et al. (1999) which caused

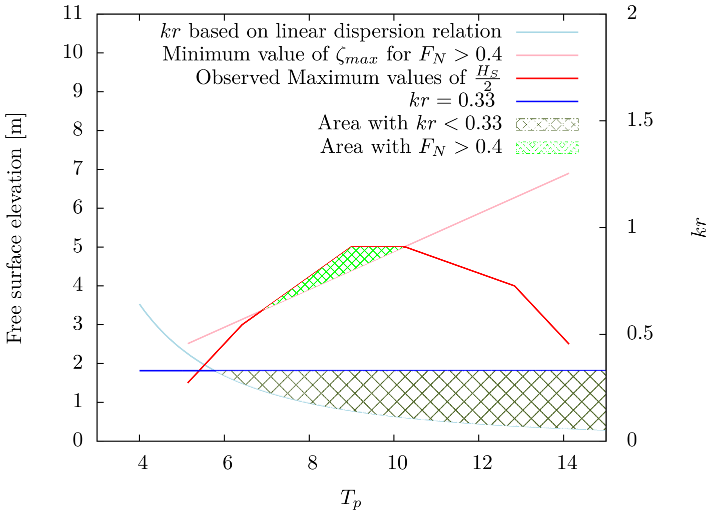

Figure 4.2: Areas where secondary load cycle should occur based on Grue and Huseby (2002).

ringing. So it is possible that wind turbine can experience ringing excited by breaking waves. This type of ringing will not be covered in this thesis, but more information on this topic can be found in e.g. Marino (2011), Marino et al. (2011) and Marino et al. (2013).

The criteria of the secondary load cycle in Grue and Huseby (2002) is here used as a criteria for when ringing could occur. This is chosen because it is not certain if the secondary load cycle will occur in the simulations, and evidence suggest it is important for ringing. So if it should have been present by the criteria established by Grue and Huseby (2002) and it does not appear, then it can be concluded that even better load models must be used.

If we investigate when the secondary load cycle occurs based on equation 4.2, for a cylinder with diameter $6[m]$, and use the requirement that $kr < 0.33$, then figure 4.2 can be created.

In the figure linear waves has been assumed, meaning that $\zeta_{max} = \frac{H}{2}$, and that the linear dispersion relationship is used to find wave number. The two uppermost curves shows the maximum values of the significant wave height observed, taken from table 2.2 (and transformed from T_z to T_p using relation 2.3 with $\gamma = 3.3$), and the minimum value of ζ_{max} necessary for a $F_N > 0.4$ as stated in equation 4.2.

The two lower curves show the line for $kr = 0.33$ and also the value of kr for a given T. The two lower curves has it's y-axis set on the right side of the figure, and the left y-axis is for the upper curves.

The two areas filled, with the two shades of green, shows the areas where the two conditions are satisfied independently (and real waves exists). What is observable is that for all values of T_P where there is registered wave amplitudes high enough to satisfy equation 4.2, the wave number is also low enough to satisfy $kr < 0.33$.

Since the significant wave height and peak frequency of the sea state have been used to compare with the needed wave amplitude, only a small proportion of the waves will actually have an maximum elevation high enough to make $F_N > 0.4$. Hence it is more correct to say that in the filled area there is sea states which may contain several waves that can cause a ringing response in the structure. Also outside the filled areas there is a possibility, albeit slim, for waves that can generate the secondary load cycle. This is because the the plot has been made on the statistical parameters H_s and T_p.

As a rule of thumb, based on figure 4.2 it appears that the wave amplitude needs to be of the same order as the tower radius for the secondary load cycle to occur. This is in line with the first observations of ringing where it was noted that it occurred when the wave height was of the same order as the structure's diameter.

The natural frequency of the tower's first bending mode is $\approx 0.28[Hz]$ as shown in section 2.4. This is within the range of third order wave forcing, meaning that the structure might be excited at it's natural frequency by a purely higher order load (i.e. not necessarily one that produces a secondary load cycle).

To summarise this section; Bottom fixed offshore wind turbines might possibly experience ringing oscillations. The dimensions of the turbine, and the environment it is subjected to, seem to give the possibility for both ringing caused by wave slamming, from a secondary load cycle or from purely higher harmonic load.

To investigate the occurrence of ringing in offshore wind turbines, a load model and wave model that are able to better predict higher order terms are possibly needed. In chapter 5 several alternatives for the prediction of loads will be reviewed. In chapter 6 two wave models that will be used are presented.

5 | Improved Force Model

To extend the capabilities of FAST to better include higher order loads, several possibilities regarding the loads have been investigated. For predicting ringing response there seems to be mainly four approaches; Faltinsen-Newman-Vinje (FNV), Malenica-Molin (MM), Rainey's slender body expressions and Computational fluid Dynamics (CFD).

A brief presentation of the characteristics of the four is given, so a choice of which model to use can be made. Further the chosen model is looked upon in more detail, along with a comparison with the existing load implementation in FAST.

5.1 Faltinsen - Newman - Vinje

Faltinsen, Newman and Vinje (FNV), have in (Faltinsen et al., 1995) developed a procedure to take into account the third order loads from large waves. The basic assumptions they have made are; infinite water, wavelength is long compared to the cylinder diameter, and that the wave height is of the same order as the cylinder diameter. The original paper considers regular waves, but the theory has later been extended to include irregular waves in Newman (1996).

They argue that the usual linear velocity potential of an regular incident wave is accurate to the third order if the dispersion relationship is written as:

$$\frac{\omega^2}{g} = k[1 + (kA)^2] \tag{5.1}$$

An argument is made that in a regular perturbation analysis the wave amplitude A is considered small. Not only to the wavelength λ, but also to the characteristic length scale of the structure. The waves of interest to ringing has however an amplitude A of comparable size to the cylinder radius, and thus it is necessary to reconsider the perturbation analysis under the assumption that $\frac{A}{r} = O(1)$.

This theory is thus different from the regular long wave theory since it allows for wave amplitude of comparable size to the cylinder radius. Because of this, a trick they use is to decompose the solution into two sub domains; an inner and an outer domain. In the outer domain a linear approach is valid, but in the inner domain significant nonlinearities exists, which is associated with the boundary condition on the free surface.

The solution of the velocity potential in the outer domain utilises the linear solution to a cylinder placed in incident waves found by MacCamy & Fuchs. Their solution is expanded to higher order under the assumption that $kr << 1$.

A similar approach is done in the inner domain, but a higher order potential is introduced as a correction to include the nonlinear effects. Due to nonlinearities related to the free surface boundary condition which the higher order potential needs to satisfy, the usual approach where one uses a Taylor approach to transfer the boundary condition to the plane $z = 0$ can not be used. They instead perform a Taylor expansion around the free surface elevation of the linear incident waves, meaning that the expansion is performed around a plane $z = A * \sin(\omega t)$. This approach is unconventional, but is claimed to give convergence in the series expansion.

In the paper, they have made the ad-hoc assumption that it can be used on finite water depth if it can be assumed that pressure field in the free surface is not significantly different from the case of infinite depth.

5.2 Malenica - Molan

In Malenica and Molin (1995) a classical perturbation technique has been carried out to the third order, meaning $(kA)^3$. The wave amplitude (or wave steepness) is considered to be of order ϵ and the wavelength and radius of the structure are unrestricted (of order 1). They assume a cylinder at a horizontal sea bed, with water depth h. The free surface boundary condition is transferred to the plane $z = 0$ in the usual way, and then the potential for the first three orders are found. They do not set restriction on a long wave compared to the structure, so these results are valid for all waves and structures, given the Stokes expansion converges.

5.3 Rainey's Slender Body Expressions

Rainey has in several papers presented a slender body theory that extends Morison's equation. This not based on the usual approach of integrating pressure over the surface, but on conservation of fluid energy. This development is done on the basis of a paper by Lighthill (1979). Rainey's arguments are presented in several papers, for instance Rainey (1989) and Rainey (1995a). He argues that an approach where one considers conservation of fluid kinetic energy is more efficient and require less knowledge about the flow. A simple 2D flow idealisation can be used to calculate the forces on a section.

The basic assumption in his derivations is that the shape of the water surface is unaffected by the presence of the structure, so that the the free surface can be described as a “Wavy-lid” in the shape of the incident wave. In his words; “This removes the free-surface degrees of freedom so the problem can be tackled by classical energy arguments” (Rainey, 1989). This assumption is in line with the classical long wave approximation where the presence of a slender structure is assumed to not affect the incident wave. In the same paper he shows that this approximation introduces errors of the third order in wave height, which is located at the free surface. This choice of free surface can actually be different, but this is merely the easiest choice. The important part is that the free surface degrees of freedom are known.

Rainey argues that when compared to a regular perturbation technique this model is accurate up to the second order with the error being of third order for the limiting case of small diameter cylinders. The theory also includes a load at the free surface which for a vertical cylinder will be of third order.

This process has not done a conventional expansion of the free surface to the plane z = 0, which means that this process can handle any wave, contrary to regular perturbation techniques where it is assumed that the wave height is small compared to all other length scales. Important nonlinear effects in the incident waves can be included in the force calculations since no requirements are placed on the incident waves.

5.4 Computational Fluid Dynamics

An alternative is to use computational fluid dynamics (CFD) to calculate the force on the structure from an incident wave. This will mean that the fluid domain is divided into a number of elements, the proper boundary conditions are imposed and then the governing equation (Navier-Stokes) is solved for each point in the domain for each time step. This method will solve the wave-structure interaction, and solution is found in the time domain. This means that the solution of one time step might affect the solution in the next time step. This solution will by far yield the most accurate results, and gives the possibility of performing fully nonlinear calculations. Computational fluid dynamics can solve all the three potential causes for ringing; slamming, higher order loads or the secondary load cycle.

The downside of CFD is that it is very time consuming, and might give unreliable results if the user is not skilled in meshing and creating the model.

5.5 Rationale for Selecting a Model

When it comes to selecting a load model to extend calculations in FAST, besides accuracy, one of the most important choices is how easy it can be implemented into FAST. This means that the basic assumptions that FAST is working under, should also be the same assumptions that the load model is based on. For instance, will FAST generate the whole time series of the wave elevation and the kinematics of the wave in the initialisation of the program, and are thereby assuming that the free surface elevation is unaffected by the structure.

Considering accuracy and possibility to model highly nonlinear effects, a CFD analysis is probably the best. CFD solution is the only one that should be able to predict a heavy structure wave interaction leading to two small hydraulic jumps travelling around the structure and colliding on the back. If this is indeed the real cause of the secondary load cycle, then this seems like the only way able to predict all aspects of ringing. However, the use of CFD is not feasible because of the calculation flow in FAST as it is today. If one is to implement a CFD calculation into the process, the free surface elevation of each time step, and it's interaction with the structure will influence the next, so that it is impossible to initialise the whole free surface elevation at the beginning. This clearly breaks with the how FAST works today, and means that lot of time must be spend on rewriting the code to implement such a feature. Thus it is not practically feasible within the scope of this thesis to perform such a work.

The FNV model is assuming deep water, but with the ad-hoc assumption that it can be used on finite water if the pressure field is not significantly affected by the sea bed. This assumption can not be assumed valid in the case of only 20 [m] depth, and with wave heights up to (7-8) m. With the current problem, using FNV will mean that it is applied outside the range of where it could be said to be valid. Also the fact that this theory assumes a regular wave, developed by stokes expansion, means that several highly nonlinear effects in the incident waves are not accounted for. An example of the kind of nonlinearity not accounted for would be the steep asymmetric waves.

MM's approach is as mentioned to perform a regular perturbation technique. In appendix B of Rainey (1995a) this technique is claimed to be diverging for the case where the waves are at the same amplitude as the structural diameter. This also utilises waves up to third order, so it might not take into consideration some of the highly nonlinear effects in a real sea.

Rainey's slender body expressions can handle any wave, as long as it is assumed that the structure does not affect the wave elevation. This is the usual long wave approximation, which is the one that FAST is presently using. The expressions can be considered as an extension of the currently used Morison's equation, which means that it should be easy to extend the existing load model to this one.

Rainey's expressions is the only model that can be easily coupled with FAST, and can handle highly nonlinear waves, thereby making it the best candidate for extending the load model in FAST.

When it comes to the possibility for predicting ringing, Tromans et al. (2006, p. 102) states that the high frequency force cannot be adequately modeled by the present models (FNV and Rainey). However they state that the best available solution seems to be Rainey's equations, since these allow for the use of a fully nonlinear wave model, allowing some nonlinear components in the wave to be included.

The conclusion is to utilise Rainey's expressions for the load and couple it with nonlinear waves. It is not certain that this will be able to produce the load history that is observed in experiment (specifically the second load cycle), but it seems to be the best existing solution out there, which can easily be coupled with the framework needed for wind turbine analyses.

5.6 Detailed Investigation of Chosen Load Model

As mentioned, the derivation of Rainey's slender body expressions is based on conservation of energy arguments. The derivation can be found in Rainey (1989). It is quite difficult to follow, but the results he ends up with, partly summarised in Rainey (1995a), are simple. The derivations will not be covered in detail, but the basic assumptions needs to be discussed.

As mentioned in section 5.3 the basic assumption in his derivations is that the shape of the water surface is unaffected by the presence of the structure. This is so that the the free surface can be described as a “Wavy-lid” in the shape of the incident wave. In the case of a slender structure this is realistic, since the structure will only set up a small diffraction potential which effect on the free surface elevation may be neglected. The turbine of interest is already classified to be mass dominated in the long wavelength regime in section 2.6. The assumption of a “Wavy-lid” is not essential, it is merely the simplest choice. In the appendix of Rainey (1995a) and in the main text of Rainey (1989), the error introduced by the wavy-lid is investigated. When using conventional Stokes categorisation of wave loads as first order, second order etc., where the order is dependent on the wave amplitude, he states that the error introduced by the wavy-lid is of third order.

The assumption of a slender structure leads to large errors if the structure is in fact not slender. He states that if the wave length is shorter than about 10 cylinder diameters, it appears that the second order/second harmonic seems to have serious errors. As seen in section 2.6 there are only observed a few sea states where the peak period gives a wave length smaller than 10 cylinder diameters.

Comparison between slender body loads and diffraction loads is performed in Taylor et al. (1992). They show that for cases where the wavelength is too short, important contributions from the microseism effect, which is a non-slender effect, is neglected by Rainey’s theory. Generally speaking, the use of a slender body assumptions means that one is neglecting far field effects, such as the waves generated by the structure.

The derivation gives the load from a potential flow on a slender structure, which can be divided into five contributions:

- Force per unit immersed length
- Axial torque per unit immersed length
- Point loads at joints
- Point loads at surface intersections
- Point load at submerged ends

For an offshore wind turbine, with a constant circular cross section, there will be no axial torque loads. This load can be thought of as a 2D example of the Munk moment, which is present in all bodies with non-isotropic added mass (Rainey, 1995a). The case of a circular cross section has isotropic added mass, so no axial torque should be present. There will neither be a point load at joints or loads at submerged ends, since there are no joints in the structure and the end of the turbine is buried in the seabed. The terms which are not present for this kind of structure will not be presented here, but can be found in Rainey (1995a).

The load on a submerged cross section is then given as:

$$\begin{aligned} \mathrm{d}F_I = \rho\frac{\pi D^2}{4}[\mathbf{a}-\mathbf{g}]_{\mathbf{T}} + \mathbf{M}[\mathbf{a}+(\mathbf{l}\cdot\mathbf{V'l})\mathbf{W}] - \mathbf{M}\frac{\partial\mathbf{U}}{\partial\mathbf{t}} \\ -2\mathbf{M}\boldsymbol{\Omega}\mathbf{W_A} + [(\mathbf{V'}+\boldsymbol{\Omega})\mathbf{MW}]_{\mathbf{T}} - \mathbf{M}(\mathbf{V'}+\boldsymbol{\Omega})\mathbf{W_T} \end{aligned} \tag{5.2}$$

Where $\mathbf{a}$ is the acceleration vector including convective terms, $\mathbf{M}$ is the added mass matrix, $\mathbf{g}$ is the gravitational acceleration vector, $\boldsymbol{V'}$ is the velocity gradient matrix in the incident waves. $\mathbf{U}$ is the velocity vector of the center point of the cylinder cross section, $\mathbf{V}$ is the velocity vector of particles in the incident waves, $\mathbf{l}$ is a unit vector along the cylinder axis, $\mathbf{W}$ is the relative velocity between waves and cylinder $\mathbf{W} = \mathbf{V\text{-}U}$, $\boldsymbol{\Omega}$ is the matrix defined as $\Omega\boldsymbol{x} = \omega \times \boldsymbol{x}$ where $\mathbf{x}$ is any vector and ω is the angular velocity of the structure. The suffixes A and T denotes axial and transverse components.

According to Jefferys and Rainey (1994) the acceleration shall include the convective terms. The same is used by Chaplin et al. (1997), Iwanowski et al. (2011) and Tromans et al. (2006). The total acceleration for a_x is given as:

$$a_x = \frac{\partial u}{\partial t} + u\frac{\partial u}{\partial x} + v\frac{\partial u}{\partial y} + w\frac{\partial u}{\partial z} \tag{5.3}$$

Similar expressions for the other components in $\boldsymbol{a} = (a_x, a_y, a_z)$ are used.

According to Rainey (1995a), the first two terms agree with terms derived by pressure integration independently by Manners in Manners and Rainey (1992). The term $\mathbf{M(l\cdot V'l)W}$ is the axial divergence term, and a lengthy discussion of the physical reason for the term is found in Manners and Rainey (1992). Here it is sufficient to say that the term seems to be related to the rate of change in added mass.

The third and fourth terms are extending the force to that of a moving cylinder, where the first of the two are an added mass inertial reaction and the second is a "negative centrifugal force" (Rainey, 1995a). If we assume that the yaw motion of the wind turbine is negligible, then the fourth term may be dropped. From a hydrodynamic point of view there is no force that creates a yaw motion, but, the rotor may impose a yaw moment on the structure. However, since this is a steel structure and it is considered clamped at the sea bed the yaw motion induced by the rotor will be limited, hence it is safe to drop the this term.

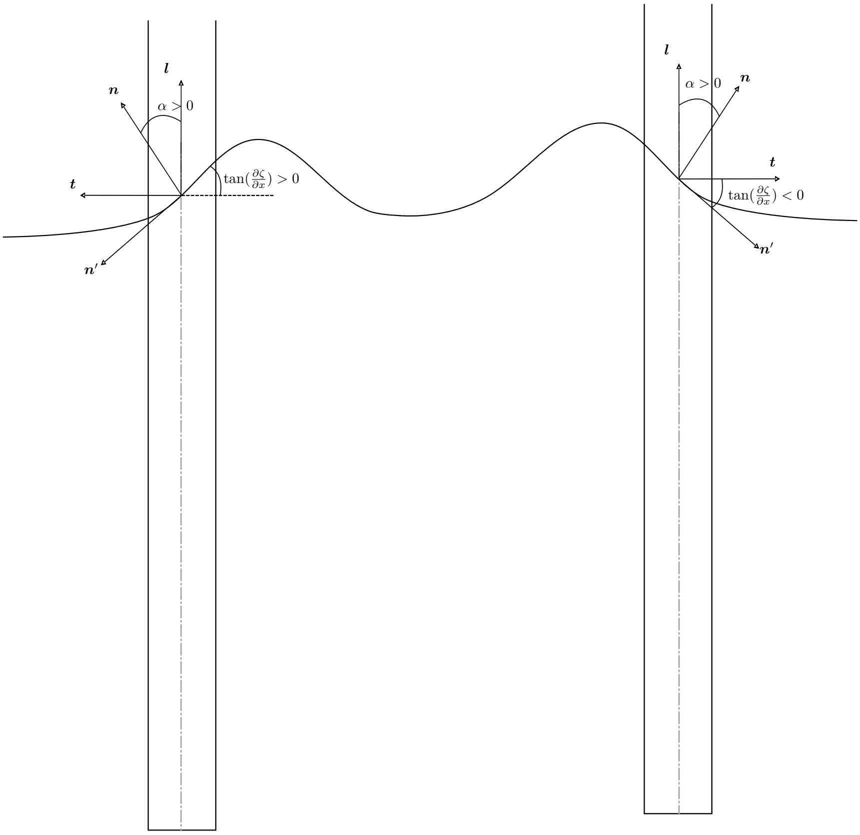

Figure 5.1: Definition of vectors and angles to be used in Rainey's slender body expressions. Case 1 is to the left and case 2 to the right.

The last two terms terms will cancel each other out for a circular cylinder with symmetric added mass.

The $\boldsymbol{l}$-vector should be the instantaneous axis of the element. However to ease the implementation, this has been set to be $\boldsymbol{l} = [0, 0, 1]$. This can be done for two reasons: The first is that this is a fairly stiff steel structure, with small deflections at the tower top, thus deflections at the sea level are even smaller. The second reason is that when FAST is utilising wave kinematics, all quantities have been calculated at the undeflected position of the structure. This means that there is already used an approximation of small deflections in FAST.

At the surface intersection the following force is present:

$$F_{SI} = \frac{1}{2}\tan(\alpha)[(\boldsymbol{t} \cdot \boldsymbol{w})\boldsymbol{M}\boldsymbol{w} - (\boldsymbol{t} \cdot (\boldsymbol{l} \times \boldsymbol{M}\boldsymbol{w}))(\boldsymbol{l} \times \boldsymbol{w})] \tag{5.4}$$

Where α is the angle between the cylinder axis and the surface normal of the undisturbed wave, and $\mathbf{t}$ is a unit vector in their joint plane, normal to the cylinder axis and pointing out of the fluid. The second term is zero for a case of a vertical cylinder (Jefferys and Rainey, 1994). This has also been proved in appendix B.3.

Figure 5.1 shows the definitions of the various vectors used in the expression. Two different cases exists, defined by whether the wave crest has passed the centre line or not. What is important to notice is that the different definitions of the quantities.

The left side of the figure is to represent case 1, and the right side to represent case 2.

The calculations will be performed in a local coordinate system where the waves are propagating in a local $x-$direction (This is explained in details in appendix C.1). Then the following can be used for the definitions of α and $\boldsymbol{t}$.

For case 1, $\boldsymbol{t} = [-1 \ 0 \ 0]$, and $\alpha = \tan^{-1}(\frac{\partial\zeta}{\partial x})$. For case 2 $\boldsymbol{t} = [1 \ 0 \ 0]$, and $\alpha = -\tan^{-1}(\frac{\partial\zeta}{\partial x})$. In section 5.7 it will be shown that since the two changes sign asymmetricly, then the force will be the same for both cases.

According to Faltinsen et al. (1995) Rainey and FNV are consistent for the loads proportional to A^2 and A^3, but a significant error exists for the term proportional to A^3. These slender body expressions predicts a force $\frac{1}{8}$th of the results of FNV (Faltinsen et al., 1995).

In Rainey (1995b) there is developed an additional force called surface distortion force, to account for the discrepancy between FNV and this theory. This can be derived by assuming that the additional force is due to the rate-of-change of the energy stored in the surface distortion. However in Chaplin et al. (1997) it is argued that this should not be included, since in the case considered in that paper,the incident waves based on Stokes expansion should have diverged, so that it is irrelevant to compare with these theories. Comparison between experiments in the paper supports the view that this force should not be included in steep waves, and so it is not used in the load model implemented in FAST.

The model can be extended to include viscous drag by adding the drag term from the classical Morison's equation. This has been added with the relative velocity between the water particles and the structure. This force component on a section is calculated as:

$$\mathrm{d}F_D = \frac{\rho}{2} C_D D |\mathbf{V} - \mathbf{U}|(\mathbf{V} - \mathbf{U})\mathrm{dz} \tag{5.5}$$

where $\boldsymbol{V}$ is the particle velocity in the incident wave, and $\boldsymbol{U}$ is the velocity of the structure cross section.

To find the total force on the submerged part of the cylinder, the force is integrated over the instantaneous wetted surface.

5.7 Comparing the Old and the New Load Model

In appendix A.1, the load components on the tower when linear incident waves with wheeler stretching is used, and forces are calculated by Morison's equation, have been calculated analytically. To be able to compare the two load models, the same technique is performed here to identify the load components.

In order to make the mathematics manageable, the structure is assumed to be a perfectly stiff vertical cylinder that is present in long crested incident regular waves. Th waves are propagating in the x-direction, with a mean water depth of 20 [m]. The incident waves are given by linear theory, but with the modification introduced by wheeler stretching.

First it is appropriate to extend the terms in the load on a submerged section. For a stiff circular cylinder the terms present is the following:

$$\mathrm{d}F_I = \rho \frac{\pi D^2}{4} \mathbf{a_T} + \mathbf{M}[\mathbf{a} + (\mathbf{l} \cdot \mathbf{V'l})\mathbf{W}] \tag{5.6}$$

$$
\begin{aligned}
&\mathrm{d}F_I = \\
&\rho\frac{\pi D^2}{4}\begin{bmatrix}\frac{\partial u}{\partial t}+u\frac{\partial u}{\partial x}+v\frac{\partial u}{\partial y}+w\frac{\partial u}{\partial z}\\ \frac{\partial v}{\partial t}+u\frac{\partial v}{\partial x}+v\frac{\partial v}{\partial y}+w\frac{\partial v}{\partial z}\\ 0\end{bmatrix}+\begin{bmatrix}m_x & 0 & 0\\ 0 & m_y & 0\\ 0 & 0 & 0\end{bmatrix}\begin{bmatrix}\frac{\partial u}{\partial t}+u\frac{\partial u}{\partial x}+v\frac{\partial u}{\partial y}+w\frac{\partial u}{\partial z}\\ \frac{\partial v}{\partial t}+u\frac{\partial v}{\partial x}+v\frac{\partial v}{\partial y}+w\frac{\partial v}{\partial z}\\ 0\end{bmatrix}\\
&+\begin{bmatrix}m_x & 0 & 0\\ 0 & m_y & 0\\ 0 & 0 & 0\end{bmatrix}\left(\begin{bmatrix}0\\0\\1\end{bmatrix}\cdot\begin{bmatrix}\frac{\partial u}{\partial x} & \frac{\partial u}{\partial y} & \frac{\partial u}{\partial z}\\ \frac{\partial v}{\partial x} & \frac{\partial v}{\partial y} & \frac{\partial v}{\partial z}\\ \frac{\partial w}{\partial x} & \frac{\partial w}{\partial y} & \frac{\partial w}{\partial z}\end{bmatrix}\begin{bmatrix}0\\0\\1\end{bmatrix}\right)\begin{bmatrix}u\\v\\w\end{bmatrix}
\end{aligned}
\tag{5.7}
$$

The fact that the cylinder is stiff means that the relative velocity is just the velocities in the incident waves, and that the $\boldsymbol{l}$-vector is always vertical. Since the waves are propagating in the x-direction, all quantities including the velocity in the y-direction are zero. Since the waves are long crested waves, it means that there will be no variation in the y-direction as well, so all differentiation with respect to y are zero. By performing the operations, introducing the said properties of the velocities, the equation reduces to the following:

$$\mathrm{d}F_x = (\rho\frac{\pi D^2}{4} + m_x)(\frac{\partial u}{\partial t} + u\frac{\partial u}{\partial x} + w\frac{\partial u}{\partial z}) + m_x\frac{\partial w}{\partial z}u \tag{5.8}$$

This result is valid for all incident waves towards a stiff circular cylinder.

We see that the first term is just the Morison inertia loading, except that the acceleration has included the convective accelerations. Morison's equation is usually used without these, especially when a linear waves are used. This is because the additional convective terms are non-linear and would produce a higher order load. The last term is the axial divergence term, which according to Manners and Rainey (1992) seems to be producing a load related to the rate of change in added mass.

To compare with the existing calculations, a linear incident wave is introduced with wheeler stretching. The wave profile of this is given as:

$$\zeta = \zeta_a \sin(\omega t - kx) \tag{5.9}$$

Then the velocity component in the x-direction is given as:

$$u = \omega\zeta_A\frac{\cosh(k(z+h))}{\sinh(kh)}\sin(\omega t - kx) \tag{5.10}$$

In z-direction:

$$w = \omega\zeta_A \frac{\sinh(k(z+h))}{\sinh(kh)} \cos(\omega t - kx) \tag{5.11}$$

In quick succession the needed differentiated quantities are given as:

$$\frac{\partial u}{\partial t} = \omega^2\zeta_A \frac{\cosh(k(z+h))}{\sinh(kh)} \cos(\omega t - kx) \tag{5.12}$$

$$\frac{\partial u}{\partial x} = -k\omega\zeta_A \frac{\cosh(k(z+h))}{\sinh(kh)} \cos(\omega t - kx) \tag{5.13}$$

$$\frac{\partial u}{\partial z} = k\omega\zeta_A \frac{\sinh(k(z+h))}{\sinh(kh)} \sin(\omega t - kx) \tag{5.14}$$

$$\frac{\partial w}{\partial z} = k\omega\zeta_A \frac{\cosh(k(z+h))}{\sinh(kh)} \cos(\omega t - kx) \tag{5.15}$$

Introducing the quantities into equation 5.8, the following is obtained.

$$\begin{aligned}
&\mathrm{d}F_x = (\rho\frac{\pi D^2}{4} + m_x)\omega^2\zeta_A \frac{\cosh(k(z+h))}{\sinh(kh)} \cos(\omega t - kx) + \\
&(\rho\frac{\pi D^2}{4} + m_x) * \omega\zeta_A \frac{\cosh(k(z+h))}{\sinh(kh)} \sin(\omega t - kx) * -k\omega\zeta_A \frac{\cosh(k(z+h))}{\sinh(kh)} \cos(\omega t - kx) + \\
&(\rho\frac{\pi D^2}{4} + m_x) * \omega\zeta_A \frac{\sinh(k(z+h))}{\sinh(kh)} \cos(\omega t - kx) * k\omega\zeta_A \frac{\sinh(k(z+h))}{\sinh(kh)} \sin(\omega t - kx) + \\
&m_x * k\omega\zeta_A \frac{\cosh(k(z+h))}{\sinh(kh)} \cos(\omega t - kx) * \omega\zeta_A \frac{\cosh(k(z+h))}{\sinh(kh)} \sin(\omega t - kx)
\end{aligned} \tag{5.16}$$

In appendix B.1 the details of the simplification of equation 5.16 is performed, with the end result given in equation 5.17.

$$\begin{gathered}
\mathrm{d}F_x = (1 + C_A)\rho\frac{\pi D^2}{4}\omega^2\zeta_A \frac{\cosh(k(z+h))}{\sinh(kh)} \cos(\omega t) + \\
(C_A \sinh^2(k(z+h)) - 1)\rho\frac{\pi D^2}{4} k\omega^2\zeta_A^2 \frac{1}{\sinh^2(kh)} \frac{1}{2} \sin(2\omega t)
\end{gathered} \tag{5.17}$$

Where C_A is the added mass coefficient.

This force can be integrated to the free surface elevation, and since wheeler stretching is utilised, the modified coordinates should be used. The first line in eq. 5.17 is equal to the term that is integrated in appendix A.1, so it will not be treated here.

The force from the second line will be given by:

$$F = \int_{-h}^{\zeta} (C_A \sinh^2(k(\frac{z-\zeta}{1+\frac{\zeta}{h}}+h))-1)\rho\frac{\pi D^2}{4}k\omega^2\zeta_A^2\frac{1}{\sinh^2(kh)}\frac{1}{2}\sin(2\omega t)\mathrm{dz} \tag{5.18}$$

$$F = \rho\pi r^2 k\omega^2\zeta_A^2\frac{1}{\sinh^2(kh)}\frac{1}{2}\sin(2\omega t)\int_{-h}^{\zeta}(C_A \sinh^2(k(\frac{z-\zeta}{1+\frac{\zeta}{h}}+h))-1)\mathrm{dz} \tag{5.19}$$

The integral is solved in appendix B.2, with the total force from this term given in eq. 5.20

$$\begin{aligned}
F = \rho\pi r^2 k\omega^2\zeta_A^3\frac{1}{\sinh^2(kh)}(\frac{1}{16}C_A\frac{1}{kh}\sinh(2kh)-\frac{1}{4}(\frac{C_A}{2}+1))\cos(\omega t) \\
+\rho\pi r^2 k\omega^2\zeta_A^2\frac{1}{\sinh^2(kh)}(\frac{1}{8}C_A\frac{1}{k}\sinh(2kh)-\frac{1}{2}h(\frac{C_A}{2}+1))\sin(2\omega t) \\
+\rho\pi r^2 k\omega^2\zeta_A^3\frac{1}{\sinh^2(kh)}(\frac{1}{4}(\frac{C_A}{2}+1)-\frac{1}{16}C_A\frac{1}{kh}\sinh(2kh))\cos(3\omega t)
\end{aligned} \tag{5.20}$$

The total integrated force on the structure, including the solution to the first line of equation 5.17 is then :

$$\begin{aligned}
F = \rho\pi r^2\zeta_A\omega^2[\frac{(C_A+1)}{k}+\frac{\zeta_A^2 k}{\sinh^2(kh)}(\frac{1}{16}C_A\frac{1}{kh}\sinh(2kh)-\frac{1}{4}(\frac{C_A}{2}+1))]\cos(\omega t) \\
+\rho\pi r^2\omega^2\zeta_A^2[\frac{(C_A+1)}{2kh}+\frac{k}{\sinh^2(kh)}(\frac{1}{8}C_A\frac{1}{k}\sinh(2kh)-\frac{1}{2}h(\frac{C_A}{2}+1))]\sin(2\omega t) \\
+\rho\pi r^2 k\omega^2\zeta_A^3\frac{1}{\sinh^2(kh)}[\frac{1}{4}(\frac{C_A}{2}+1)-\frac{1}{16}C_A\frac{1}{kh}\sinh(2kh)]\cos(3\omega t)
\end{aligned} \tag{5.21}$$

For the component at the free surface intersection, the force is given as:

$$F_{SI} = \frac{1}{2}\tan(\alpha)[(\boldsymbol{t}\cdot\boldsymbol{w})\boldsymbol{M}\boldsymbol{w} - (\boldsymbol{t}\cdot(\boldsymbol{l}\times\boldsymbol{M}\boldsymbol{w}))(\boldsymbol{l}\times\boldsymbol{w})] \tag{5.22}$$

The value of $\tan(\alpha)$ has two different definitions, as shown in figure 5.1. From geometry considerations it is clear that

$$|\alpha| = |\tan^{-1}(\frac{\partial\zeta}{\partial x})| \tag{5.23}$$

The case on the left side of figure 5.1 shows:

$$\tan(\alpha) = \tan(\tan^{-1}(\frac{\partial\zeta}{\partial x})) = \frac{\partial\zeta}{\partial x} \tag{5.24}$$

and on the right side

$$\tan(\alpha) = \tan(-\tan^{-1}(\frac{\partial\zeta}{\partial x})) = -\frac{\partial\zeta}{\partial x} \tag{5.25}$$

As mentioned the $\boldsymbol{t}$-vector is given as in section 5.6 with $\boldsymbol{t} = [-1, 0, 0]$ for the left case, and $\boldsymbol{t} = [1, 0, 0]$ for the right case.

The details of the derivation of the load on the two cases can be found in appendix B.3, with the end result given as:

Left case:

$$F_{SI} = -\frac{1}{2}\frac{\partial\zeta}{\partial x}m_x u^2 \tag{5.26}$$

Right case:

$$F_{SI} = -\frac{1}{2}\frac{\partial\zeta}{\partial x}m_x u^2 \tag{5.27}$$

So it is clear that the expression for the force will be exactly the same for both cases in figure 5.1. This is because $\boldsymbol{t}$ and $\tan(\alpha)$ will change signs asymmetrically.

Introducing the expressions for the velocity, and wave slope into equation 5.27. Note that there is no need to change the coordinates, since the principle of wheeler stretching is to use the wave kinematics from $z = 0$ at the free surface, it is simpler to just put $z = 0$ at the un-stretched expression.

$$
\begin{aligned}
F_{SI} &= -\frac{1}{2}(-k\zeta_A\cos(\omega t))m_x(\omega\zeta_A\frac{\cosh(kh)}{\sinh(kh)}\sin(\omega t))^2 \\
&= \frac{1}{2}m_x k\zeta_A^3\omega^2\frac{\cosh^2(kh)}{\sinh^2(kh)}\cos(\omega t)\sin^2(\omega t)
\end{aligned}
\tag{5.28}
$$

$$
\begin{aligned}
F_{SI} &= \frac{1}{2}m_x k\zeta_A^3\omega^2\frac{\cosh^2(kh)}{\sinh^2(kh)}\frac{1}{4}(cos(\omega t) - cos(3\omega t)) \\
&= \frac{1}{8}\rho\pi r^2 C_A k\zeta_A^3\omega^2\frac{\cosh^2(kh)}{\sinh^2(kh)}(cos(\omega t) - cos(3\omega t))
\end{aligned}
\tag{5.29}
$$

Introducing this into the expression in eq. 5.21 gives the total force on a stiff cylinder in regular waves with wheeler stretching and forces by Rainey's expressions.

$$
\begin{aligned}
&F_{Rainey} = \\
&\rho\pi r^2\zeta_A\omega^2[\frac{(C_A+1)}{k} + \frac{k\zeta_A^2}{\sinh^2(kh)}(\frac{1}{16}C_A\frac{1}{kh}\sinh(2kh) - \frac{1}{4}(\frac{C_A}{2}+1) + \frac{C_A}{8}\cosh^2(kh))]\cos(\omega t) \\
&+ \rho\pi r^2\omega^2\zeta_A^2[\frac{(C_A+1)}{2kh} + \frac{k}{\sinh^2(kh)}(\frac{1}{8}C_A\frac{1}{k}\sinh(2kh) - \frac{1}{2}h(\frac{C_A}{2}+1))]\sin(2\omega t) \\
&+ \rho\pi r^2 k\omega^2\zeta_A^3\frac{1}{\sinh^2(kh)}[\frac{1}{4}(\frac{C_A}{2}+1) - \frac{1}{16}C_A\frac{1}{kh}\sinh(2kh) - \frac{C_A}{8}\cosh^2(kh)]\cos(3\omega t)
\end{aligned}
\tag{5.30}
$$

The expression for the loading by the inertia term in Morison's equation is developed in appendix A.1, and is given as:

$$
F_{Morison} = \rho\pi r^2(1+C_A)\omega^2\frac{\zeta_A}{k}\cos(\omega t) + \rho\pi r^2(1+C_A)\omega^2\frac{\zeta_A^2}{2kh}\sin(2\omega t) \tag{5.31}
$$

By comparison it is clear that the important differences exist between the two load models. For the first harmonic load there has been the inclusion of some higher order terms that depends on ζ_A^3. These terms are expected to be very small due to the dependence on $\frac{k}{\sinh^2(kh)}$ while the first order term is dependent on $\frac{(C_A+1)}{k}$.

The second harmonic term also includes additional terms, which are expected to have a bigger contribution, since one of them depend on $\frac{\sinh(2kh)}{\sinh^2(kh)}$ which should be more significant than the extra terms for the first harmonic.

Lastly, third harmonic loads are not present at all when using Morison's equation.

6 | Improved Wave Models

There are two reasons for why the wave model in FAST should be improved. Firstly, there is a need to validate the proposed load model with experiments. If a load model with more accurate kinematics is used in the validation, more confidence can be put at the results. The experiments have been performed with regular waves, so a need for a nonlinear regular wave model is present.

Secondly, the conclusion made in section 5.5, is to use Rainey's slender body expressions together with nonlinear incident waves. The nonlinear waves are needed in order to obtain accurate kinematics also for steep waves. Steep waves are known to have asymmetric front and back, this is a feature that a regular wave train can not easily model.

In the project thesis several waves were reviewed, and the conclusion reached was to use a mixed-Eulerian-Lagrangian method to simulate fully nonlinear waves. This model is presented here, along with a wave model presented by Fenton (1988) which will be used to create nonlinear regular waves. The Fenton model was chosen because it is easy to implement into FAST, and due to it's capability of handling a large range of waves with varying degree of nonlinearity.

6.1 Fenton

In among others, Fenton (1988) presents a Fourier approximation method for steady waves, along with the code for a Fortran program to solve the problem. At the homepage of John D. Fenton [1] there is an updated version of the program freely available.

---

[1] http://www.johndfenton.com/

The technique is trying to overcome the difficulties regarding Stokes waves and Cnoidal theory. Stoke waves, based on a conventional perturbation theory assumes small wave amplitude, and breaks down in shallow waters. Cnoidal theory is an explicit theory for shallow waters, which breaks down in deeper water. To have an accurate representation, both are dependent on wave a height small with respect to the wavelength. These methods are solving the problem analytically, but the procedure proposed by Fenton is a numerical approximation.

The original paper gives a short history of the method of Fourier approximation, and a link to other related methods such as Stream theory. Details of stream theory can be found in e.g. Dean and Dalrymple (1984).

According to the user guide Fenton (2012), the method could be described as a nonlinear spectral approach. First a series solution is assumed, where each term satisfies the field equation, and then the coefficient for each term is found by solving a system of nonlinear equations. In Fenton's approach the coefficients are found by solving the nonlinear governing equations by Newton's method. According to the user guide, the only numerical approximation introduced in the calculations are the truncation of the Fourier series, and the numerical methods can obtain accurate solutions up to the highest possible waves. This means that this method should incorporate as much as possible of the nonlinearities in regular waves.

The present program is said to break down in the limit of very high and very long waves, where the Fourier series needs to represent the sharp crest and long and virtually flat through. A solution for a wave with $\lambda/h = 50$ and H/h is shown in the user guide.

The theory of the program might be found in both Fenton (1988) and also in the appendix of the user guide mentioned (Fenton, 2012).

This method presents an simple, but accurate, way of obtaining nonlinear regular waves that might be used in the calculations to validate the load model. Since the solution to the various parameters is a Fourier series, it is easy to implement them into the existing framework of FAST. The process of implementing these waves is found in appendix C.1.2.

6.2 Mixed Eulerian-Lagrangian Approach

In Marino (2011) and Marino et al. (2011) a fully nonlinear wave model is developed in order to model breaking waves. The model has been developed based on, among others, Longuet-Higgins and Cokelet (1976) and Nakayama (1990).

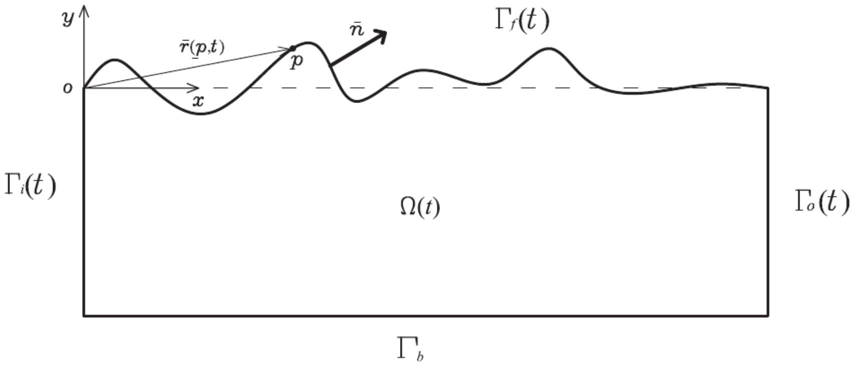

Figure 6.1: Domain of simulation, taken from Marino et al. (2011).

The process is called a mixed-Eulerian-Lagrangian approach. This is a two step procedure. First at time t the potential in the domain is solved using a higher order boundary element method (HOBEM). Then in the second step the free surface is stepped forward in time a distance Δt with a Taylor expansion in time. Then the boundary value problem is again solved using HOBEM, before another time step is undertaken.

The usual assumptions of an ideal fluid is used, making the solution a potential flow method.

An inertial coordinate system is fixed in the x direction, and has the y axis pointing upwards. As can be seen on figure 6.1, points on the free surface are tracked by the Lagrangian position vector $\bar{r}(p,t) = x_f \bar{e}_x + y_f \bar{e}_y$, where $\bar{e}_x$ and $\bar{e}_y$ are the unit normal vectors.

The velocity potential for each point in the domain $\Omega(t)$ can be described by Laplace's equation:

$$\nabla^2 \phi(p,t) = 0 \tag{6.1}$$

The domain is bounded by the four boundaries, $\Gamma_i(t), \Gamma_o(t), \Gamma_b \; and \; \Gamma_f(t)$. For all boundaries except the free surface, a Neumann-boundary condition is given as:

$$\boldsymbol{V}^n(p,t) = \nabla\phi(p,t) \cdot \bar{n} \tag{6.2}$$

Where $\boldsymbol{V}^n$ is the flux of the velocity through the boundary, and $\bar{n}$ is the normal vector.

The dynamic free surface boundary condition can be written as

$$\frac{D\phi(p,t)}{Dt} = -\frac{p_A}{\rho} - g\zeta + \frac{1}{2}\nabla\phi(p,t)\cdot\nabla\phi(p,t) \quad \text{for } p \,\epsilon\, \Gamma_f(t) \tag{6.3}$$

The kinematic free surface boundary condition is written as

$$\frac{D\bar{r}(p,t)}{Dt} = \nabla\phi \quad \text{for } p \,\epsilon\, \Gamma_f(t) \tag{6.4}$$

The boundary value equations are taken from Marino et al. (2011), and it is observable that they are slightly different from the ones given in section 2.5, as they are written in the Lagrangian reference system.

To solve the problem in the time domain, the geometry and velocity potential of the free surface must be known at $t = t_0$. This initial value, is then used as input for the time marching algorithm.

To perform the time marching, and find the propagation of the free surface in time, a Taylor expansion might be utilised, expanding the position vector $\bar{r}(p,t)$ and velocity potential ϕ in time by:

$$\bar{r}(p,t+dt) = \bar{r}(p,t) + \frac{D\bar{r}(p,t)}{Dt}dt + \frac{1}{2}\frac{D^2\bar{r}(p,t)}{Dt^2}dt^2 + O(dt^3) \tag{6.5}$$

$$\phi(p,t+dt) = \phi(p,t) + \frac{D\phi(p,t)}{Dt}dt + \frac{1}{2}\frac{D^2\phi(p,t)}{Dt^2}dt^2 + O(dt^3) \tag{6.6}$$

The velocity potential to be expanded like this is the potential on the free surface.

The series expansion is truncated after the second order term. According to Marino (2011) this seems to be the optimum choice because of numerical effort to compute higher order coefficients. While stokes expansion is an expansion in space, this expansion is in time. This means that the potential and position vector is expressed at the next time step as a function of value this time step, along with the “rate of change” and “rate of change in rate of change”. This is completely analogue to the case of expressing position in the next time step as a function of position this time step along with velocity and acceleration at this time step.

In Marino et al. (2013) it is reported of a fourth order Runge-Kutta method for the time marching, and it is stated that this is preferred over a Taylor expansion due to better stability.

The process of finding the Lagrangian derivatives are described in detail in Marino (2011), and will not be treated here. It is however worth mentioning that the second order coefficient/second order Lagrangian derivative is found by solving a boundary value problem, and this is true for all coefficients of higher order according to (Nakayama, 1990). This may sound time consuming, but in fact the formulation of the problem is the same as for finding the velocity potential. The geometry is the same, the only difference is in the boundary condition values.

By using this technique, two boundary value problems are solved for each time step. The first is to find the velocity potential, and the second is to find the solution to the problem $\nabla\dot{\phi}$. These problems have been solved by utilising a boundary element method, with higher order elements to discretise the boundary value problem.

To summarise the method, it is easy to think of it as a two step procedure:

1. Eulerian step: At a time t, the free surface and the velocity potential on the free surface is known. The flux on the boundaries Γ_i and Γ_o is also known. Then the two fluxes $\nabla\phi \cdot \bar{n}$ and $\nabla\dot{\phi} \cdot \bar{n}$ on the free surface are found by a boundary element method.
2. Lagrangian step: The free surface and the velocity potential on it are updated in time, to the next time step, providing boundary values for the next Eulerian time step.

According to Marino (2011) two instabilities occurred for this solution scheme. The first one is a strong instability related to too large time steps. This is easily managed by setting the time steps small enough. The second instability is what is named a saw tooth instability, which means that the surface gets the appearance of the working edge of a saw. This can be fixed by a smoothing technique where the value of a node is smoothed with a 5 point smoothing formula. Longuet-Higgins and Cokelet (1976) proposes a smoothing and regridding-scheme suited for the calculations.

This method will describe fully nonlinear potential flow waves, since no assumptions have been made regarding the height of the waves. No restrictions have been made regarding the nature of the velocity potential. If increased accuracy is needed, then the time marching must be done more accurately.

For validation of the method, the reader is referred to Marino (2011).

In both Marino (2011), Marino et al. (2011) and Marino et al. (2013), this method is connected to linear irregular sea, so a simulation with irregular fully nonlinear waves are obtained.

7 | FAST

To investigate the problem of higher order wave loads on a bottom fixed turbine, a solver named FAST is used. FAST is a fully Aero-Hydro-Servo-Elastic solver, developed by National Renewable Energy Laboratory (NREL). It was among the first solvers capable to perform a fully coupled analysis on floating offshore wind turbines.

The main purpose of the solver was to develop a tool so floating wind turbines could be analysed, but it can also be used to analyse bottom fixed turbines. Most of the solver's capabilities for offshore wind turbines was developed as part of the Ph.D thesis of J. Jonkman (Jonkman, 2007).

FAST has been chosen to investigate the problem because it is free and has an open source code, making it possible to alter the calculations in order to better account for higher order wave loads. Another reason for choosing FAST, is that there already exists an input-model of the reference wind turbine described in chapter 2, which was used in OC3.

Parts of this chapter is a summary of my project thesis, but is included for completeness.

7.1 Short Summary of Capabilities

In order to provide some information on the workings of FAST, a short introduction to its calculation model is needed. Since FAST is a coupled aero-hydro-servo-elastic solver, it is natural to mention some of the aspects regarding each of the elements.

To calculate the aerodynamic forces on a blade, each blade is divided into a number of sections and each section is assumed aerodynamically independent from the others. The property of each section is given through an input file, and it is possible to use the coefficients statically, or with a dynamic stall model. For the wake of the turbine the user can choose between a classical blade element momentum theory, or a generalised dynamic wake model. The theory of the aerodynamic calculations is found in Moriarty and Hansen (2004).

FAST has the possibility of performing calculations on either a floating wind turbine, or a bottom fixed one. The theory behind the calculation of hydrodynamic forces will vary depending on which type of turbine one is studying. For the case of a floating turbine, FAST calculates the linear diffraction and radiation forces, in the time domain. Jonkman (2007) presents the calculations and rationale behind them in depth. For a bottom fixed turbine, the wave forces are as mentioned calculated by using Morison's equation in the relative form covered in appendix A.1.

Incident waves are limited to the case of linear waves, either regular or irregular. Three stretching techniques are possible; vertical, extrapolation or wheeler stretching. FAST has also the possibility of introducing externally calculated waves. This possibility will be used in this thesis for using fully nonlinear incident waves.

For a wind turbine it is necessary to be able to control the pitch and revolution of the blades. This is done partially to maximise power generation on off-design conditions and to be able to maintain control over the rotor in the event of strong winds. In FAST, the control system can mainly be implemented as a coupling with Matlab-Simulink, or as a dynamically linked library.

For the structure, FAST uses a modal approach. For the case of the tower, it has two modeshapes in the front-aft direction, two in the side-side direction, and one torsional mode. For the blades there are two modes in the flapwise direction, and one mode in the edgewise direction. According to Langen and Sigbjørnsson (2011) most vibration problems are governed by the lowest modeshapes and their natural frequency. So including two modes will probably give an accurate enough representation, given the tower deflection is reasonably small.

7.2 Implementing the Changes in FAST

The process of implementing the extended features in FAST has been quite comprehensive. It involves the calculation of the spacial derivatives for the existing linear waves and also the wave slope. This is needed because Rainey's expressions needs these quantities. The Fenton generated waves are implemented as an entirely new feature in FAST, which meant that some additions were made to the wave initialisation part in FAST. The fully nonlinear waves are read by FAST in an already existing feature where an external calculated wave can be used. Only slight modifications was needed to make this work.

These implementations are thoroughly described in appendix C. In the appendix also how the solver calculates the force on the structure is covered, along with an introduction to a small error in the linear incident waves which may cause disturbances in the force. It has not been possible to include the source code for the changes in the appendix, but in the digital appendix to this thesis, the source code is present, along with a pre-compiled version which runs on a 64-bit Linux machine.

The summary of the force implementation is that the force has been implemented as presented in section 5.6 equation 5.2. The second line in the equation will be zero for all circular cylinders with no yaw motion, and has not been implemented. The $\boldsymbol{l}$ and $\boldsymbol{t}$ vectors have been implemented so the structure remains vertical for all time instance. This is a simplification, but it is in line with the assumption FAST is working under, with small deflections of the tower. It should be noted that even though the forces are calculated with kinematics at $x = 0$, the actual velocity of the element is used to calculate the relative velocities needed. More details can be found in appendix C.

8 | Verification of Implementations

8.1 Verification of Recompilation

FAST is originally developed for a Windows environment, but by following a forum post made from a member of the community [1] , I was able to recompile FAST for use on a 64-bit Linux operating system. The new version has been recompiled using gfortran, an open source compiler. The recompiled version runs significantly slower than the provided .exe file, probably due to not being able to optimise as much as the commercial compiler used at NREL.

To verify that this process which involves some minor patches does not introduce any errors, it is useful to compare two equal simulation, one on Linux and one on Windows.

The main component which contains uncertainty is how the control system is behaving after the port to Linux. Figure 8.1 shows the velocity of the rotor subjected to the same wind input, for the case of simulations ran with the original executable, and the case of recompilation.

As can be seen, the two show good comparison, but there seems to be a slight phase difference. This is also seen in the incident waves, so it appears that a small but constant phase difference is introduced. The reason for this phase difference might be as simple as the use of different random numbers in the phase of the incident waves. Since more variables are declared, the random number generation in FAST, should give different results. This means that the time series of the force is not identical, and so the results should not be totally identical. To conculde:

---

[1] https://wind.nrel.gov/forum/wind/viewtopic.php?f=4&t=588

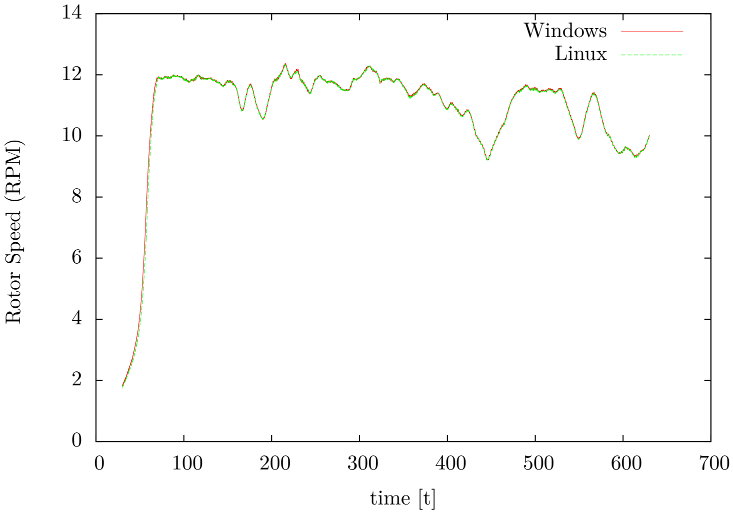

Figure 8.1: Comparison of the rotor speed for a Windows run, and a Linux run.

although some phase difference exists, it seems that the recompilation has not introduced any errors in the control system.

8.2 Verification of Fenton Generated Waves

To validate the load model implementation, nonlinear regular waves are needed. In chapter 6 it was decided to implement Fenton generated waves. The implementation of these should also be verified so that confidence can be put on results obtained with these waves.

Since the wave elevation is calculated as a sum of components, a Fenton generated wave with only one component should give approximately a linear wave. This means that it is possible to compare the already existing feature of linear waves and Morison's equation, with the new feature of Fenton waves with Morison's equation. If the two yield the same results, for the case when Fenton is generated with one component, this is an indication that the Fenton waves are implemented correctly.

Two series of calculations have been made on the reference turbine. The wave amplitude has been set to 2 [m] and the wave period to 12.4 [s]. Aerodynamic

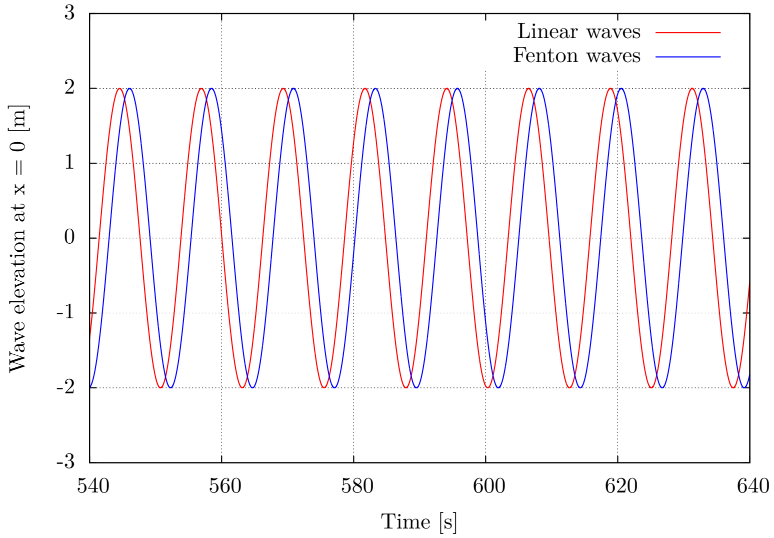

Figure 8.2: Comparison between the wave elevation for generated by linear theory, and Fenton theory.

calculations have been turned off, so the only external force acting on the turbine are the waves. In one of the series the existing linear waves have been used, and in the other the Fenton generated waves have been used. As a first comparison, it is beneficial to compare the wave elevation between the two.

Figure 8.2 shows the time realisation of free surface elevation. As can be seen, the two have the same amplitude, but slightly different phase. The different phase has no significance as long as the phase difference is constant, which it appears to be.

Figure 8.3 shows the total force on the structure from the two different wave models, and the two shows very good agreement. The phase difference is naturally caused by the phase difference in the wave elevation.

Figure 8.4 shows the bending moment at the mudline, from the incident waves and again the results are similar.

There seems to be some small disturbances in the bending moment at the top of each cycle for the linear case, which is believed to be caused by numerical errors. These errors are presented in detail in appendix C.1.5. Apart from that, all figures shows excellent comparison, leading to the conclusion that the implementation

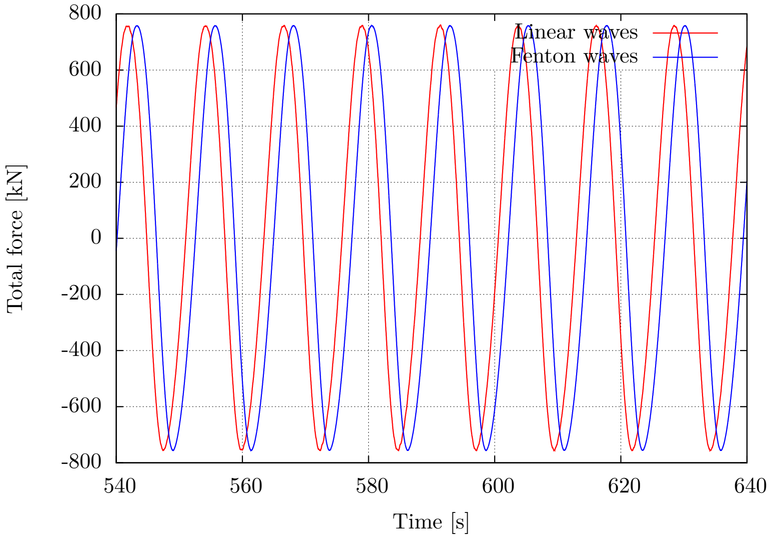

Figure 8.3: Comparison between total force from incident waves generated by linear theory, and Fenton theory.

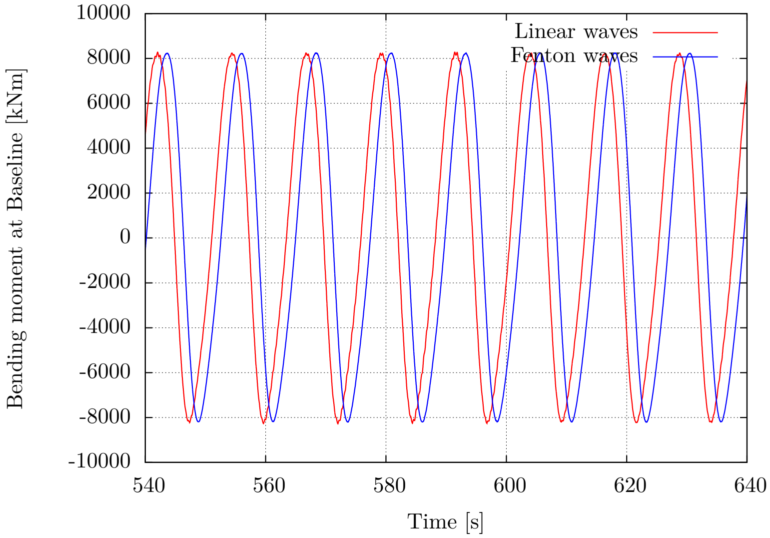

Figure 8.4: Comparison between bending moment at mudline from incident waves generated by linear theory, and Fenton theory.

of Fenton generated waves in FAST is correct.

8.3 Verification of Load Model Implementation

In Chaplin et al. (1997) a series of experiments were conducted to compare the slender body loads with experiments. The experiments were performed with a frequency focusing technique that created steep, near breaking waves. A cylinder was mounted, so that the waves interacted with it. Description of set-up and characteristics of the cylinder can be found in the original paper. Seven different waves was sent towards the cylinder, which was given the identities “745, 750, 755, 760, 765, 770, 775”.

To obtain the wave kinematics from the recorded free surface elevations, they used two different models in the paper; a crest fitting technique, and a regular wave based on stream theory. To try to recreate the latter case the Fenton generated waves from section 6.1 is used with FAST.

These waves will not be able to recreate the exact free surface elevation of the focused waves, because the focused waves are highly nonlinear and will be unsteady. The Fenton generated waves are a steady solution to the wave propagation problem, and is a regular wave. It is thus not expected to fully recreate the experiment and obtain good comparison with the results reported in the paper. The real purpose of using the Fenton waves is however to compare with the results obtained by Stream theory in the paper. Since Fenton waves and Stream function waves stems from the same theory, the results obtained with Fenton should be comparable to the reported results with stream theory. If these two are similar, then it can be argued that the load model has been implemented correctly in FAST.

To compare the experimental realised waves, and the numerically Fenton generated, two plots that compares two cases has been made. The data from the experiment has been read from Chaplin et al. (1997, figure 1), and is thus prone to small errors. By comparing the smallest and the largest waves in the experiment with the numerical waves, it is possible to get an indication of how accurate the representation is.

It is clear from figure 8.5 that the crest of the lowest wave is represented satisfactory by a Fenton wave, but that the trough is not as good represented. For the largest case it is clear that the wave in the experiment contains strong asymmetry in the vertical plane. The Fenton wave is not able to reproduce this asymmetry and as can be seen in figure 8.6, it does not give as good a fit as for the lowest wave. Since the wave in the experiment is unsteady and the Fenton wave is

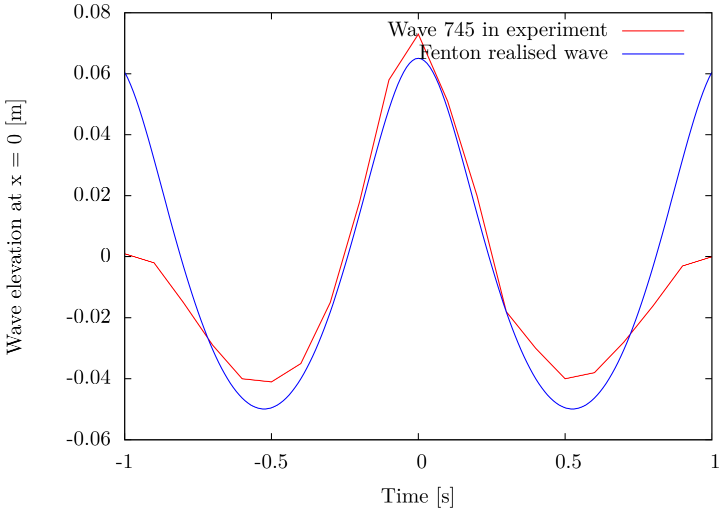

Figure 8.5: Comparison between wave 745 in experiment and Fenton generated wave.

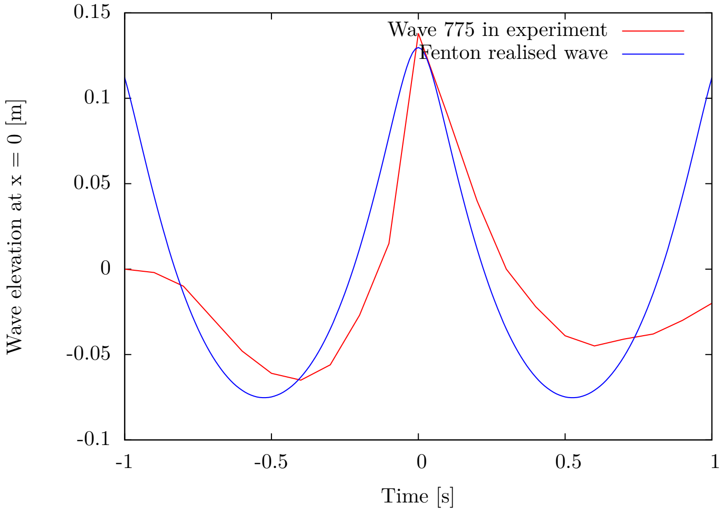

Figure 8.6: Comparison between wave 775 in experiment and Fenton generated wave.

steady, it is only natural that the error towards ±1 is large where the Fenton wave goes towards another crest. One would expect the error in the force calculation of the smallest wave to be quite small, but that the error will increase with increasing wave height. Is is expected that based on Fenton waves, the forces on the cylinder will be significantly underpredicted at the largest waves.

FAST is a wind turbine design tool, and needs all the components of a wind turbine in order to work. A small version of a wind turbine has been created, so that it has the same diameter and depth as the cylinder in the test. On top of this a small rotor has been placed, which is more or less a scaled down version of the rotor on the reference turbine. Since only the forces from waves are is interesting in this context, the rotor was parked, and all aerodynamic calculations where turned off. In the experiments the natural frequency of the cylinder/turbine-tower was approximately 28 $[Hz]$. At first the small tower was made with this natural frequency, but this lead to the need of extremely small time steps, so the cylinder was made entirely stiff with no degree of freedom.

The waves were generated in a way that made it possible to send only one wave crest to the tower. To get as similar conditions as possible, by trial and error a time interval that made the wave elevation start with a trough was found for each case. Figure 8.7 shows the realised time series for the different cases. The waves will have slightly different propagation velocity, so the time has been shifted for each case so that the top of the crest is at approximately $t = 0$. This is done only for the purpose of comparison.

With the realised time series, calculations have been performed for each case. The maximum moment has been extracted and made non-dimensional by the following relation used in the original paper:

$$M'_{max} = \frac{M_{max}k}{\rho g \pi r^2 h} \tag{8.1}$$

For all the cases, a series of calculations have been made with different components of the slender body expressions. This has been done both to verify that each component has been implemented correctly, but also to compare the different components to the experiments. In figure 8.8 the following definitions has been used: M-Morison inertiea force (with acceleration including convective accelerations), A-Axial divergence force, I-Free surface intersection force, V-Viscous force with $C_D = 1$.

As can be seen from figure 8.8 there is reasonably good agreement with potential forces and the experiments for the smallest waves. With the inclusion of the viscous force, there is indeed very good agreement with the experiments up to

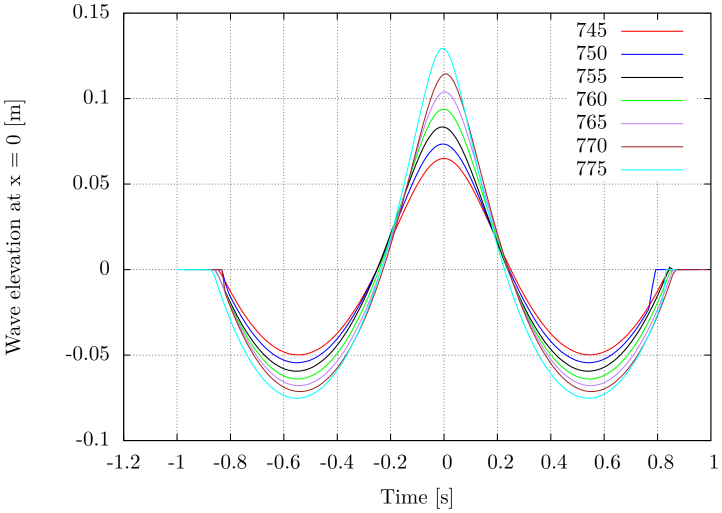

Figure 8.7: Realised Fenton time series for the 7 different cases.

the two steepest waves. With the viscous drag force included the maximum moment of the smallest waves are overpredicted.

The two largest waves contain a significant asymmetry with respect to the vertical axis, and must be considered more nonlinear than the realised Fenton waves. This means that if the exact wave had been recreated the results might have been closer to the experimental results.

As can be seen from figure 8.8, there seems to be a significant difference between results only containing mass the Morison inertia force, and the results also including axial divergence force. The free surface intersection does not have much influence, except for the steepest waves.

Excellent comparison is found between the implemented model in FAST with Fenton generated waves, and the results calculated in Chaplin et al. (1997) with Stream theory. The good agreement between the results is a strong indicator that the load model has been implemented correctly in FAST.

In the paper, they report of a secondary load cycle, appearing shortly after the main load peak. In their numerical calculations they did not succeed in reproducing this load cycle. Neither in the calculations performed here has this load cycle been seen.

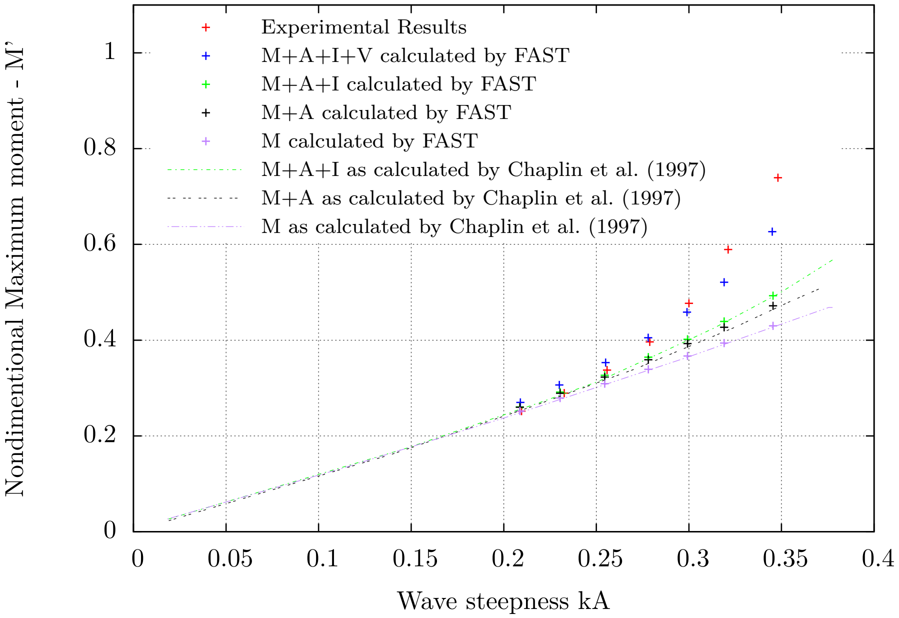

Figure 8.8: Nondimensional maximum moment from calculations, compared with experiment. M-Morison inertia force(with acceleration including convective terms), A-Axial divergence force, I-Free surface intersection force, V-Viscous force with $C_D = 1$.

9 | Validation and Comparison of Load models

9.1 Introduction

Huseby and Grue (2000) have performed a series of experiments to investigate the higher harmonic load components in regular waves. A cylinder has been placed in a field of incident regular waves, and the force it is subjected to has been measured. The force has been analysed by taking the Fourier transform of the signal, meaning that the force F, is decomposed into it's harmonics.

$$F = \mathrm{Re}\{F_1 e^{i\omega t} + F_2 e^{i2\omega t} + F_3 e^{i3\omega t} + F_4 e^{i4\omega t} + F_5 e^{i5\omega t} + ...\} \qquad (9.1)$$

Where ω is the incident wave frequency.

The paper presents results for the first seven harmonics, for two cylinders with radius $r = 0.03[m]$ & $r = 0.04[m]$, and for a range of kA and kr values. The natural frequency of the cylinders in the experiment was around $25[Hz]$. For the characteristics of the experimental set-up, the reader is referred to the paper.

The experimental waves are in the paper said to be close to Stokes waves, generated by a pure sinusoidal signal to a wave maker. According to the paper these experimental waves are prone to be disturbed by parasitic waves. They make an argument how the measurements have been performed in order to avoid that these waves disturb the experiment. In the parts of the time series that are free from parasitic waves, the free surface elevation is regarded as being close to a pure Stokes wave, and given by:

$$\zeta = A\cos(kx - \omega t) + a_l^{(2)} cos(2(kx - \omega t)) + a_l^{(3)} cos(3(kx - \omega t)) + ... \tag{9.2}$$

This indicates that it is possible to describe fluid domain by the analytic velocity potential:

$$\phi = Re[\frac{Ag}{i\omega} e^{kz} e^{i(kx-\omega t)}] + O(A^4) \tag{9.3}$$

The dispersion relationship must be written as: $\omega^2 = gk(1 + A^2k^2)$.

This means that the incident wave kinematics ideally have only a single oscillation frequency, so all higher harmonic forces are due to the wave-structure interaction.

Regarding the simulations with FAST, as for the case in section 8.3, a small version of the reference turbine has been created in order to be able use FAST. The simulations performed to compare the numerical model with the experiments can be divided in two: Firstly a model with a completely stiff tower has been placed in waves generated by linear theory. Wheeler stretching has been used to obtain kinematics to the instantaneous free surface. Secondly a model with flexible tower and Fenton generated incident waves was used.

The reason for a completely stiff cylinder in the linear wave case is that because of the inherent error in the wave generation in FAST, mentioned in appendix C.1.5, the elements must be very small. The smallest wave height in the experiment is $\approx 4[mm]$, meaning that the elements should ideally be much smaller than this. With a water depth of $0.6[m]$ this leads to the need for a large number of element, making it practically impossible to satisfy this with the chosen wind turbine. Also if this cylinder should be free to flex with two bending modes, the time step would be extremely small. A guide for the time step needed for FAST is $dt < \frac{1}{10 * f_n}$ where f_n is the highest natural frequency in [Hz].

Since there is a need for both small time step, and many structural elements, it was concluded to perform calculations on a completely stiff model. This will lead to inaccuracies, but since the first bending mode natural frequency is $25[Hz]$ in the experiments, very small dynamic effects are expected. Even with this stiff tower, it is difficult to use enough elements and still have a reasonable calculation time. The results with linear waves seems to contain a number of higher order disturbances, making the results a bit uncertain.

The calculations with linear incident waves has been performed with a viscous drag coefficient set to zero. This is because a comparison can be made between the only the inertia term in Morison's equation and Rainey's expressions without disturbances from the higher order viscous drag term. No calculations have been made with viscous drag, because it is intended to compare with the analytical expression presented in section 5.7, which has been made without viscous drag.

The second analysis with Fenton generated waves has been performed with a flexible tower with a natural frequency of the first bending mode $\approx 26[Hz]$. To get conditions as close to the experiment as possible, only the tower bending modes are free to move, and all other DOFs has been turned off. Both Rainey's slender body expressions and Morison's equation have been used. In both cases the drag coefficient has been varied, so one set was ran with $C_D = 0$ and another with $C_D = 1.0$. In all cases the added mass coefficient has been set as $C_A = 1$.

Calculations have not been performed with the exact same kA values as in the paper, but spread evenly out over the range $kA = 0.02 - 0.2$. This is done because the exact kA values of the waves used in the experiment have not been reported. This makes it impossible to compare the time evolution of the free surface elevation between the experiments and the numerical simulations.

Regarding the results, the amplitude of the n^{th} harmonic has been made nondimensional by dividing on $\rho g A^n r^{(3-n)}$. Where A is the incident wave amplitude, r the cylinder diameter, ρ the water density and g the gravitational constant.

The time series used, are long enough to dampen out any eventual numerical transients in the start up phase, and the data used has been gathered from the tail of the time series to properly ensure steady state conditions.

A quick note on the legend of the plots. All results with forces by Morison is represented with triangular marks/lines with triangles on, and all plots with forces by Rainey is represented by crosses. A choice has been made regarding the colors, so that each case studied has it's own color. This makes it easy to compare results by Rainey and Morrison, as it only reduces to comparing the data of the same color.

9.2 Postprocessing

In the paper, time series consisting of 10 waves were used as a basis for the Fourier transform to decompose the force into it's harmonics. To ensure comparable results, a routine has been made which selects exactly 10 cycles from the time history of the force in the simulations performed. The Fourier transform is then calculated using the build-in Matlab function FFT based on these cropped time series. To find the correct amplitude of the various harmonics, the following

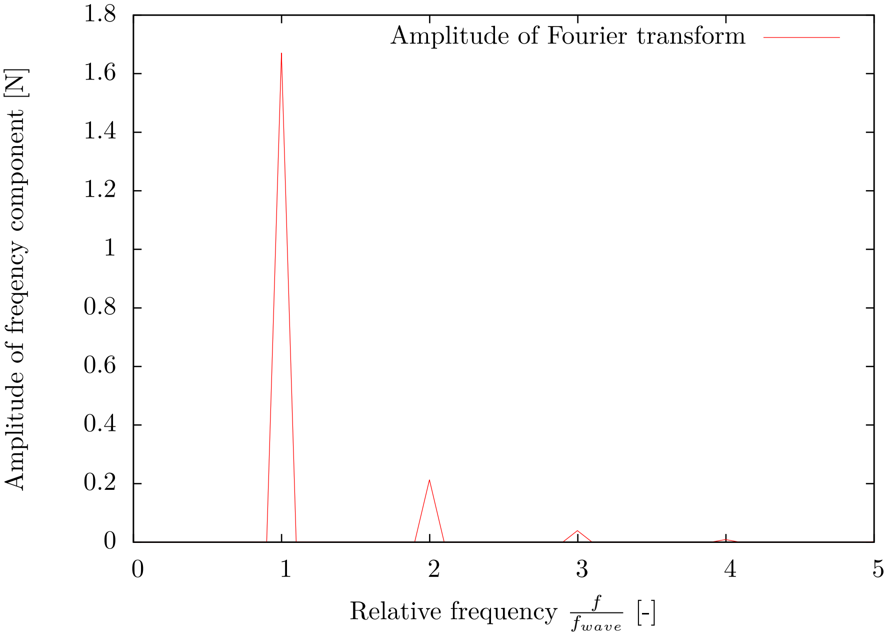

Figure 9.1: Example of the Fourier transform of the force on the monopile. Here shown for a wave with frequency 1.3 [Hz] and amplitude 0.029412 [m], Fenton generated incident waves.

relation has been used to scale the output of the FFT:

$$F_n = \frac{2}{N}|\mathcal{F}(f_n)| \tag{9.4}$$

Where F_n is the n'th harmonic force, N is the number of elements in the time series, $\mathcal{F}(f)$ is the value of the Fourier transformation at the frequency f, and f_n is the frequency of the n'th harmonic of the wave frequency.

To automate the process, and also take into account that there might be small discrepancies between the frequency with the local maximum in the $|\mathcal{F}(f_n)|$ and f_n, the maximum value has been chosen in a small interval around f_n

A plot of of the amplitude in the frequency spectrum for one of the cases is shown in figure 9.1. The amplitude is calculated as given in equation 9.4.

As can be seen from figure 9.1 the force clearly contains higher harmonics of the wave frequency. From the calculations, up to the 4th frequency can be observed for this case where a Fenton generated wave has been used. For waves with smaller amplitudes, the 4th harmonic is not always observable. As the fourth harmonic only appears for the biggest waves, it has been decided to only compare the first three harmonic loads. In the figure the incident wave is Fenton generated, and it is really clear that the time series only contain forces at the harmonics of the incident wave frequency, which strengthens the belief that this wave model is properly implemented into FAST.

Figure 9.1 also stands as a characteristic distribution of the force. From all the calculations it appears that the first harmonic load is dominating, and the second harmonic load is again larger than the third and so on.

9.3 Linear incident waves

For the case of linear incident waves, the first three components of the force are presented in figs. 9.2 to 9.4. Here both experimental data, numerical data with Morison's loading, numerical data with Rainey's loading and the analytical expressions for the load by Rainey are presented. A deliberate choice has been made to not include the analytical expressions for the load by Morison, since this would make the figures more difficult to read. The drag coefficient has been set to zero in order to be able to compare the potential part of the two load formulations.

It is observable that the first order component seems to be slightly underpredicted by both load models. There does not seem to be any significant difference between the two, but Rainey's expressions seems to predict slightly larger values as kA increases. This is to be expected by the expressions presented in section 5.7, where it is clear that Rainey's expressions gives additional contributions to the first harmonic load. It is clear that the analytically derived load of Rainey's force is similar to the numerically calculated by FAST.

For the second harmonic load there is quite good comparison with experiments. For all kA values Rainey's expression predicts the highest values, as is expected in section 5.7. Also here, is it good agreement between the analytically calculated results and the numerical calculated results. Small differences are present at the lower kA values, but this is believed to be caused by numerical errors due to small amplitude of the load, and the error (app. C.1.5) in the linear incident waves, that generates noise in a Fourier transform.

For the third harmonic there seems to be generally bad agreement with experimental results. This is true for both experimental results and the analytically

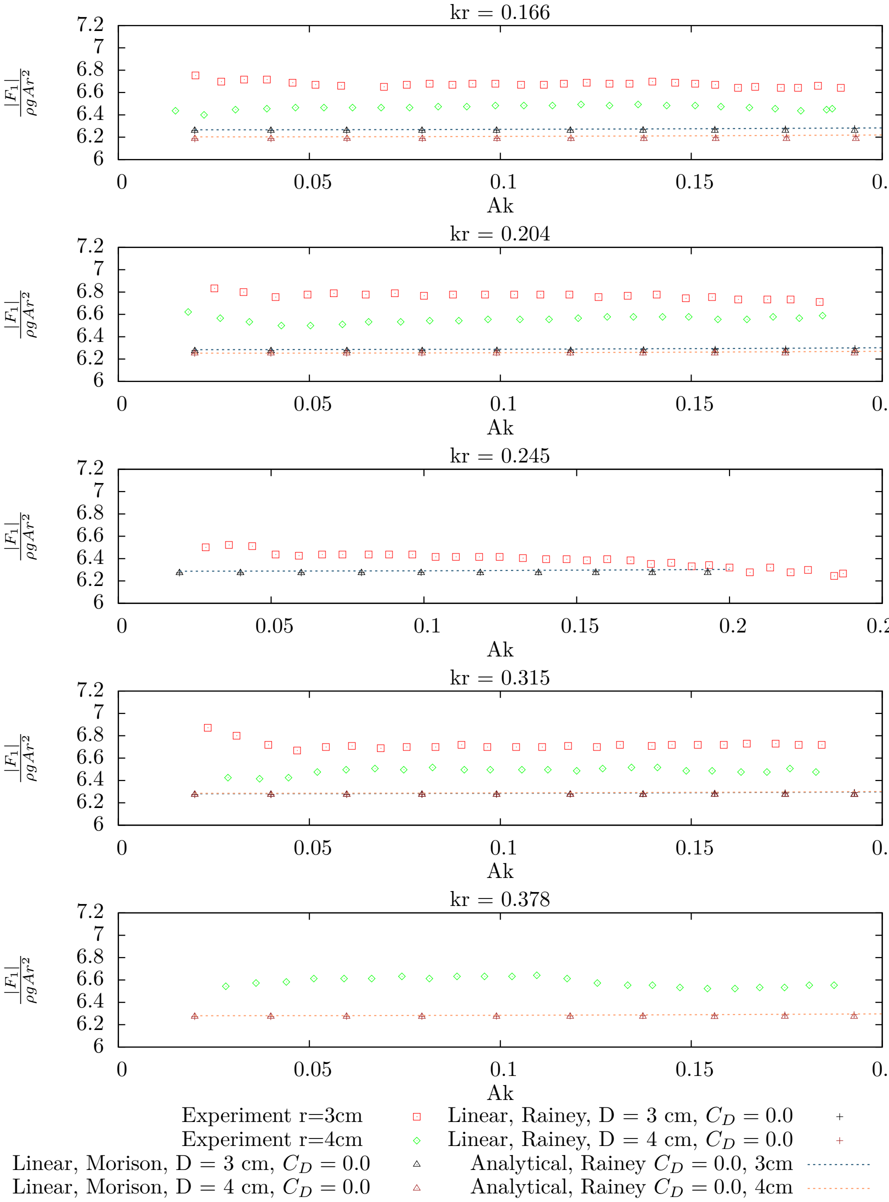

Figure 9.2: First harmonic component of wave force, for various kr values. Linear + wheeler incident waves, and forces by both Morison and Rainey. No viscous drag

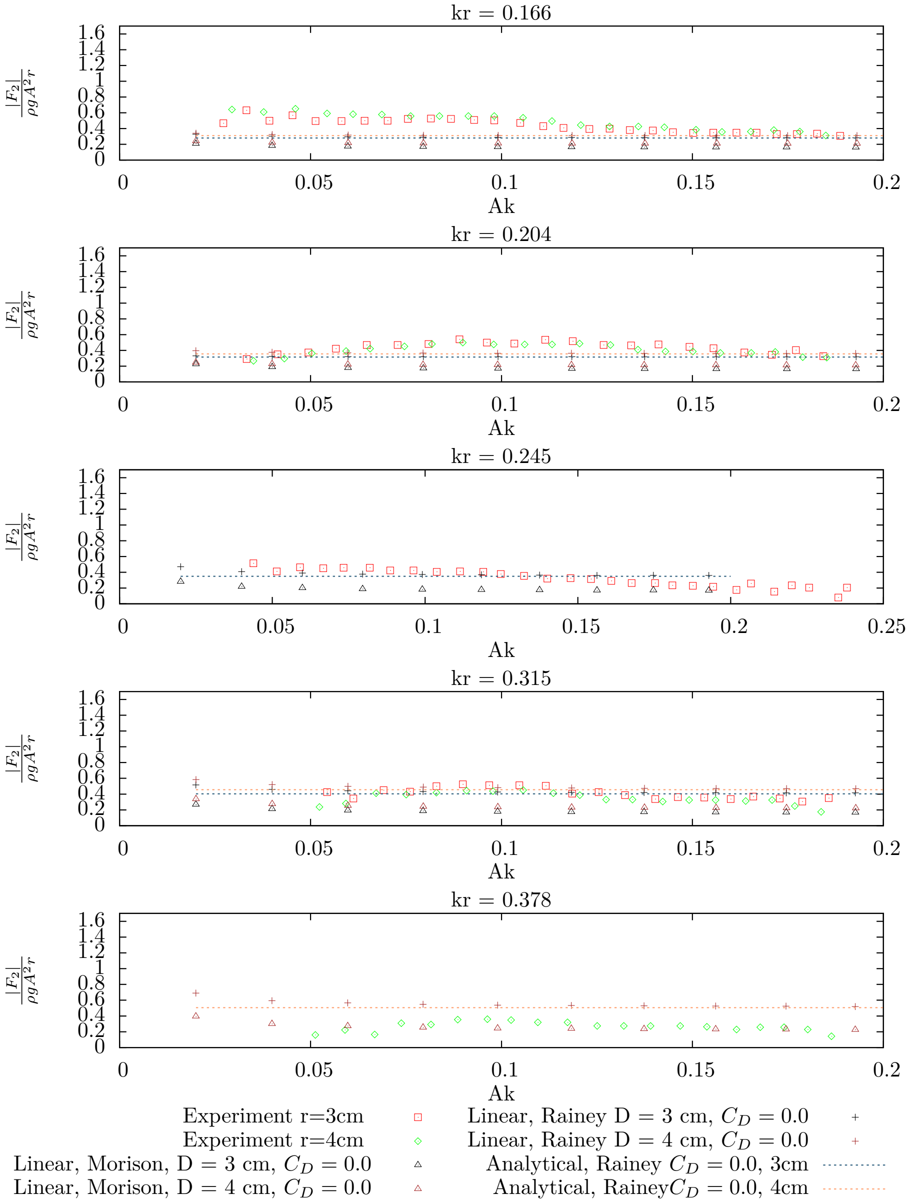

Figure 9.3: Second harmonic component of wave force, for various kr values. Linear + wheeler incident waves, and forces by both Morison and Rainey. No viscous drag.

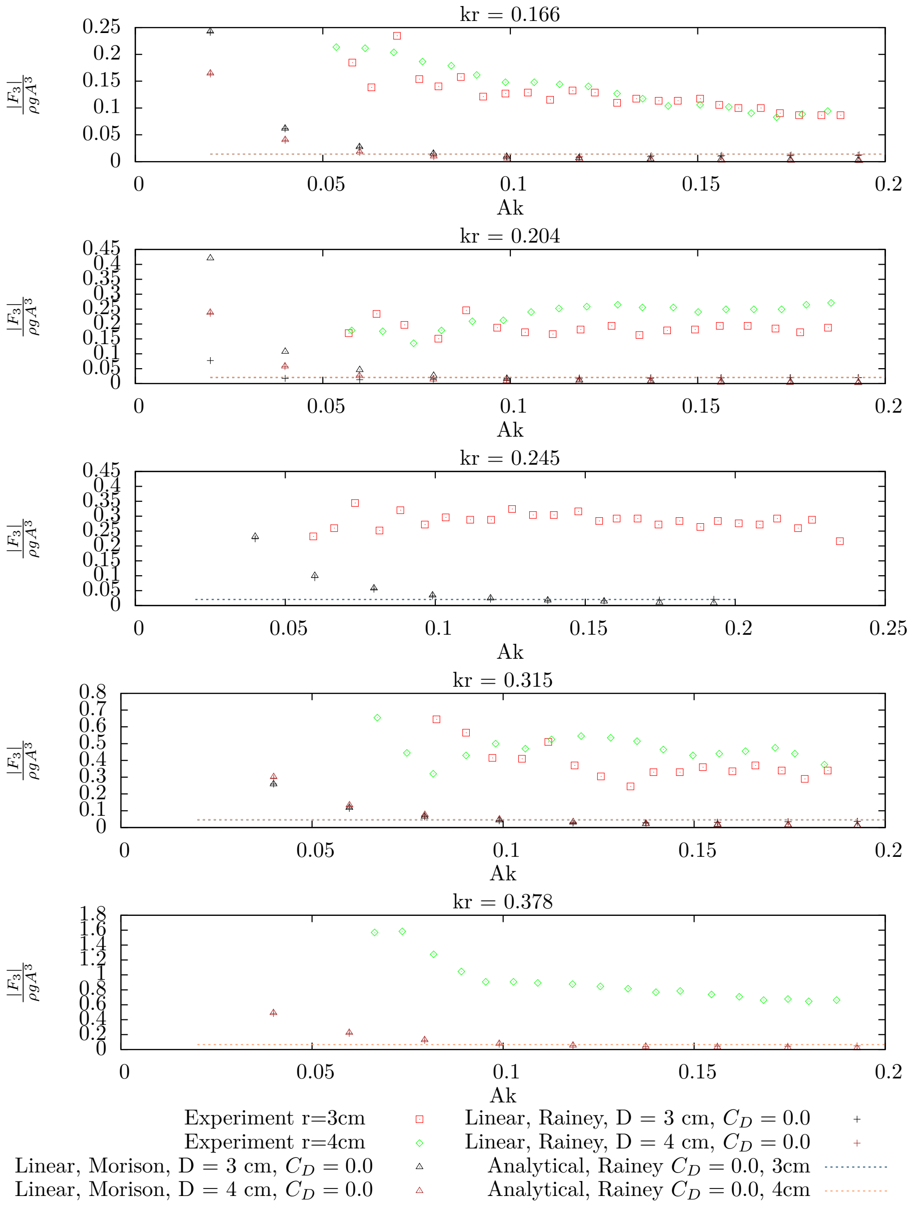

Figure 9.4: Third harmonic component of wave force, for various kr values. Linear + wheeler incident waves, and forces by both Morison and Rainey. No viscous drag.

calculated values. There is however good agreement between analytical and numerical values for the higher range of kA values, which indicates that the calculations have been implemented correctly. Again the error in the lower range is expected to be due to numerical errors and noise.

The cause of the large discrepancies of the third harmonic load can be threefold. Either the load predicted is too small, the linear incident waves can not accurately represent the waves in the experiment or the fact that the viscous drag has been left out. The cause is probably a mix of the three cases, as the waves in the experiment is said to be close to pure Stokes' waves which have a free surface elevation given as in equation 9.2. From the expression for the third harmonic load is can be concluded that the free surface is important for this load, and by not having the same free surface elevation as the experiment, the linear waves will introduce errors here. Secondly, FNV predicts a third harmonic load which is eight times larger than Rainey's expressions. The difference between them might be a source for the bad agreement for the third harmonic. There has been suggestions to include a surface distortion force in Rainey's slender body expressions to take into account the difference between the two. However Chaplin et al. (1997) finds better agreement in steep waves, when this is not included, so it has not been included in the calculations in FAST. Lastly the viscous drag load give loads at odd frequencies, so for the third harmonic there should be an additional component.

9.4 Fenton generated incident waves

It is believed that the Fenton generated waves will more accurately represent the free surface elevation in the experiments than the linear waves. The Fenton generated waves will however contain higher harmonics in the description of the fluid domain, since the solution is given as a sum of Fourier components. In the paper they have stated that in the field there should ideally be only one frequency. The difference between the experiments and Fenton waves will be discussed in section 9.6.

For the Fenton generated incident waves, the main purpose is to compare the two load models with experimental data. Therefore first a comparison between forces calculated with Morison's equation are presented in figs. 9.5 to 9.7. Figures 9.8 to 9.10 presents the comparison for Rainey's case. In both cases calculations with and without viscous drag force have been included.

Lastly three figures showing direct comparisons between Rainey and Morison are presented in figs. 9.11 to 9.13. Again calculations with and without drag are included.

By comparing the figures it appears that the two models predict quite similar results for the first harmonic load, and also for the second harmonic load. Rainey's expressions predict slightly higher values for the second harmonic load, but they are both overpredicting the experimental results. The overprediction increase with increasing kr values. Rainey's predictions fit the third harmonic experimental data better than the predictions made by Morison's equation.

Since the waves are nonlinear, Morison's equation will also contain higher harmonic components than the second harmonic that comes from integrating to a moving free surface. This makes it possible to investigate how much of the higher harmonic loads that stems from the nonlinearities in the waves, and how much of the higher harmonics that originates in the load formulation. This will be explored in section 9.6

In figs. 9.11 to 9.13 the results of the two load models are compared. The first harmonic is very similar for the two, but with higher kA values Rainey predicts slightly larger loads. The first harmonic load is underpredicted by both models for all values of kA and kr. Rainey's model predicts higher second harmonic load for all values, and the difference between the two increases with increasing kr value. Compared to the experiments, both models overpredict this load. Also for the third harmonic load Rainey predicts higher loads. When compared to the experiments Rainey's expressions shows better comparison than Morison's equation for this harmonic.

The difference between the two load models seems to be significant for the second and third harmonic. This is an indication that the extra nonlinear terms in Rainey's expression compared to Morison's equation has some importance for the total load, also in nonlinear incident waves.

The results from these analyses will be further discussed in section 9.6

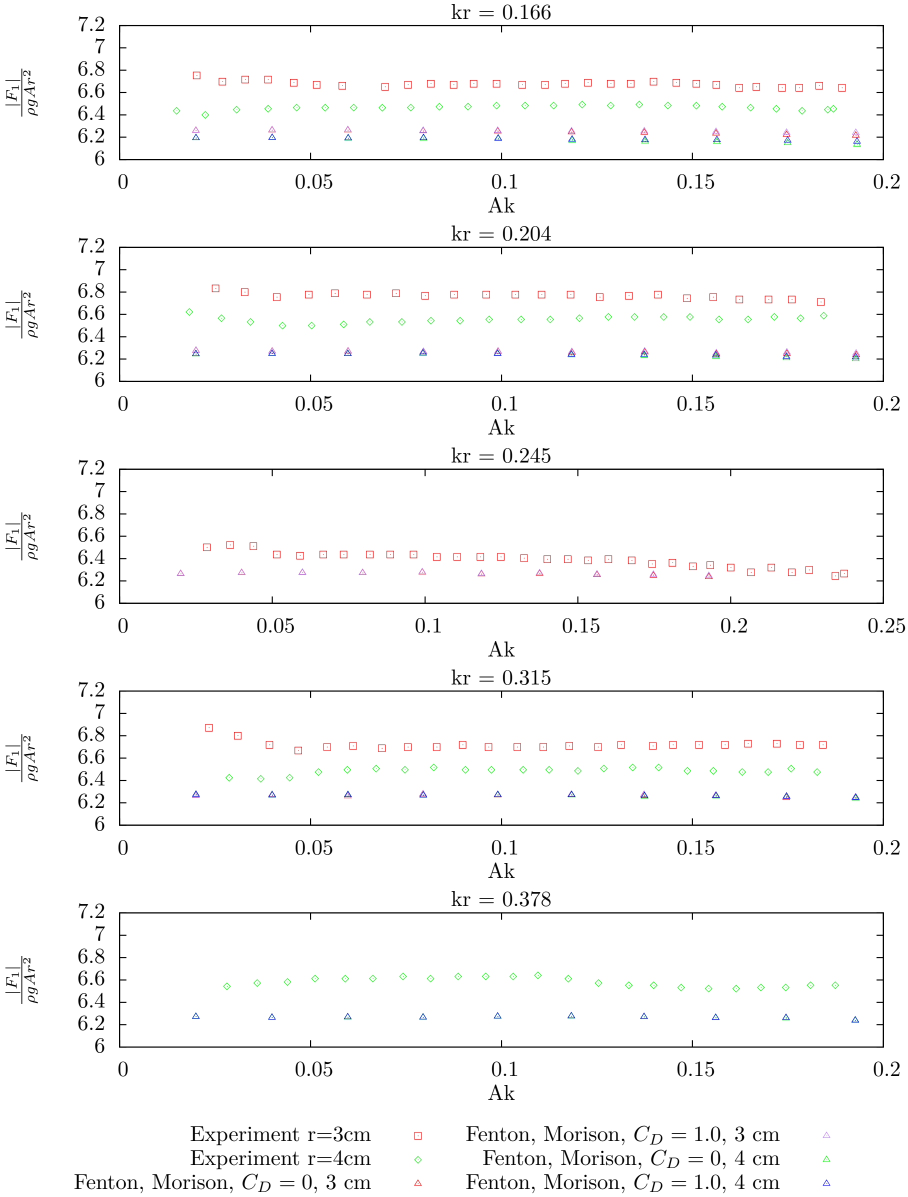

Figure 9.5: First harmonic component of wave force, for various *kr* values. Fenton generated incident waves, and forces by Morison's equation, with and without drag.

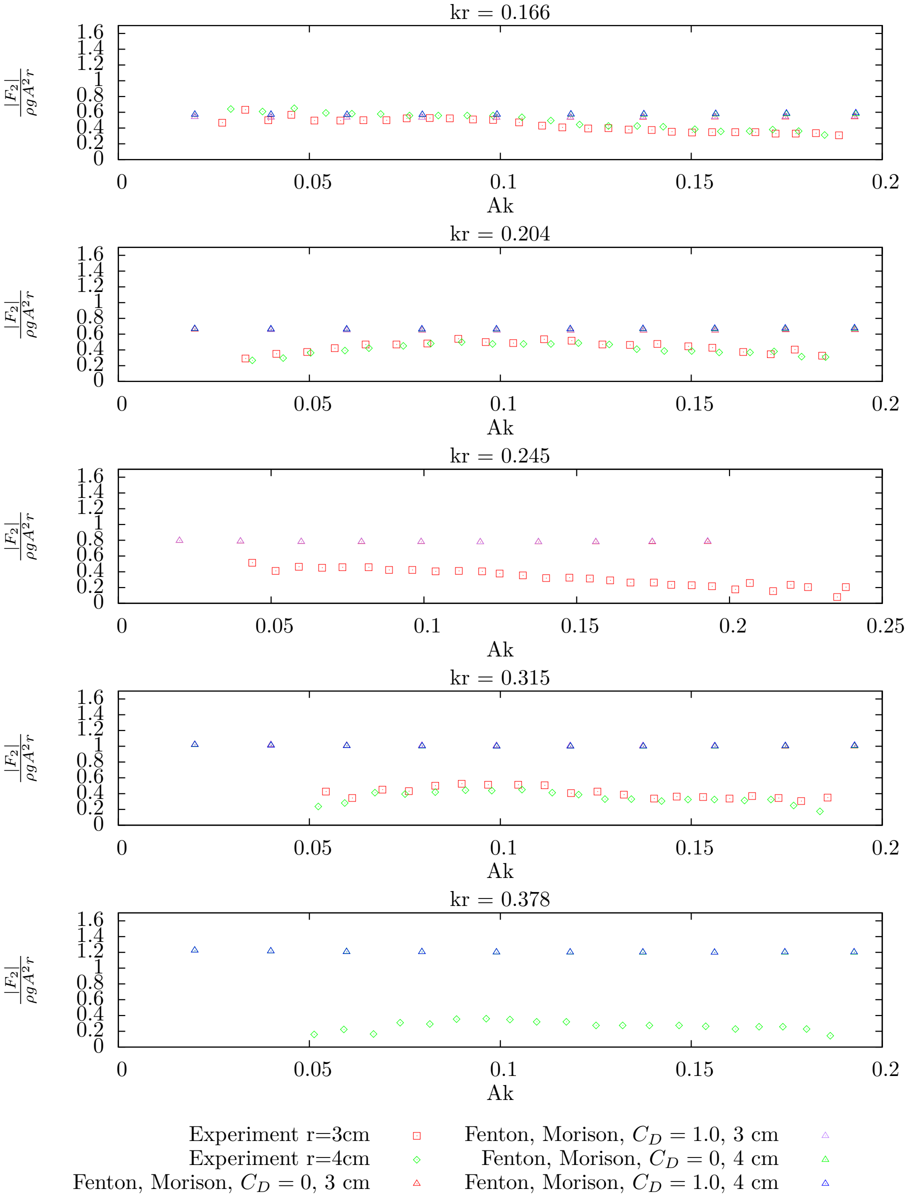

Figure 9.6: Second harmonic component of wave force, for various kr values. Fenton generated incident waves, and forces by Morison's equation, with and without drag.

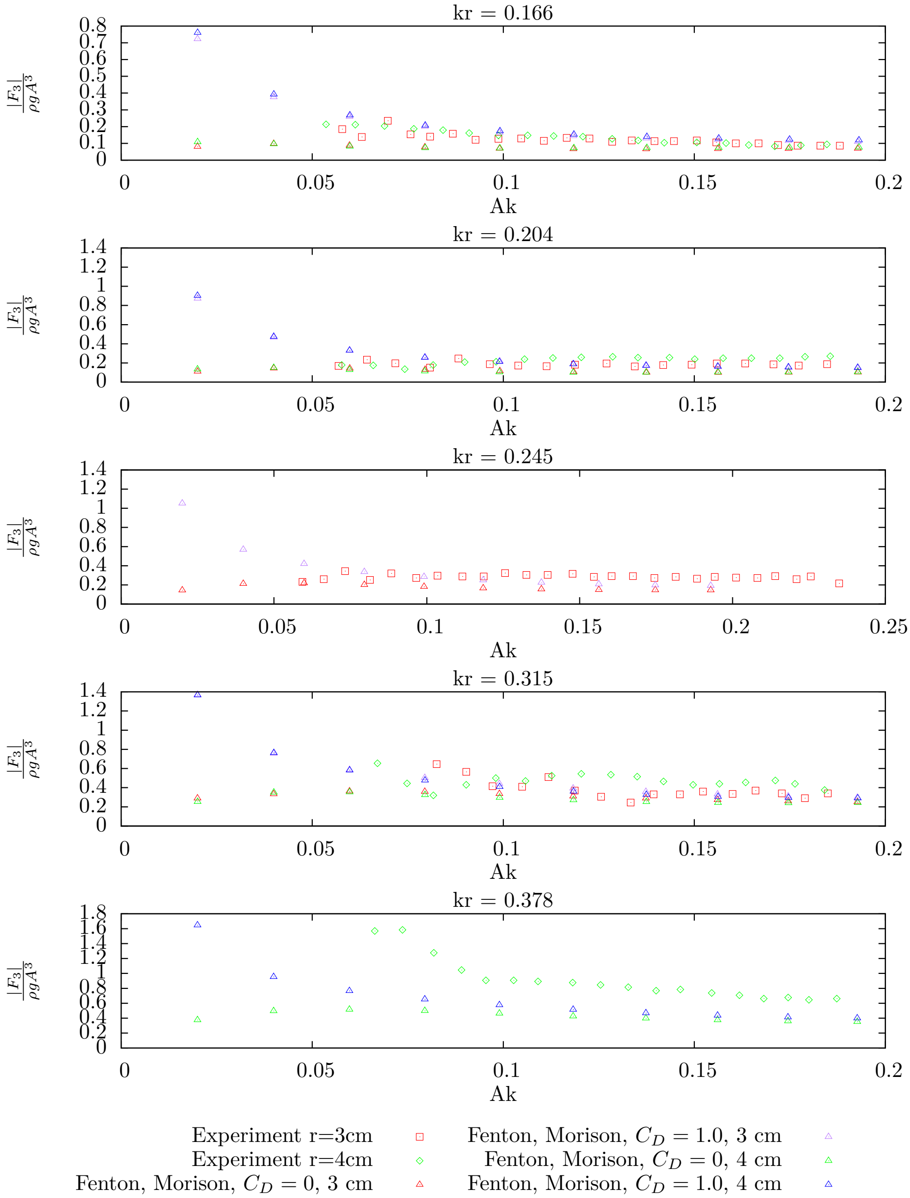

Figure 9.7: Third harmonic component of wave force, for various kr values. Fenton generated incident waves, and forces by Morison's equation, with and without drag.

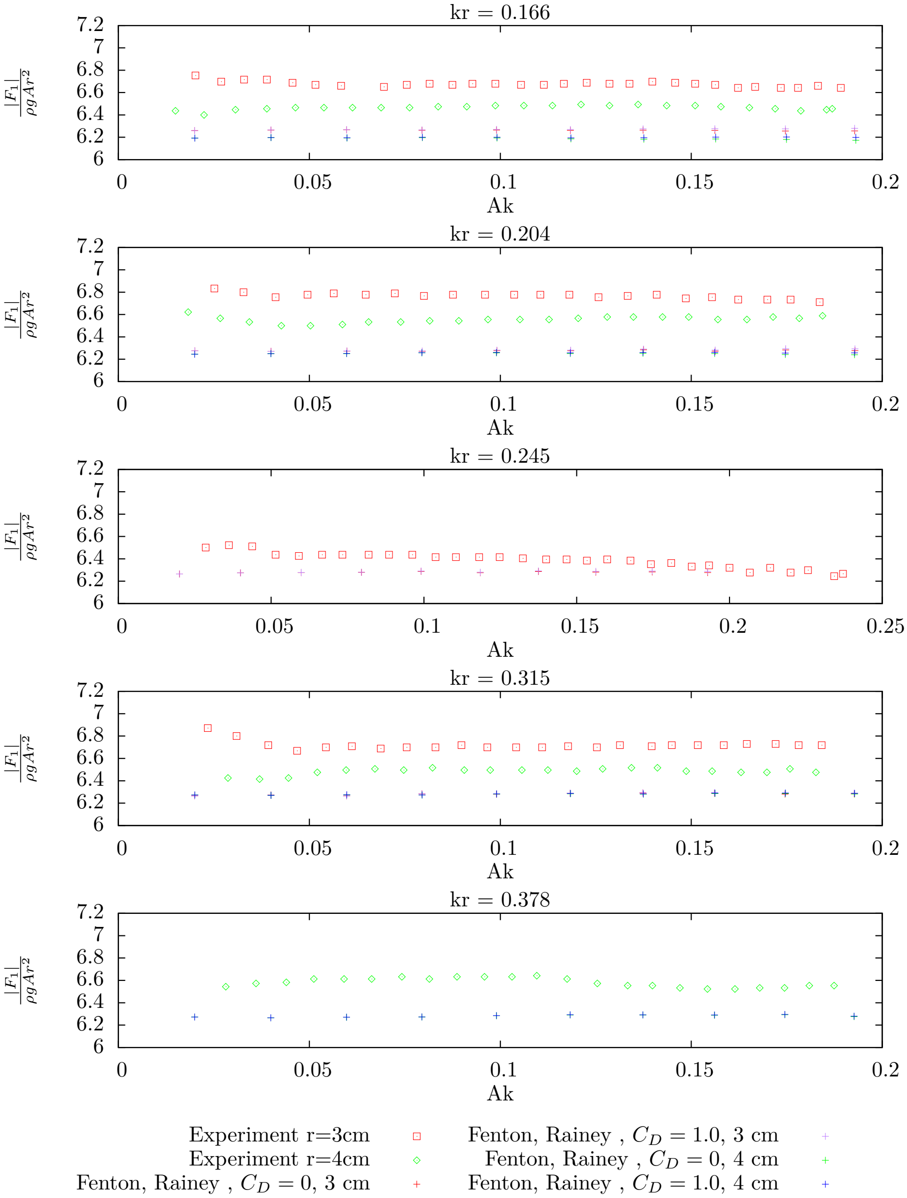

Figure 9.8: First harmonic component of wave force, for various kr values. Fenton generated incident waves, and forces by Rainey's expressions, with and without drag.

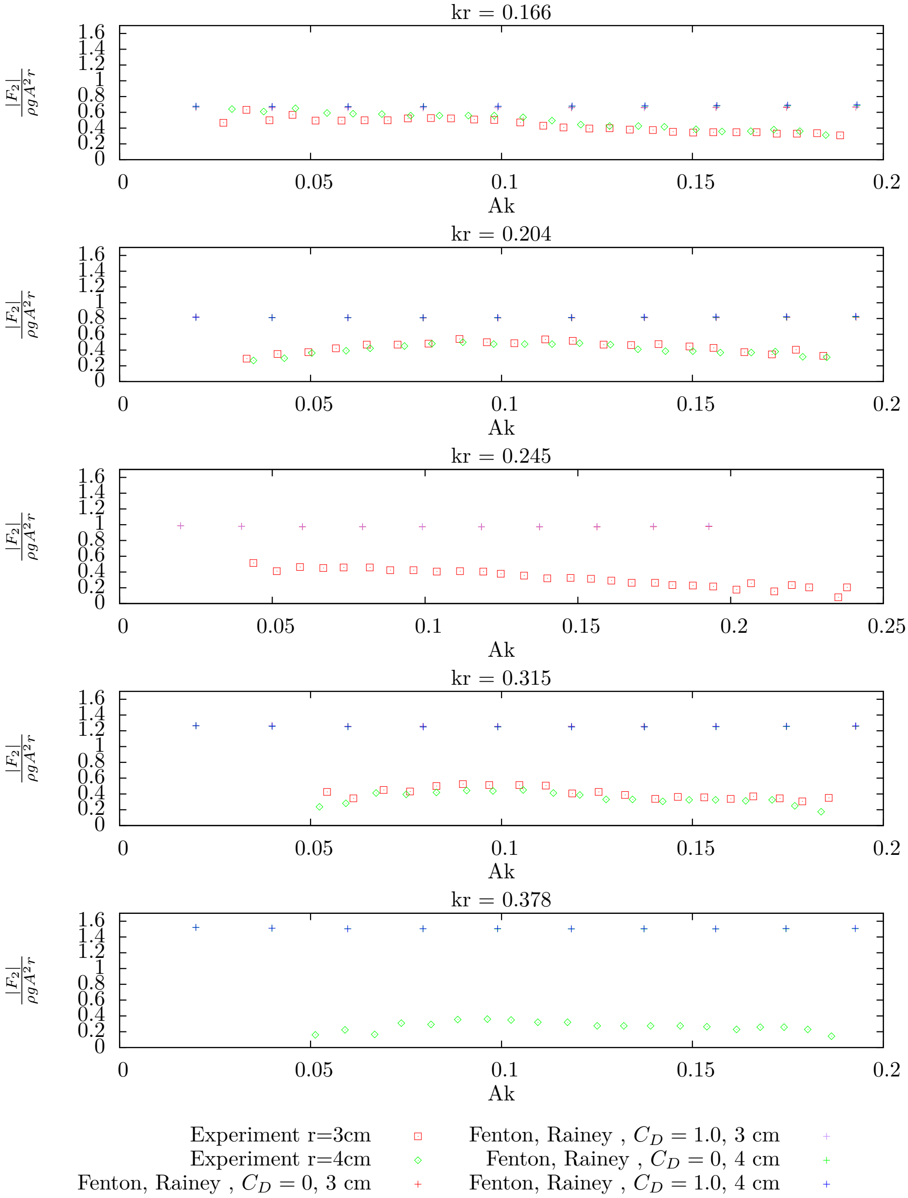

Figure 9.9: Second harmonic component of wave force, for various kr values. Fenton generated incident waves, and forces by Rainey's expressions, with and without drag.

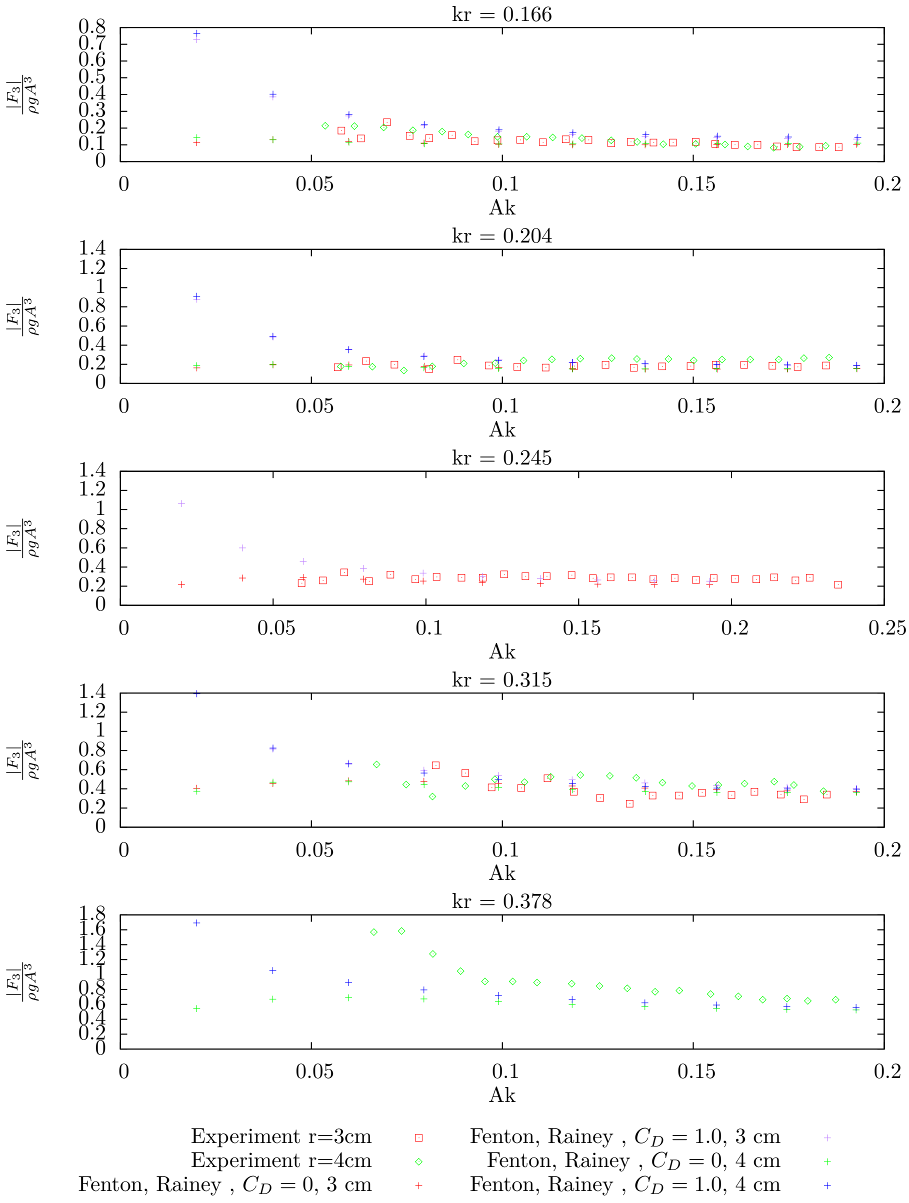

Figure 9.10: Third harmonic component of wave force, for various kr values.Fenton generated incident waves, and forces by Rainey's expressions, with and without drag.

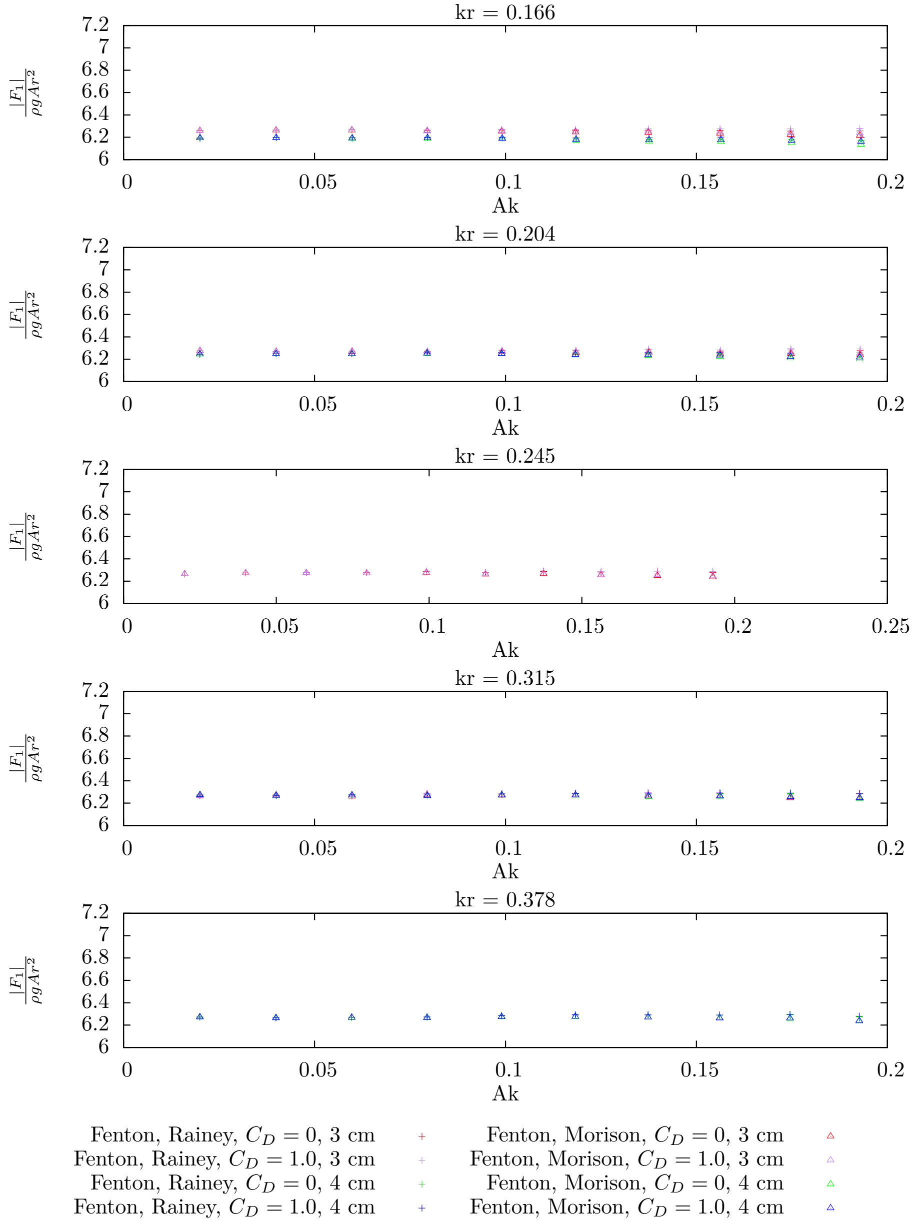

Figure 9.11: Comparison of first harmonic component of wave force, for various kr values. Fenton generated incident waves, and forces by Morison and Rainey, with and without drag.

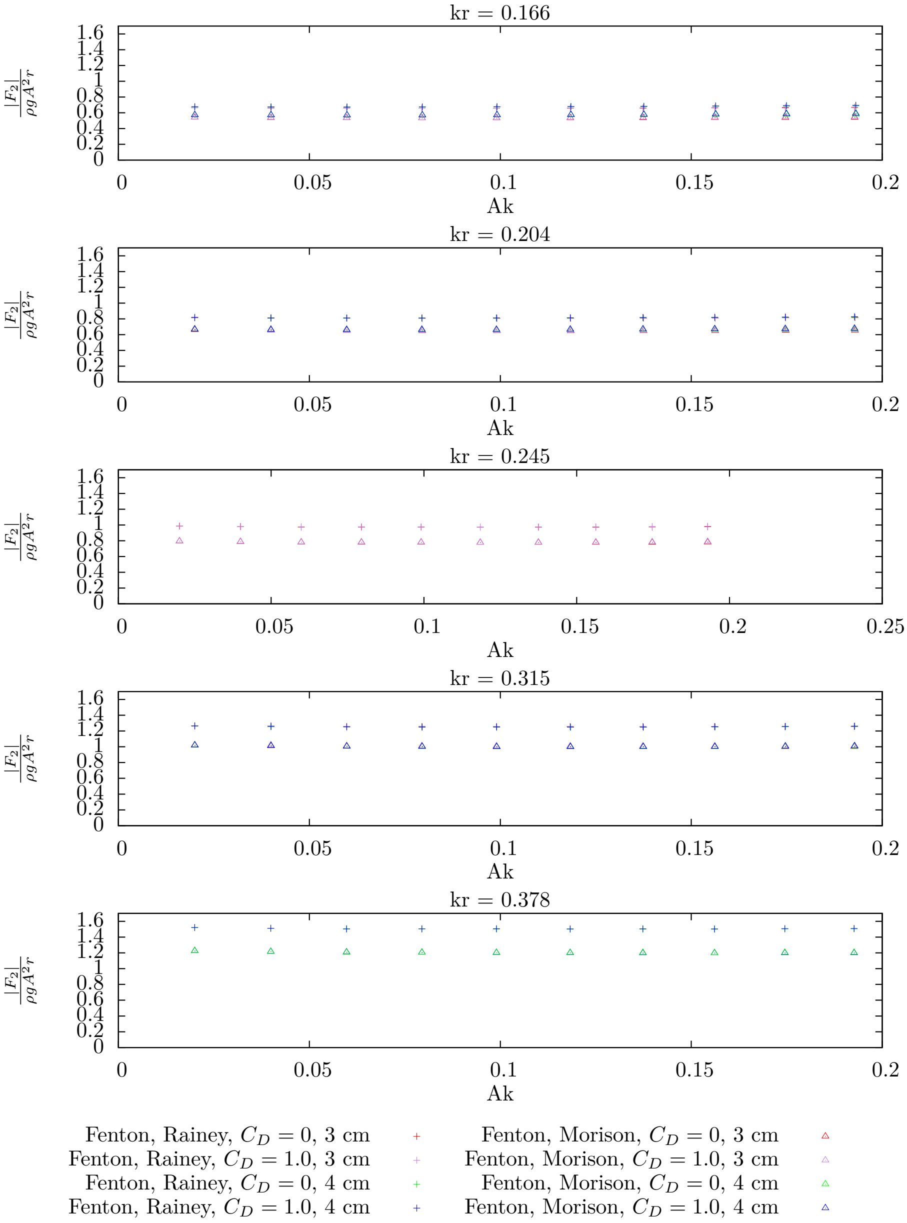

Figure 9.12: Comparison of second harmonic component of wave force, for various kr values. Fenton generated incident waves, and forces by Morison and Rainey, with and without drag.

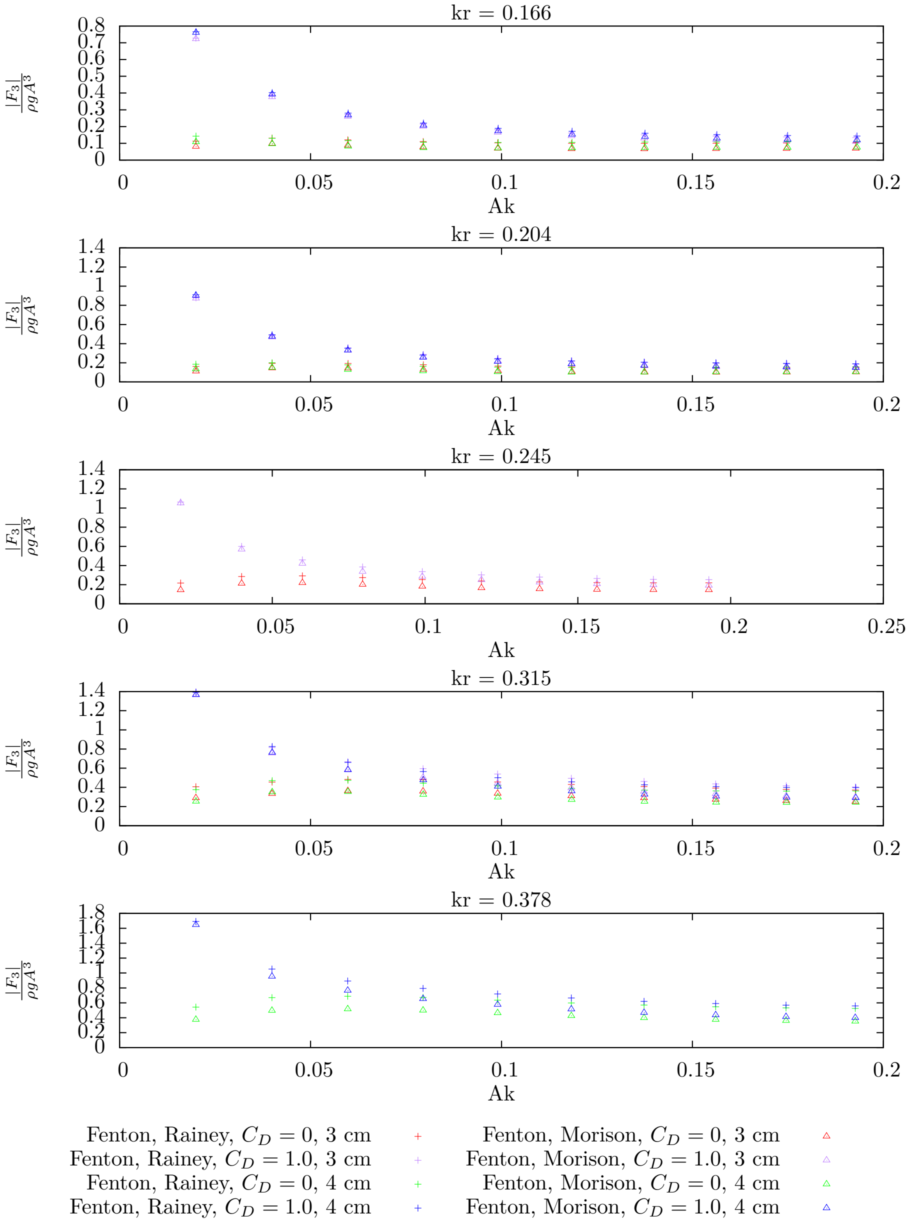

Figure 9.13: Comparison of third harmonic component of wave force, for various kr values. Fenton generated incident waves, and forces by Morison and Rainey, with and without drag

9.5 Trendline over kr

Since the theory utilised is a slender body theory, it is interesting to investigate how the ratio between calculated values and experimental values changes over the range of kr values used. From the figures it appears that the nondimensional first and second harmonic loads are almost constant over the kA range. As a rough simplification, say that the average over all kA values is representative for the load for a given kr. This makes it possible to calculate the average of the numerical calculations and the experimental values, and try to find some kind of trend regarding the error between the two.

The average of the nondimensional loads for each kr value is calculated, both for the experimental, and numerical values. Then the ratio $\frac{\text{Avg.Numerical}}{\text{Avg.experimental}}$ is calculated and plotted for each kr value.

The third harmonic load from the experiments seems more dependent on the kA value, but for the higher range of kA values it seems to converge against some kind of asymptotic value. Also there is a clear difference between the loading with and without viscous drag. The potential load is almost constant over the range of kA values, while the viscous component has a clear dependence on kA. The same procedure of calculating mean values over the kA can also be used for this load, but care should be taken with the results.

Figures 9.14 to 9.16 shows the trendlines for the ratio between the average loads, plotted against the different kr values.

The first harmonic load seems to have a close to constant ratio, which is close to one. No practical differences seems to exist between calculations made Morison and Rainey, or with and without drag for the Fenton case. There are also no difference between Fenton generated waves and linear+wheeler.

The third datapoint for the cylinder with diameter $D = 3$ [cm] should be read with care, as it appears to be an uncertainty in the experimental values. This uncertainty can be illustrated by looking at for instance fig 9.8, where for $kr = 0.245$ there seems to be lower forces in the experiment than for both the case $kr = 0.166$ and the case $kr = 0.315$. It is strange with this behaviour, especially when the cylinder with $D = 4$ [cm] does not seem to have such a behaviour.

The second harmonic load shows some exciting features. First there is a clear difference between which load formulation that has been utilised, with Rainey predicting higher loads for all cases. For the largest cylinder the ratio between calculated and experimental values seems to have a close to linear dependence on kr, or alternatively slightly exponential. This is true for both Fenton generated waves and also linear waves. The smallest cylinder does not show this behaviour, with the third datapoint significantly different from such descriptions. The third datapoint is the same point that has shown some uncertainty in the first harmonic. It appears that also for the second harmonic the experimental values for this datapoint shows low values compared to the case before and after.

Fenton waves are overpredicting the load for all kr for both load models, but with reasonably good agreement for the two lowest kr values. The linear waves with Rainey seems to give quite good comparison with the experiments, and loads with Morison seem to underpredict the load for all kr. For the Fenton waves no discernible difference seems to be present between including the viscous drag term or not. This is expected, as the viscous drag should only produce odd harmonic components.

It is interesting to note that for the second harmonic, the difference between the calculated ratio for Rainey and Morison appears to be more or less equal for the two wave models, i.e. Fenton and linear waves. This indicates that the difference between the two load models for the second harmonic is not largely dependent on the incident wave model.

The picture of the third harmonic is a bit more chaotic. Remember from the results that when viscous drag was included for the Fenton waves, very large third harmonic component was present for the lowest kA values, but as the kA value increased better fit between experiment and numerical results where present. This means that when comparing the mean value over kA there might be unrealistic large difference between the experiments and the numerical. This can clearly be seen on the results of the load without drag (this load is almost constant over kA values for each case), where the there is on average only a slight underprediction by the numerical model.

For the case of linear waves, it was observed that there was practically no third harmonic load for the highest kA values, yet on average the load seems to be ≈ 0.5 of the experiments. This is not real, and is once more the result of very large loads at the lower kA range. Therefore no discussion is made on the trend of the third harmonic.

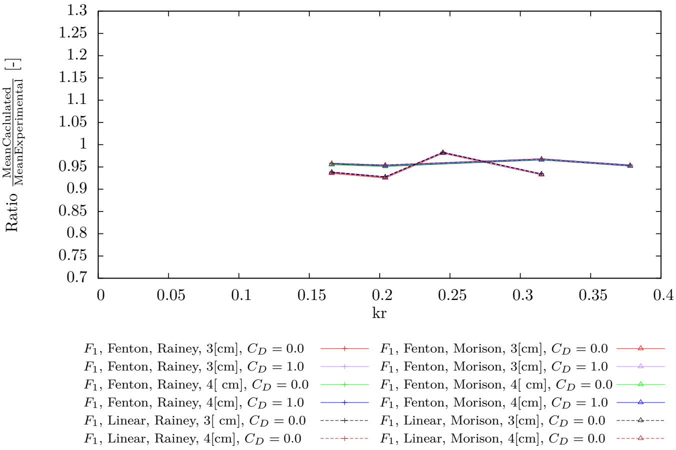

Figure 9.14: Trendline over kr for the first harmonic load, waves by linear and Fenton, loads by Morison and Rainey.

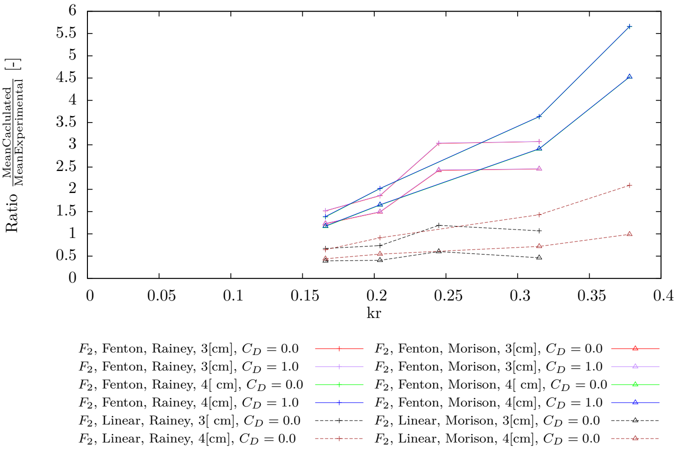

Figure 9.15: Trendline over kr for the second harmonic load, waves by linear and Fenton, loads by Morison and Rainey.

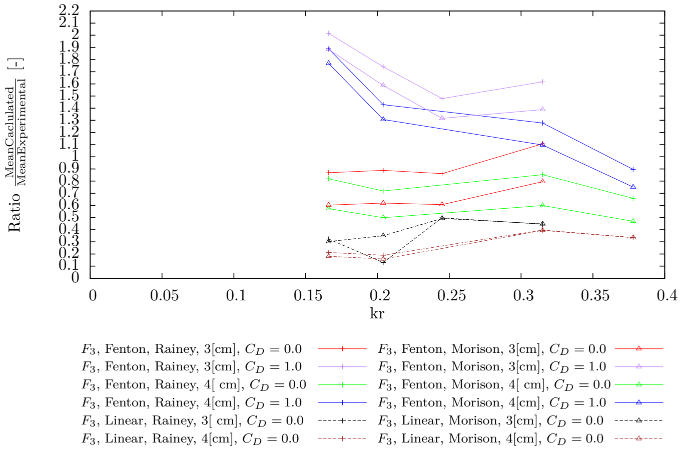

Figure 9.16: Trendline over kr for the second harmonic load, waves by linear and Fenton, loads by Morison and Rainey.

9.6 Discussion of the Results

The first harmonic load, is slightly underpredicted consistently for all values of kA and kr. This is true for both Fenton generated incident waves and linear waves. The numerical calculations seem to be minimum $90 - 95\%$ of the experimental values. The results are similar to the calculation by Morison's equation, and also to calculations with linear waves. Thus there is no improvement in the first harmonic load by using more advanced wave theories or another load formulation. There seems to be no practical difference when including the viscous drag in the Fenton calculations.

The second harmonic load is overpredicted with Fenton generated incident waves. It is clear from fig 9.9 that the amount of overprediction increases with increasing kr numbers. It is expected that the error should increase with increasing kr numbers, since this means that the slenderness of the structure compared to the wave is diminished, and the theory used assumes slender structures. Quite good comparison is obtained for the lowest kr value, also the second lowest case shows quite good agreement. Tromans et al. (2006) reports that the second harmonic load is overpredicted. The overprediction of the second harmonic load is in Tromans et al. (2006, page 44) partly contributed to the neglection of far-field diffraction effects when using slender body assumptions. It is observable that the inclusion of viscous loads have little to no effect, which is expected since it should only produce odd harmonic loads. In general the error is acceptable for the lowest kr values, but the overprediction may be a bit too conservative for the highest kr-values.

As commented under section 5.6 there seems to be a big error for the cases where the wave length is smaller than ≈ 10 times the diameter of the structure, but that the error seems to be smaller if the structure is allowed to move. Calculations have also been done with a stiff cylinder (not reported here), but it does not show significantly different results than the calculations performed here. This might be due to the fact that the cylinder has a natural frequency of 25 [Hz], which is 15 times larger than the waves with the highest frequency in the experiments. This means that very little motion of the cylinder should occur due to a very stiff cylinder.

There is also a possibility that the Fenton generated waves do not give similar conditions as waves in the experiment. In Grue and Huseby (2002) they describe the experimental waves to be close to pure Stokes waves, with a single frequency in the velocity field. This was chosen to ensure that the nonlinear loads are caused solely by the presence of the structure. The Fenton generated incident waves used in FAST had 30 harmonic components, which means the incident wave kinematics will have higher harmonic components by itself. This will lead to larger loads for the higher harmonics, than the experiment. By investigating the coefficients for the Fenton waves, it can be found that the first harmonic coefficient are clearly dominating the solution for the field, being a factor 1000 larger than the next component. The big question is whether the kinematics in the experiment truly only contains one frequency, and how well the experiment is represented with the Fenton generated waves.

The linear incident waves shows results with very good agreement with the experiments for the second harmonic. Rainey's expression seems to have better agreement with the experiment than Morison's equation with this wave model.

The linear waves contains only one frequency, and it was seen that Rainey's equation produced loads that were quite similar to experiments. With Fenton waves there is an overprediction. It can thus be concluded that the new load model performs fairly good for the second harmonic load, but has a tendency to overpredict the load. How much the load is overpredicted is difficult to quantify, because it is difficult to compare the waves used in FAST with the exact waves from the experiment.

For the third harmonic loads with Fenton waves, the calculations without viscous drag seems to slightly underpredict. The error is largest for small kA-values, and for the largest kA-values quite good comparison exists. The inclusion of the viscous drag seems to give results more similar to the experiment, or to a slight overprediction of the load. In general the third harmonic load is reasonably good predicted by Rainey's load model and the Fenton generated waves for the high kA range.

The results obtained by Morison's equation and Fenton waves shows underprediction of the third harmonic load for all but the lowest kr, even with Fenton waves and viscous drag included. The fact that this load model produces significant third harmonic loads is a sign that significant higher harmonics are present in the fluid domain.

For the case of linear waves, there is however large differences, both with Morison's and Rainey's expressions(analytical and numerical calculations), between the experiments and the numerical results. For the case where loads are calculated by Morison, it was expected, as it has been shown that there should not be a third harmonic component present. It is however more surprising for the Rainey case. From the expression of the force, it is clear that the surface intersection force is dependent on the free surface elevation, and it's slope. The experiment is said to be carried out with a close to pure Stokes wave, which have sharper crests than a linear wave. It is possible that the different wave profile is part of the cause of the bad results for the third harmonic load calculated by Rainey, with linear waves. As mention in section 9.3 another possibility is that viscous drag is not included and lastly that the third harmonic load is not good enough represented by Rainey's expressions.

The difference between the the two load formulation for the third harmonic can also be used to judge how much the nonlinearities in the incident waves affects the higher harmonic loads. The loads from Morison stands as a reference for the nonlinearities in the incident wave field, since all third harmonic loads should originate from nonlinearities in the waves. The difference between the two models is thus what the nonlinearities from the load formulation produce. As can be seen from figure 9.13 there is very little difference for the lowest kr values. The difference between them increase with increasing kr number. For $kr = 0.378$ there is a clear difference between them, but is less than half of the nondimensional load produced by Morison. This indicates that the nonlinearities in the incident waves are dominating over the nonlinearities in the load formulation for slender structures.

To summarise, it is clear that quite good comparison between experiments and numerical calculations has been obtained. Potential sources for discrepancies between the results have been discussed, but no conclusion has been made due to it not being possible to compare the exact wave elevation in the experiments and the numerical calculations.

It is noteworthy that the comparison has only been made with respect to the amplitude of the load components, and not the phase of the load with respect to the incident waves. Tromans et al. (2006) report of errors in the phase from the load models, when compared to experiments. This off course might be valid for the present calculations, but has not been investigated.

It has been found that for loads on a general slender body structure, it appear to be a possible improvement for the load calculations if the force is calculated with Rainey's expressions instead of Morison's equation. This conclusion is reached based on the results showing a better comparison with experiments. If linear waves with wheeler stretching are used, the first two harmonics are farily good predicted by Rainey. It has also been shown that using nonlinear waves further improves the comparison in the higher harmonic loads, and a clear advantage is present by using a wave model that incorporates nonlinear effects. It is also noted that for a slender structure the nonlinearities in the incident waves are more significant than the nonlinearities in the load formulation.

10 | Fully Coupled Simulations

So far the performance of the new load model has been compared with the old model and experiments with a cylinder in waves, without the effects of the turbine. The next logical step is to use the new model in a realistic load condition, and see how it compares to the old model. For this purpose, both linear incident waves and fully nonlinear waves generated by the MEL-procedure from section 6.2 will be used.

The goal of the simulations with linear incident waves is to investigate if there is any practical difference between the two load models in linear waves. For the fully nonlinear waves the goals are to see if any ringing occurs in the structure, and if there is any difference between the two wave models when more accurate wave kinematics are used.

Marino et al. (2013) has investigated the difference between the linear solution and a fully nonlinear solution, and found significant differences. In their simulations they even found ringing response in some of the steep non breaking waves as well as in breaking waves.

In section 4.3 the phenomenon of ringing was contributed to both steep breaking waves that slam into the structure and thereby excite a wide range of natural frequencies in the structure, and also to moderately steep waves, that do not slam into the structure, but create higher order loads. It is of the latter case that these simulations will try to predict.

Since the difference between the two load models are in the higher order terms, and these terms are significantly smaller than the first order term, it is important to simulate the worst possible sea states, where the wave elevations are big enough for these terms to have any significance.

From a time series alone it can be quite difficult to say something quantitatively about the difference between the load models. Instead by studying the power spectral density (PSD) of e.g. the bending moment at the mudline or the force, it is possible to investigate how the power of the time series is spread out over frequencies, and hopefully be able to discover differences between the two load models. By power it is meant the square of the time signal, so that the unit for the PSD of the moment is Nm^2/s if the frequency is given in Hz. For the force the PSD would have unit $N^/s$.

The power spectral densities reported in this chapter have been estimated using Matlab's built-in function pwelch. For a reference on this function the reader is referred to Matlab's user guide.

The downside of investigating the results using a PSD of the time series, is that it is not possible to connect the frequency content with when it occurred. To have a representation of the frequency content over time it is possible to use either a Wavelet transform, or an Emperical-Mode-Decomposition(EMD) with a Hilbert-Huang transformation(HHT) to obtain the Hilbert-Huang-spectrum(HHS).

The EMD breaks the signal down to well behaved Intrinsic Mode functions(IMF), which it is possible to take the Hilbert transform of. The IMFs needs to be close to orthogonal for the procedure to be accurate, therefore care should be taken when reading the results, as it is not certain that the calculated IMFs are always close to orthogonal. Due to this the HHS will only be used on small time windows to give indications of frequency content. For details about this process of calculating the frequency content in time, the reader is referred to e.g. Huang et al. (1998) or Rilling et al. (2003). The routines used here to calculate the HHS has been developed as part of the latter reference. A choice has been made to only calculate this for some special cases, because many answers can be found also from the regular PSD.

Since the interest is to study the worst sea states, from table 2.4 SS 5-7 will be simulated. When comparing that table with the wave statistics in table 2.2, it was found that the T_P values, in the statistics closer to the area of interest, was slightly lower than the ones reported in table 2.4. Therefore the following load cases will be used:

Sea State	H_s	T_P [s]	$Wind_{90[m]}$ [kn]	$Wind_{90[m]}$ [m/s]
5	3.25	8	30.5	15.7
6	5	9	46.7	24.0
7	7.5	10	64.1	33.0

Table 10.1: Load cases simulated

To convert the wave speed to 90[m] height, the relation in eq. 2.5 has been used.

The incident wind field is calculated using the tool TurbSim provided by NREL, to create wind input files for FAST. It can produce turbulent wind by using several different spectra and techniques. For further details the reader is referred to Kelley and Jonkman (2007).

The simulation time that has been chosen is one hour, i.e. 3600 [s]. According to Veritas (2010) a sea state might have a duration of 20 min up to 3-6 [hours], hence it can be concluded that one hour is a realistic length of a sea state.

The last sea state has a mean wind speed that is larger than the rated cut-out wind speed of the turbine, equal to 25 [m/s] (from table 2.1). The second sea state has a mean wind of 24 [m/s], which means that in periods of the simulations the wind speed will be above the rated cut-out speed of the turbine.

It is my understanding that when the wind and the rotor speed are above threshold values, the control system should alter the pitch of the blades in order to reduce the load on the rotor. This is performed in order to try and keep a constant rotation speed. It is believed that the control system will be able to handle such strong winds as used here, but it might be interesting to see how the turbine behaves if it is manually placed in a parked condition. This is a possible solution if the control system is not able to handle the strong winds, or if bad weather is expected.

Since such a simulation is not very time consuming, simulations with a parked rotor have been run for all sea states, even though for the first condition it is not realistic (except if the turbine is subject to some kind of error).

Regarding the global behaviour of the wind turbine, it is believed that the deflection of the tower top can give valuable information of the behaviour of the system as a whole. This is because the tower top deflection is affected by the aerodynamic loads, the hydrodynamic loads, and the motion will in turn affect the control system and the aerodynamic loads on the rotor. The motion of the tower top is thus in reality fully coupled aero-hydro-servo-elastic motion.

Therefore, in order to investigate the behaviour of the system, the shear force at the mudline (which is equal to the total horizontal force on the structure), the bending moment at the mudline and the tower top deflection will be used to investigate the behaviour in the different analyses.

Finally, in order to investigate eventual resonant phenomena, it is noted that the first natural frequency of the tower bending is close to 0.28 [Hz], and the second natural frequency is approximately 2.4 [Hz], as found in section 2.4.

10.1 Linear Incident Waves

The existing feature in FAST of linear incident waves are used with the optional wheeler-stretching of the kinematics. From experience gained in my project thesis it is expected that the bending moment will be dominated by the aerodynamic loads. In general it is not expected that the linear waves are able to properly represent the waves that might cause ringing, so the occurrence of ringing in these simulations is doubtful.

By studying the results of the time series, very small differences were indeed present, so no time-series are presented here. In the section regarding resonant oscillations (section 10.1.1), some resonant phenomena will be investigated and time series presented. These time series show the characteristics of the difference between the two load models.

Figures 10.1 to 10.3 present the power spectral density for the simulations, both with a running turbine and also with a parked turbine.

The first thing to notice from the PSD-plots is that in the PSD of the shear force at the mudline, the range where the waves are present have the highest levels. This means that the wave force is actually dominating over the aerodynamic forces when one studies the shear force at the mudline. The PSD in this frequency range shows little differences between the running and the parked simulation, and also between Morison and Rainey's load formulation. FAST is employing a cut-off frequency in the incident wave spectra to avoid nonphysical high frequency waves, which is clearly seen on the PSD as a sharp decline for all cases.

For the next range of frequencies above the cut-off frequency, it is clear that there exist differences between Morison's and Rainey's load formulation. This can be seen most clearly for the parked simulation, but it is also clear that for the running turbine simulations there are differences between the two load formulations in the PSD of the shear force. Since this is above the cut-of frequency, this is due to higher order effects. For the parked simulation the difference is observable up to ≈ 0.75 [Hz]. For the running simulations this is observable up to ≈ 0.5 [Hz].

When investigating the PSD of the bending moment it is clear that there exists much power outside the range of linear wave forcing, and that the difference between the two load formulation is small to nonexistent for a running turbine. This is mildly surprising, since in chapter 9 it was found differences between the two load models regarding the second harmonic force in linear waves. One would expect that the different wave force on the tower would have some impact on the bending moment, which it clearly does not. This is an indication that the bending moment at the mudline is governed by the force on the rotor, which due

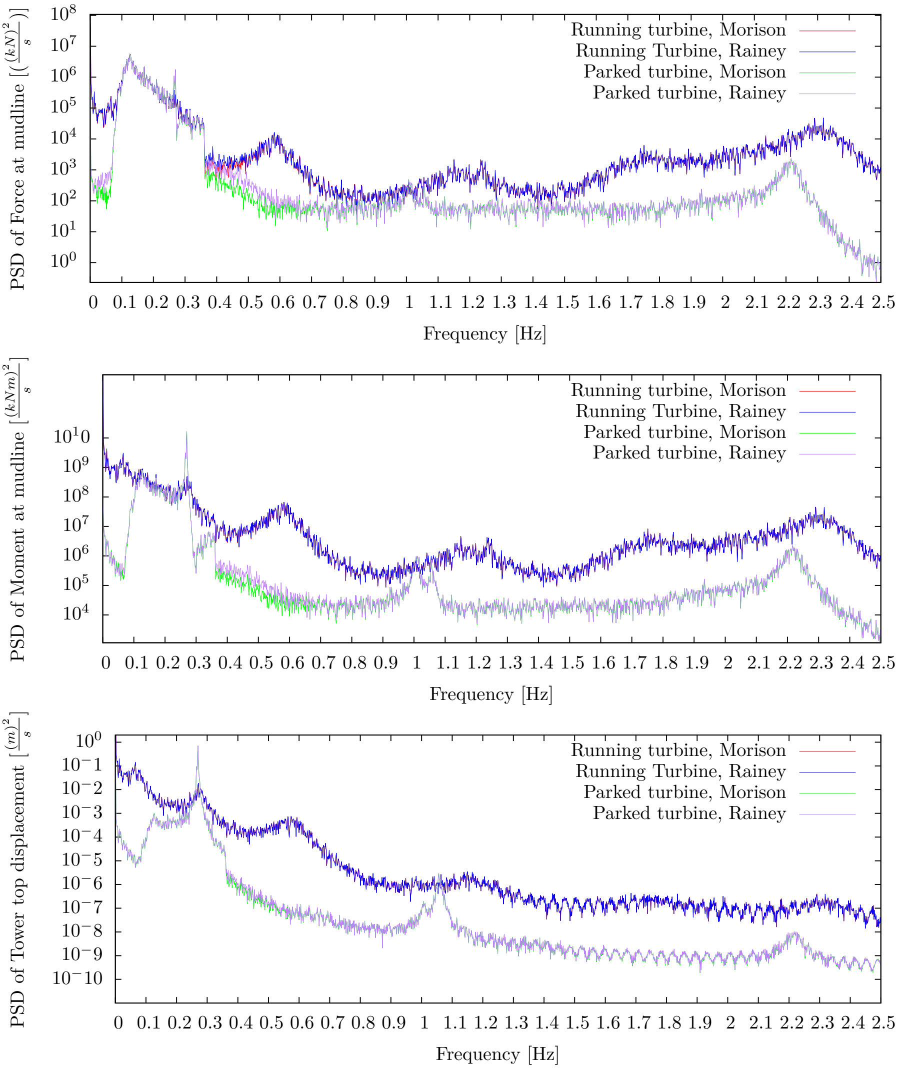

Figure 10.1: Power spectral densities of: Force at mudline, bending moment at mudline, and displacement of tower top in SS 5. Both simulations with a running and a parked Rotor. Forces by Morison and Rainey.

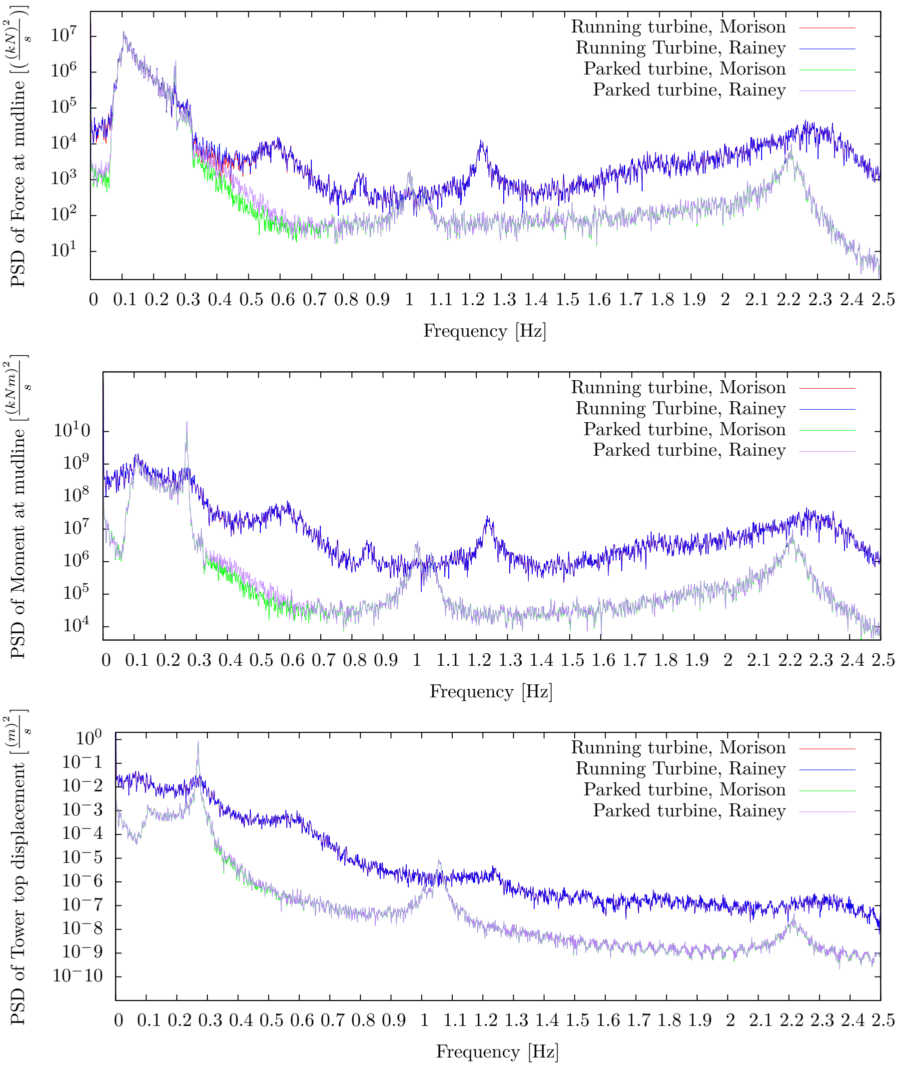

Figure 10.2: Power spectral densities of: Force at mudline, bending moment at mudline, and displacement of tower top in SS 6. Both simulations with a running and a parked Rotor. Forces by Morison and Rainey.

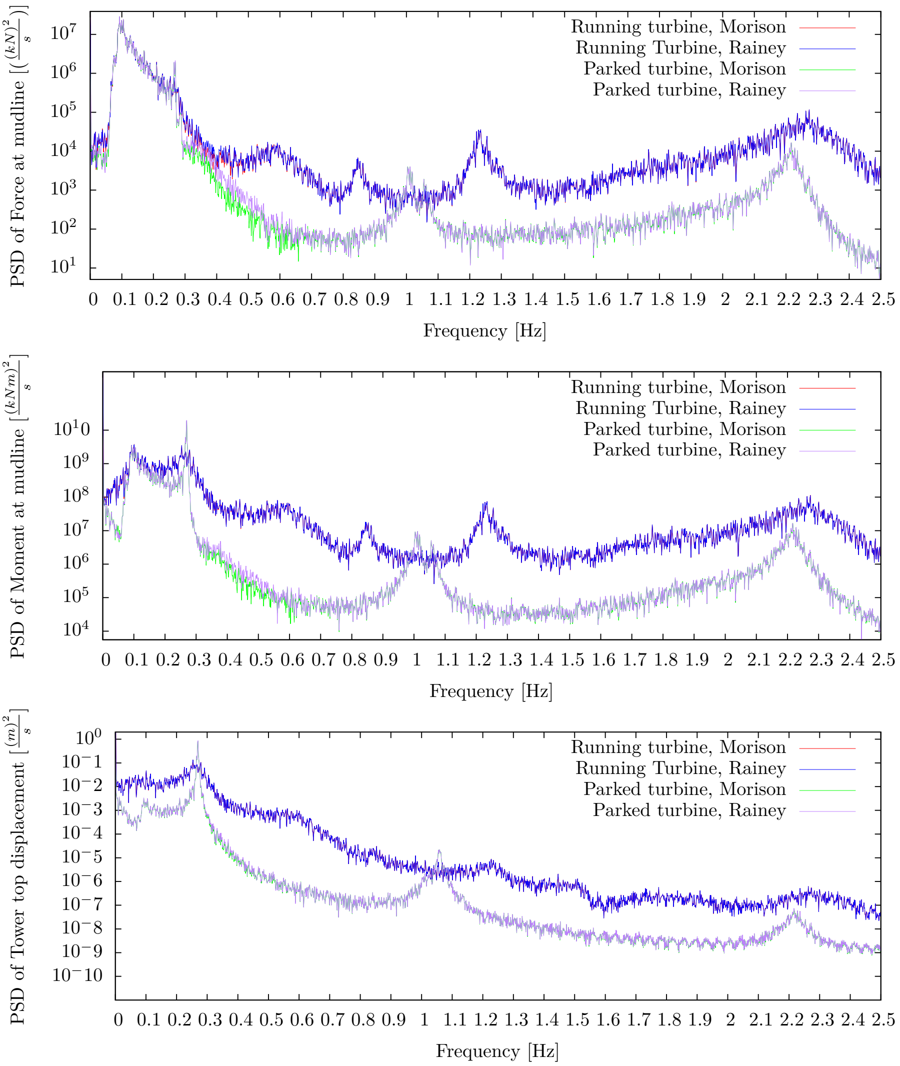

Figure 10.3: Power spectral densities of: Force at mudline, bending moment at mudline, and displacement of tower top in SS 7. Both simulations with a running and a parked Rotor. Forces by Morison and Rainey.

to the long arm creates much larger moments than the waves. This can also be seen in the displacement of the tower top that it is practically equal for the two models.

This means that for the wind turbine system in linear incident waves, there is no practical difference in which wave load model one uses, because the aero-elastic effect is clearly dominating the tower top motion.

The large peak at the resonant frequency for the case with a parked rotor might be related to low damping levels. The structural damping in the tower is set to 1 % of the critical damping for both modeshapes of the tower. According to measured damping rations for different structures found in Langen and Sigbjørnsson (2011), this might be said to be a reasonable value for such a steel structure. However, in a real monopile there are additional damping terms that might have significant importance. In a real installation the assumption of a clamped boundary condition at the seabed is not reasonable, there will be some kind of motion here. Motion of the structure in the seabed will generate additional damping forces.

To investigate the effect of damping, another set of simulations have been performed with increased damping levels. Since there is no easy way to implement the additional damping terms, the structural damping has been increased to 5 %. The point is not to make a totally realistic simulation, but to do another simulation with more damping, so the effect of damping can be compared. Figures 10.4 to 10.6 shows the results in terms of the PSD.

The simulations show that the peak at the natural frequency in the PSD of the tower-top displacement is significantly reduced for all sea states. Also at the high frequency range, around the second natural frequency of the structure, there is shown even greater reduction in the power.

The large reduction in PSD at the resonant frequency when additional damping was introduced can be an indication that the system is lacking damping in the parked condition. The topic of resonant motions and the effect of damping will be further discussed in the next section.

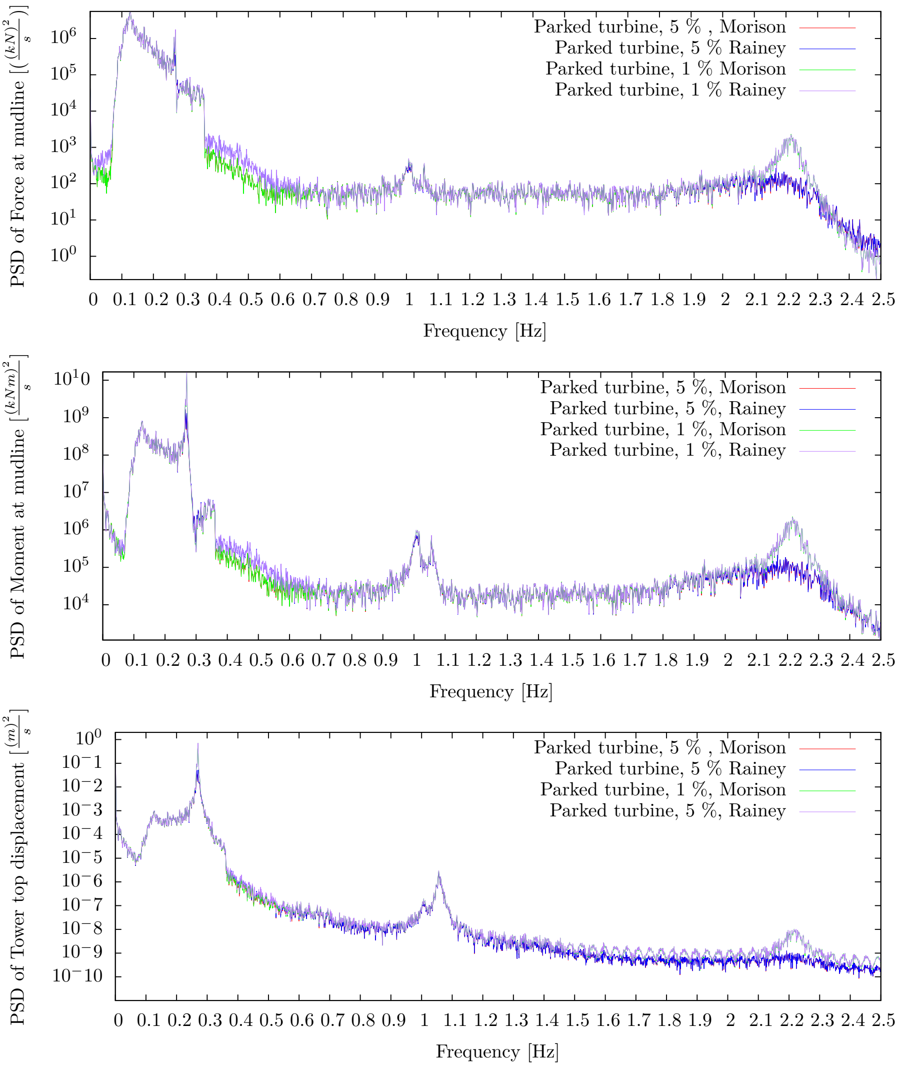

Figure 10.4: Comparison of the PSD for simulations with and without increased structural damping in SS 5. Forces by Morison and Rainey, linear incident waves with Wheeler stretching.

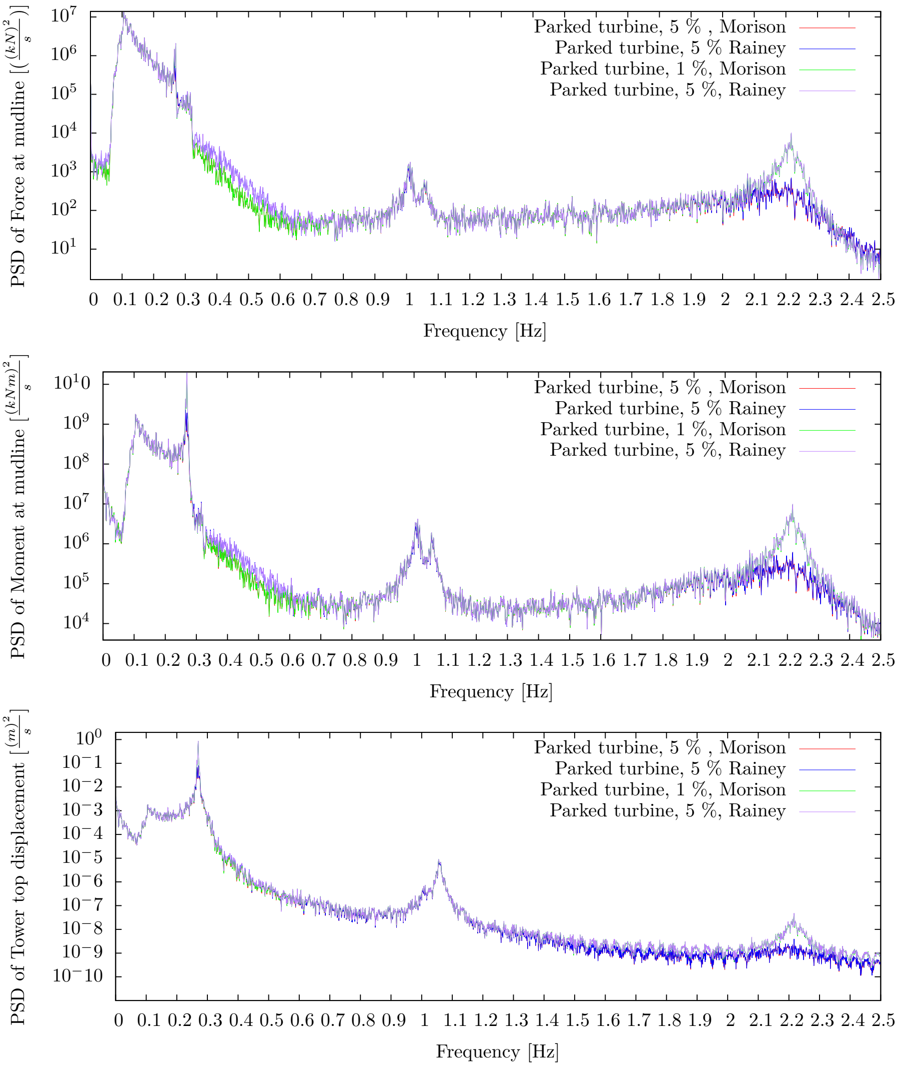

Figure 10.5: Comparison of the PSD for simulations with and without increased structural damping in SS 6. Forces by Morison and Rainey, linear incident waves with Wheeler stretching.

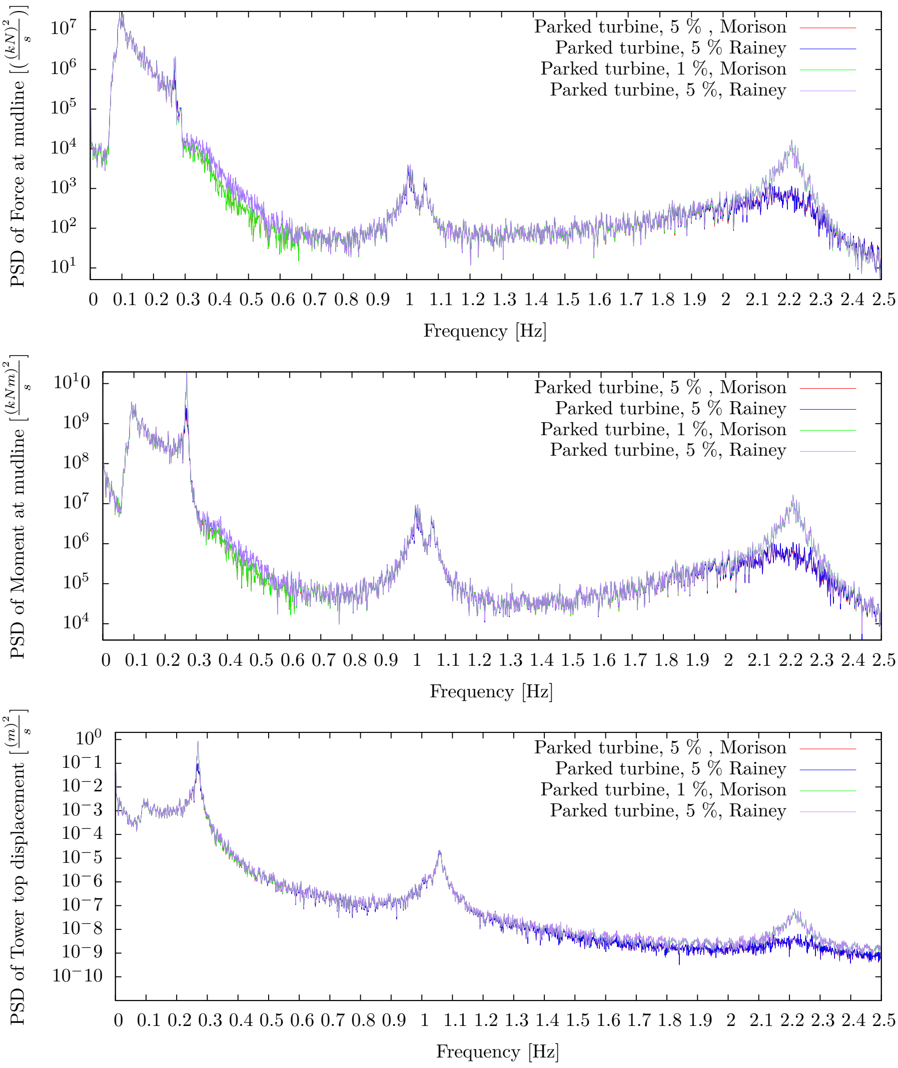

Figure 10.6: Comparison of the PSD for simulations with and without increased structural damping in SS 7. Forces by Morison and Rainey, linear incident waves with Wheeler stretching.

10.1.1 Resonant Behaviour

In the parked simulations there is a big peak at the first natural frequency of the tower in both the PSD for the bending moment, and also the PSD for the tower top displacement. It is possible that the structure in such a condition is undergoing steady state resonant oscillations also known as springing.

In figure 10.7 a comparison is made between the simulations with a parked turbine with normal damping, and with additional damping, for forces calculated by Morison's equation and also Rainey. It is clear that increasing the structural damping significantly reduces the amplitude of the oscillations, but that the oscillations still occur at the same frequency. No difference in the amplitude seems to be present between the load models. By looking at the period between each oscillation, it appear to be close to the natural frequency of the structure. The figure shows small differences in the shear force at the mudline between the highly damped and the normal damped system, but there are clear differences in the amplitude of the oscillations.

It is noteworthy that the maximum deflection of the tower top is quite small, with oscillations in the time window investigated of ≈ 0.1 [m]. This is not believed to be dangerous from a maximum stress point of view, but springing is usually considered to be more important for fatigue, where the large number of load cycles affect the life span of the structure.

However to really judge whether the structure is undergoing steady state oscillations, the frequency content in time needs to be investigated. The EMD with Hilbert-Huang transform has been used to create a Hilbert-Huang-Spectrum to investigate this. In figs. 10.8 and 10.9 the last 600 seconds of the tower top displacement in the simulation with a parked turbine in SS 5 are reported for calculations with both load models.

The figures of the HHS have been created by normalising by the maximum value, and plotting them with a logarithmic scale, where colors indicate the levels. It should be read so that the more intense red, the higher importance a frequency has at that time instance. What appear to be lines in the HHS, are actually each IMF where each line shows the frequency content of each IMF in time. In all the plots of the HHS, a white line is placed at 0.28 [Hz], indicating the approximate position of the first natural frequency of the tower, as calculated in section 2.4. Because the EMD-procedure may not produce exactly orthogonal IMFs, it is believed that the frequencies may be a bit inaccurate. Therefore oscillations in a small range around the white line are here considered as resonant oscillations.

From figs. 10.8 and 10.9 it can be seen that only small differences are present in the HHSs between the two load models. It is also clear that the tower top oscillates

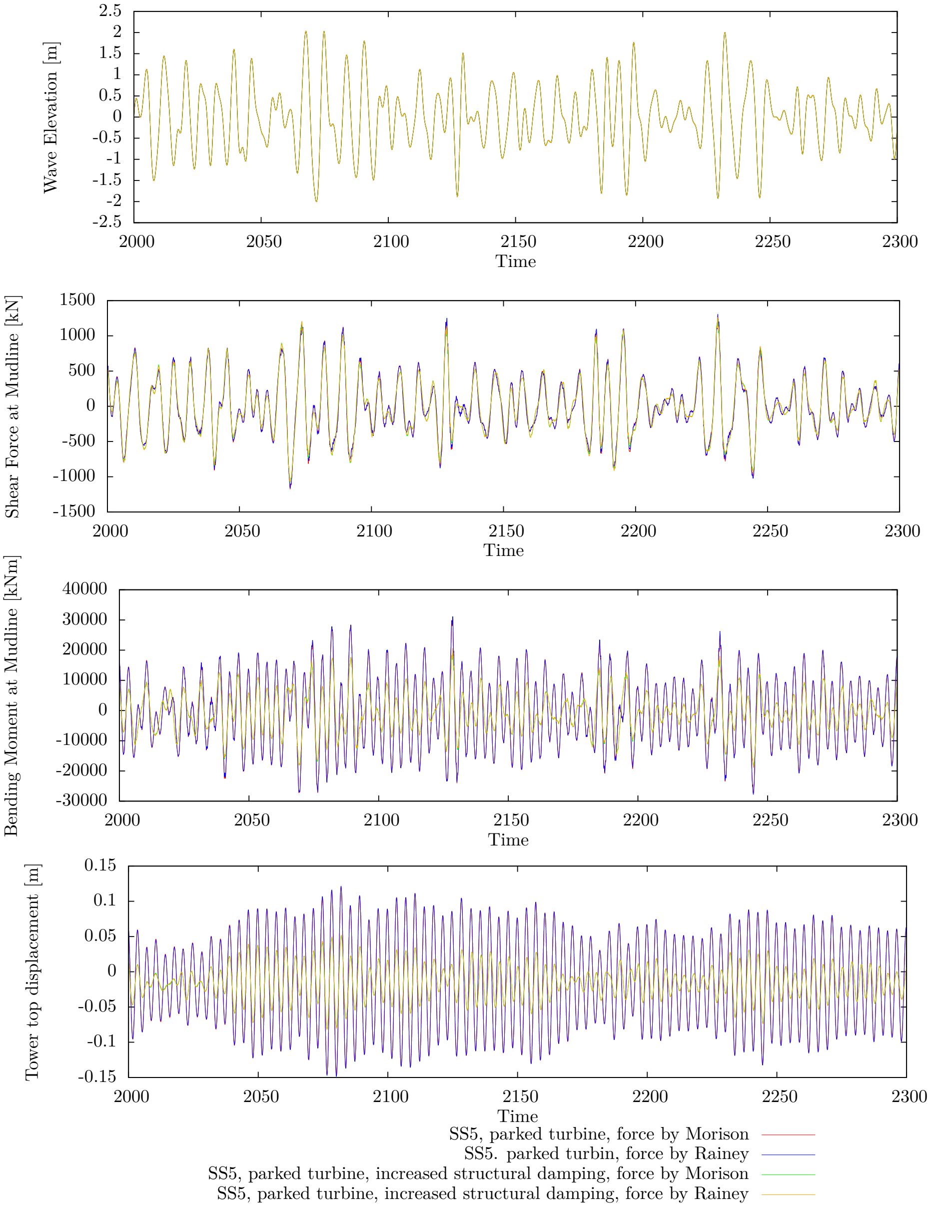

Figure 10.7: Comparison of a parked turbine and parked turbine with additional damping in SS 5.

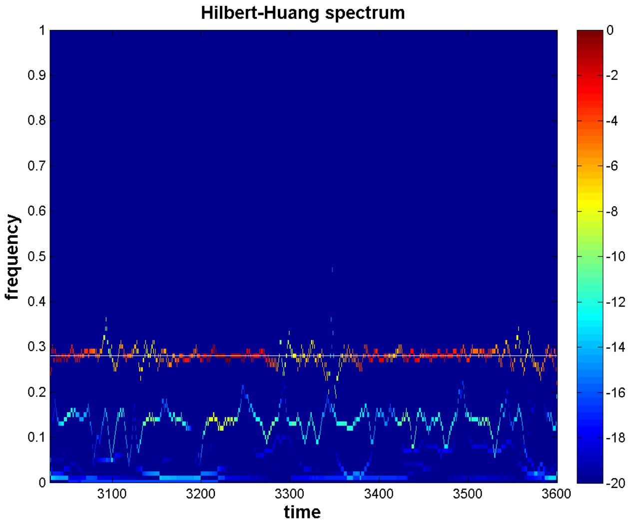

Figure 10.8: Hilbert-Huang-spectrum for the tower top deflection, last 600[s] of the simulation in SS 5 with a parked turbine, and forces by Morison's equation.

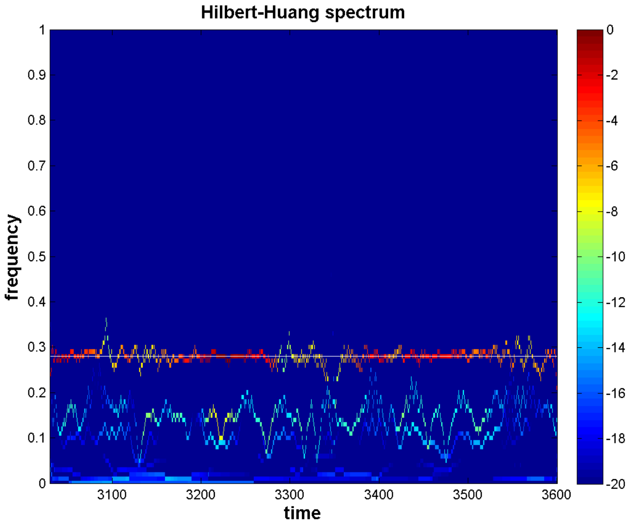

Figure 10.9: Hilbert-Huang-spectrum for the tower top deflection, last 600[s] of the simulation in SS 5 with a parked turbine, and forces by Rainey's expressions.

quite strongly with a frequency in the area around the resonant frequency. These oscillations are dominating for almost the whole time window investigated. This indicates that the resonant oscillations are present at nearly all time instances, and could be considered as springing according to the definition given in section 4.2. Even though the amplitudes are changing, the frequency remains more or less constant throughout. It appears then that the reference turbine is experiencing quite heavy springing when the rotor is set in the parked condition.

By comparing the PSD of the force on the running turbine and a parked turbine, it is clear that in this frequency range, the force is not very different from the two cases. It has also been shown that by increasing the structural damping, the peak at the resonance frequency is reduced, but it has not disappeared. This is an indication that the system is lacking damping in the parked condition, because the wave loads manage to constantly excite the structure, and keep it oscillating at the resonant frequency. It is believed that the springing is caused by nonlinear wave loads, because the natural frequency is well outside the range where the first harmonic should have any significant power.

To figure out if it is indeed caused by nonlinear wave effects, a possible solution could be to use no stretching of the incident wave kinematics, to obtain a consistent linear theory. However, the viscous drag load from Morison's equation will produce nonlinear forces, due to it's square dependence on the water particle velocity. Since Morison's equation is implemented in the relative form in FAST, it will produce important damping from the viscous drag. It is therefore not wise to run simulations with $C_D = 0$. Thus there is a paradox; if simulations are run with $C_D \neq 0$ nonlinear loads will originate from the viscous drag, and if simulations are run with $C_D = 0$ even less damping is present in the system. It has therefore been concluded not to try and figure out if the springing also occurs for a situation with only linear wave forcing.

What appears to be the cause of springing is the lack of aero-elastic damping, because the only aspect that is different is the missing loads produced by a running rotor. When the turbine is running it provides enough damping to inhibit these oscillations, but once the turbine is parked, the natural frequency of the tower is excited by the wave forcing. This means that parking the turbine in bad weather might actually be dangerous because it can lead to springing, which might cause fatigue problems. This is naturally depending on the actual structure and the stiffness of the tower. However, the NREL reference turbine is believed to be representative for bottom fixed turbines, so in general it is important to investigate the behaviour of the structure with a parked rotor.

The feature of springing has been found in the smallest investigated sea state, with both load models. It is not necessary to investigate the other sea states (SS

6 and SS 7), as it is only natural that springing is also present in these, due to even worse wave loading.

It will not be investigated, but there is a strong possibility for springing to also occur with a parked wind turbine in smaller sea states. This is believed because of the clear tendency to springing seen in SS 5. SS 4 has a $H_S < 2.5$ and range of T_P similar to that of SS 5. This is very close to the values for SS 5 used in the simulations, that causes severe springing.

By further investigations, it has been found transient resonant oscillations of the tower top in SS 6, presented in figure 10.10, with a HHS in figure 10.11. The HHS spectrum is only calculated for the case with loading by Rainey's expressions, but as the time series reveal, no difference is present between the two load models.

It can be observed that the transient resonant oscillations do not occur when the structure interacts with a steep wave, and at the time instance of the resonant oscillations at ≈ 2700 [s], the waves are actually relatively small. The resonant oscillations do not seem to have the same appearance as the classical ringing presented in figure 4.1. This behaviour is very strange and it leads to the possibility that it was actually strong winds, possibly coupled with the way the control system works, that created the resonant behaviour.

There is a possibility that in strong winds a large aerodynamic force could cause a large mean deflection of the tower top. If the control system then suddenly alters the pitch of the blades to reduce the rotor speed, the aerodynamic force will be reduced quite rapidly. This can cause the tower to experience resonant oscillations.

If this is the case, then these resonant oscillations in the tower may not be caused by the classical mechanisms of ringing presented in section 4.3. It is possible to investigate this by re-running the simulations with firstly a smaller mean wind speed, and secondly the original wind speed, but no incident waves.

For the case with a lower wind speed, the wind input from SS 5 has been used. In figure 10.12 the time evolution around the previous transient resonant oscillations is presented for the extra cases with either no waves, or a reduced wind speed.

For the tower top deflection and the bending moment, only small changes are present when no incident waves are present. However for the horizontal shear force, large differences are present when no incident waves are present. The tower top is still experiencing resonant oscillations, even with no incident waves, indicating that the strong winds and possible also the control system that causes this behaviour.

For the case with lower wind speed, large differences for the tower top deflection

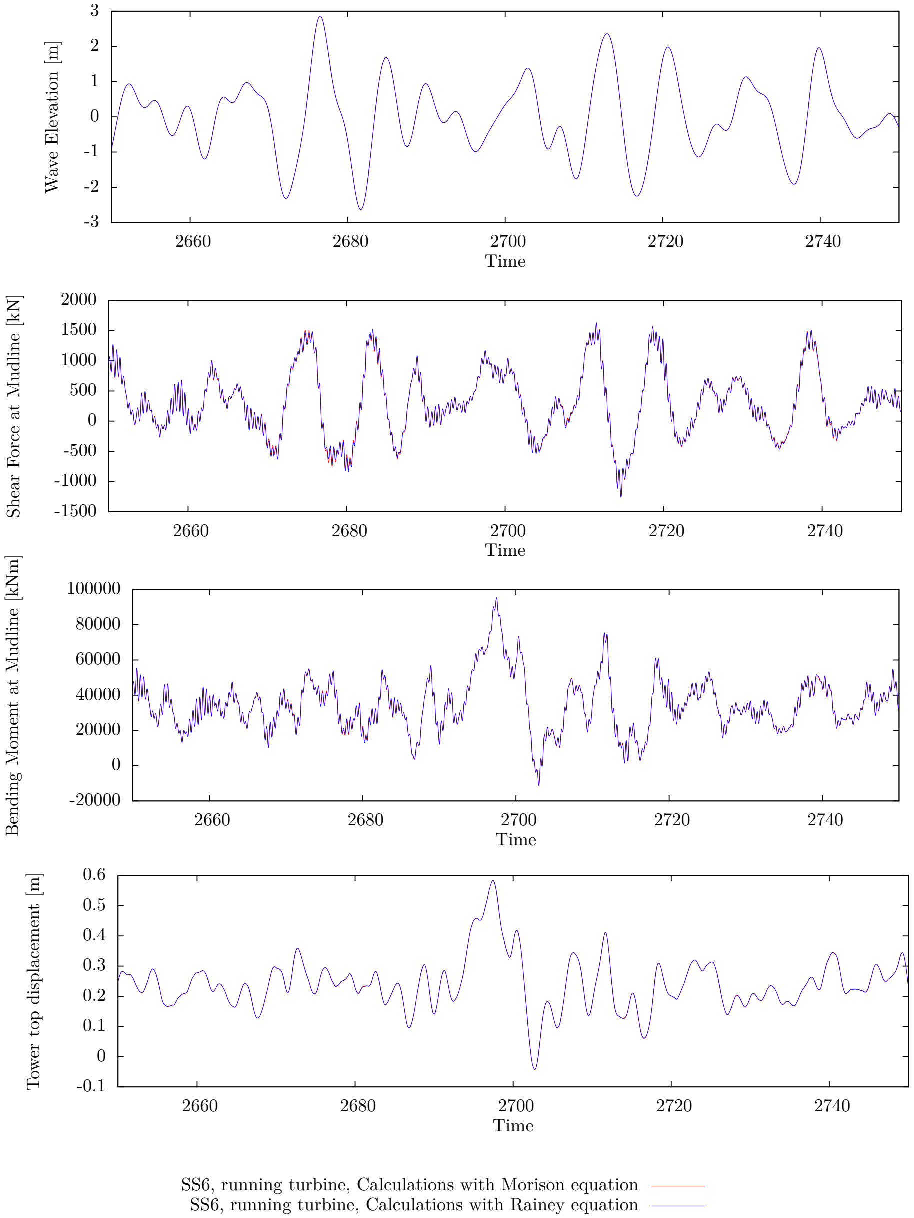

Figure 10.10: Time evolution of the wave elevation, shear force, bending moment and tower top displacement around the event at 2700 [s] in SS 6.

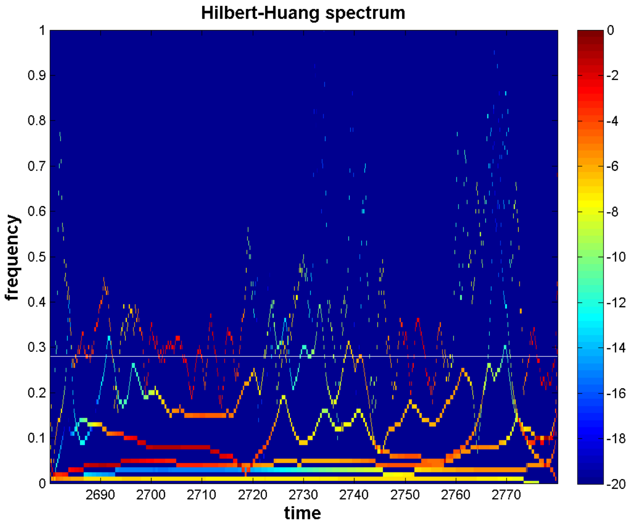

Figure 10.11: Hilbert-Huang-spectrum of tower top deflection around a burst like event at ca 2700[s], forces computed with Rainey's expressions.

and the bending moment are present, but the horizontal shear force are quite similar. It is also clear that the resonant oscillations in the tower top has been replaced by another behaviour.

The fact that the shear force is more or less equal in the simulations with the lower wind speed, but much smaller if the no waves are present, further confirms that the waves are dominating this load.

By investigation of the HHS of the event for the case of lower mean wind speed in figure 10.13, it is shown that the transient resonant behaviour of the tower top around 2700 [s] is indeed gone, and has been replaced by another lower frequency behaviour.

The simulations with a running turbine in SS 7 are a bit different from the others, because the mean wind speed is much larger than the maximum rated wind speed of the turbine. This should make the control system constantly try to keep the rotor under control. Considering the findings in SS 6, it is an even larger possibility for the wind causing resonant oscillations in this simulation.

It appears that the maximum in the PSD of the tower top deflection is at the first natural frequency of the tower, and in the time series it is observable with

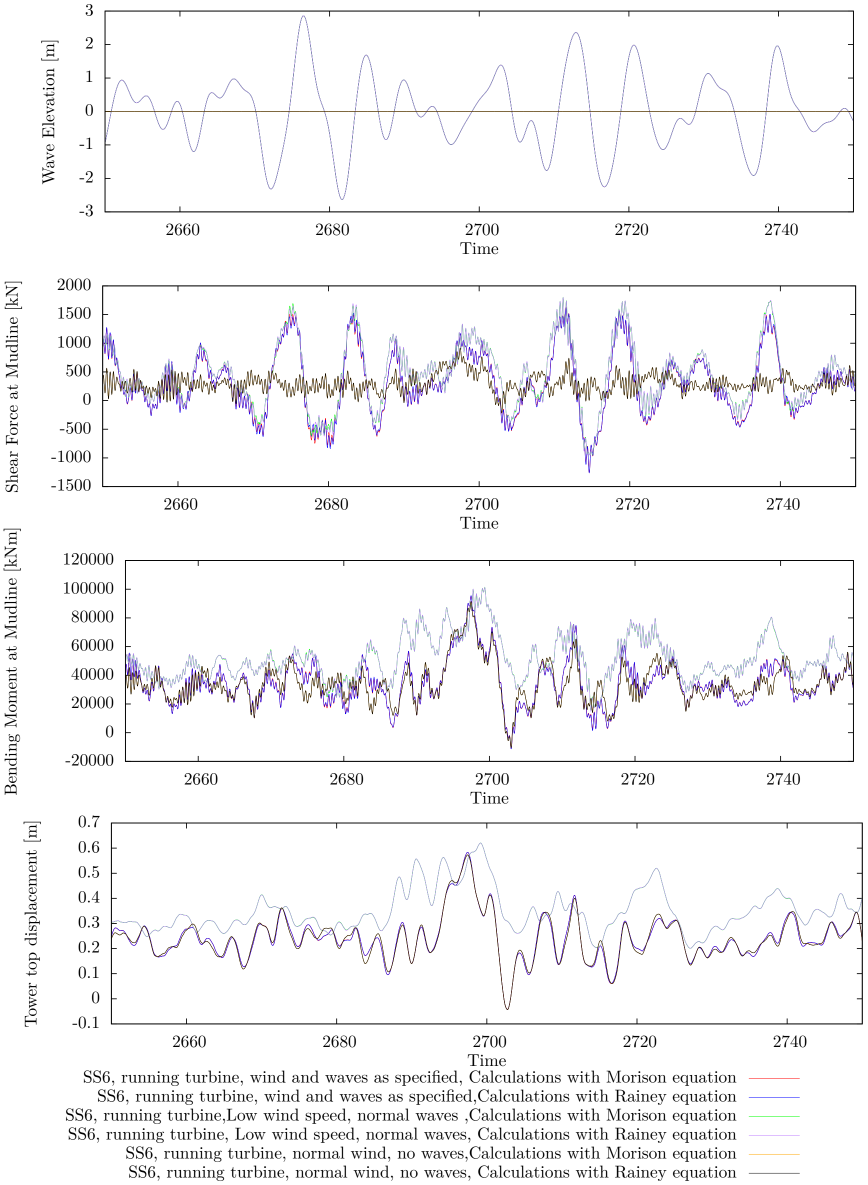

Figure 10.12: Time evolution of the wave elevation, shear force, bending moment and tower top displacement around the event at 2700 [s] in SS 6, with and without a lower wind speed and with or without incident waves.

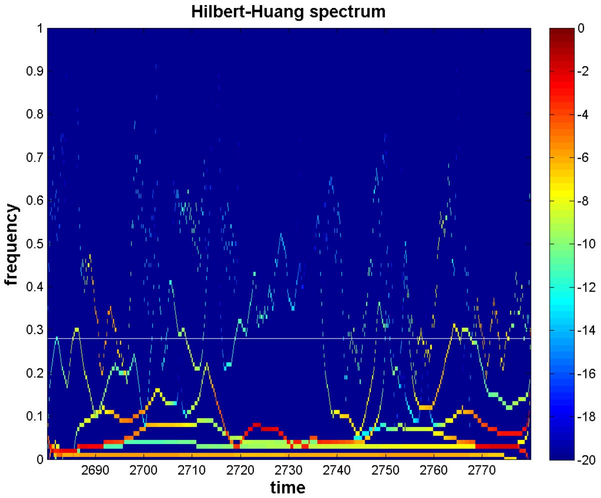

Figure 10.13: Hilbert-Huang-spectrum of tower top deflection around an event at ca 2700 [s], low wind speed,forces computed with Rainey's expressions.

oscillations that are close to the natural frequency on several occasions. One of the instances at ≈ 3500 [s] are presented in figure 10.14.

The time evolution shows small differences, with respect to which load model that is used, in the mudline shear force. For the other quantities no differences are present.

Contrary to the observed resonant phenomena in SS 6, the resonant oscillations start to appear at the same time as a large wave appears.

The instance has also been investigated with a HHS spectrum, presented in figure 10.15, for the case of forces calculated with Rainey's expressions. Due to the small difference in the time evolution, no differences are expected in the HHS between the load models, and it will only be shown for calculations with Rainey.

The HHS shows that there is a clear transient period where strong oscillations occur, with a frequency close to the natural frequency of the tower.

To investigate what causes the oscillations, the same procedure as for SS 6 has been used, and is presented in figure 10.16.

First of all, the simulations without waves show a clear reduction in the amplitude of the oscillations, but the frequency has not been changed. This is different from

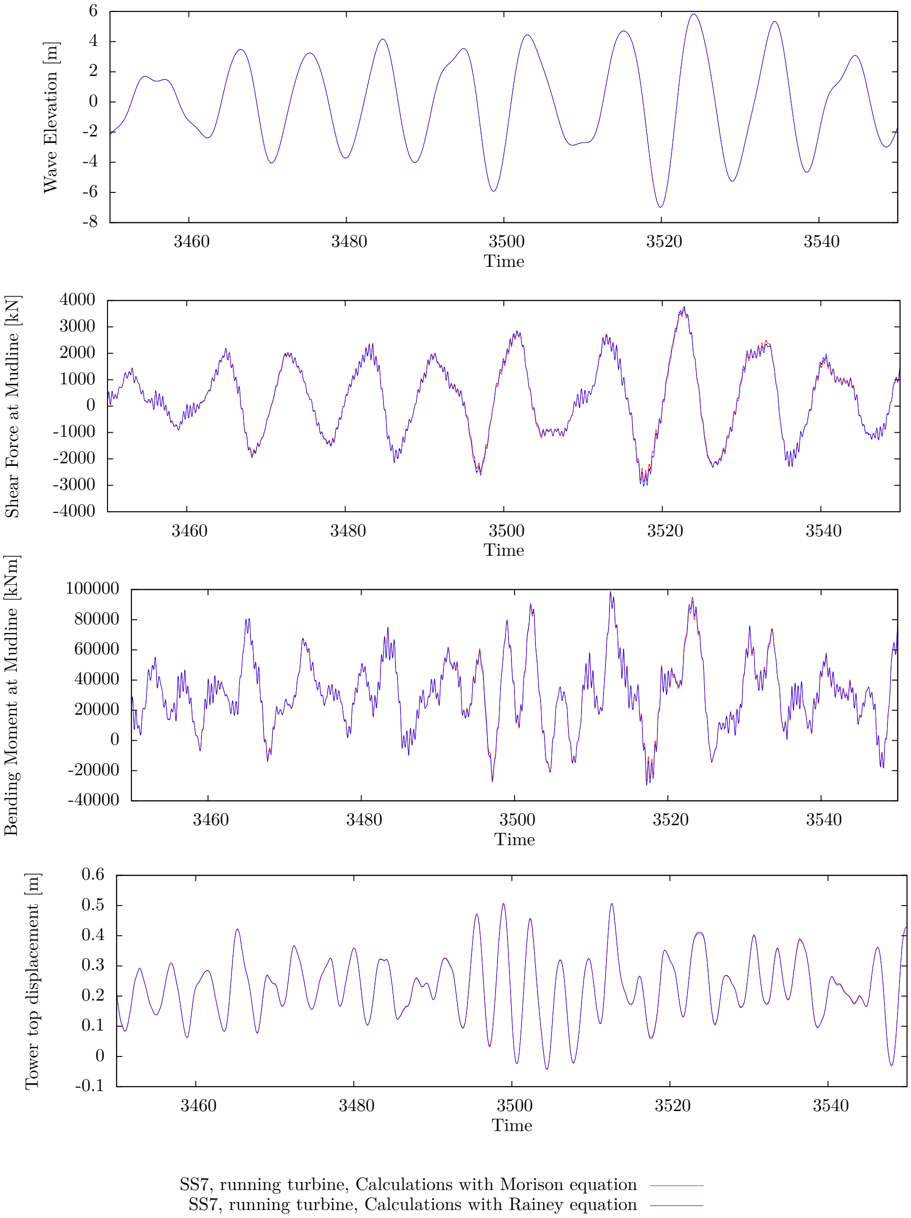

Figure 10.14: Time evolution of the wave elevation, shear force, bending moment and tower top displacement around the event at 3500 [s] in SS 7.

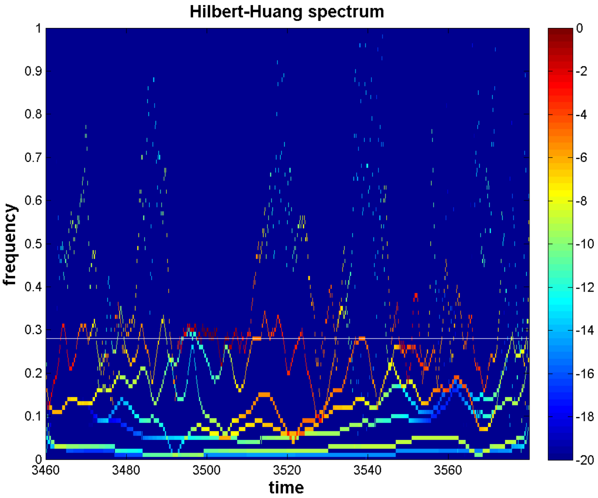

Figure 10.15: Hilbert-Huang-spectrum for the tower top deflection, for a transient resonant oscillation event around 3500 [s] in SS 7 with a running turbine, and forces by Rainey.

SS 6, where only a very small difference occurred. This indicates that for this case, the wave loading is actually important, but the structure will experience resonant oscillations by account of the wind. From the time series it is difficult to see if resonant oscillations also occur for the case where the lower wind has been used. In order to investigate this, the HHS has also been create for this case and is presented in figure 10.17.

It can be observed that much of the resonant oscillations has been removed, and again pointing to the cause of the oscillations being strong winds.

To summarise this section: It has been shown clear springing response in the tower for the special case when the rotor has been parked. By increasing the damping, significant reduction in the amplitude of the oscillations has been found, but the resonant behaviour still remains. It is believed that the cause for the resonant oscillations is the lack of aero-elastic damping from the turbine.

It has then been shown that transient resonant oscillations can occur in this structure, and is believed to be by strong winds. Both in SS 6 and SS 7 transient resonant oscillations has been observed, and in both cases it has been found that they are mainly caused by strong incident winds, and disappeared if lower incident winds was used. For the case of SS 7 the incident waves were found to affect the

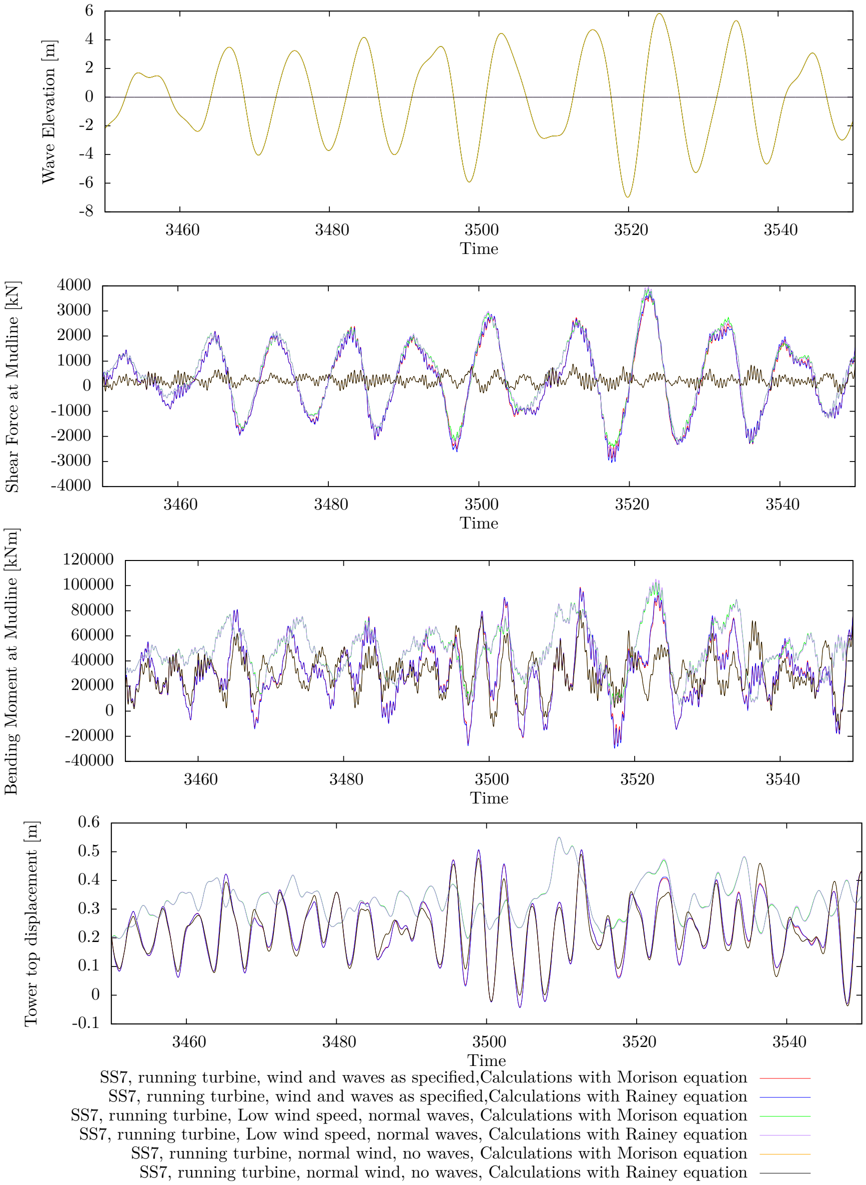

Figure 10.16: Time evolution of the wave elevation, shear force, bending moment and tower top displacement around the event at 3500 [s] in SS 7,with and without a lower wind speed and with or without incident waves.

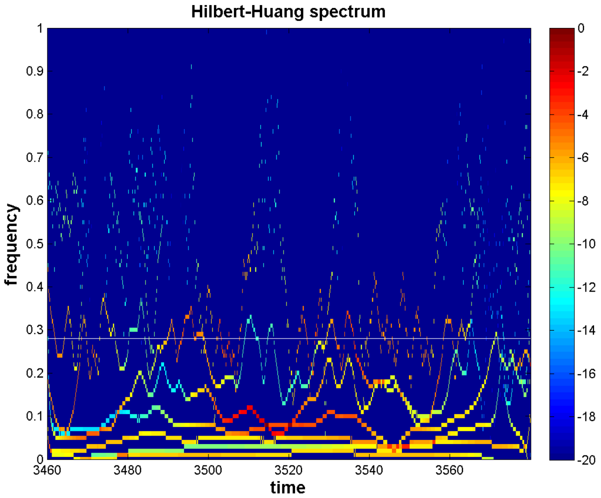

Figure 10.17: Hilbert-Huang-spectrum for the tower top deflection, for a transient resonant oscillation event around 3500 [s] in SS 7 with a running turbine, reduced wind speed, and forces by Rainey.

amplitude of the oscillations, but that the resonant motion still occurred when no waves were present. The phenomenon observed will not be called ringing, because it is not caused by the waves.

It appears that there might exist a coupling between the strong winds, the control system and the wave loads that might govern resonant oscillations in the tower. It has been shown that the wave loads can have an influence on these resonant oscillations. It is therefore a reason to believe that if a steep wave interact with the structure at the same time that the strong winds and the control system creates a resonant motion, large resonant oscillations can occur.

It is important to note that this is not a definite proof of the existence of such a coupling between strong winds, the control system and an eventual wave loading. It is a mere indication of such a relation, and without deeper knowledge about the control system, the question of possible resonant oscillations can not be answered. It is outside the scope of this thesis to investigate these eventual couplings between the control system, strong winds and wave loads.

10.2 Fully Nonlinear Waves

Due to the findings in linear waves, it has been decided to slightly change the point of study. Focus will be put mostly on resonant oscillations in a turbine in the parked condition in SS 6 and SS 7. For a running turbine, only SS 6 and SS 7 will be studied, with input parameters as specified in table 10.1.

The fully nonlinear wave model also produces a linear time series, which can be used to compare linear and fully nonlinear waves. In conversation with one of the creators of the waves model, it has been stated that the incident wave kinematics for the linear solution, is obtained with a vertical stretching. This stretching technique employs the values for the quantities at $z = 0$ for all values above $z = 0$. Forces calculated by this method will then naturally be slightly larger than the forces obtained with wheeler stretching in the last section. Care should be taken when comparing linear results from this section, with the linear results from the last section, as they have been calculated with slightly different wave models.

10.2.1 Quantitative Differences Between Wave Models and Load Models

The first point of interest is to study the PSD of the simulations, as these describe the simulation as a whole. For each sea state, the PSD has been calculated for the same quantities as for linear waves. The cases studied are the fully nonlinear incident waves with forces by Morison, fully nonlinear incident wave with forces by Rainey and lastly linear incident waves with forces by Morison. By investigating these it should be possible to answer the question regarding the effect of nonlinearities in the incident waves. For both sea states the mean wind speed used is the same as stated in table 10.1.

For the force it can be seen differences between the three simulations for both sea states. The differences appear to be bigger between a fully nonlinear and a linear load, than between the load formulations. An interesting feature is that in some areas the PSD from the Morison formulation is actually larger than for Rainey's forces.

The bending moment shows, as expected from the linear simulations, less differences and thus less dependence on the wave loading. Some differences are actually observable also for the bending moment. This is a clear difference from the case of linear waves, where no differences where observable for the bending moment.

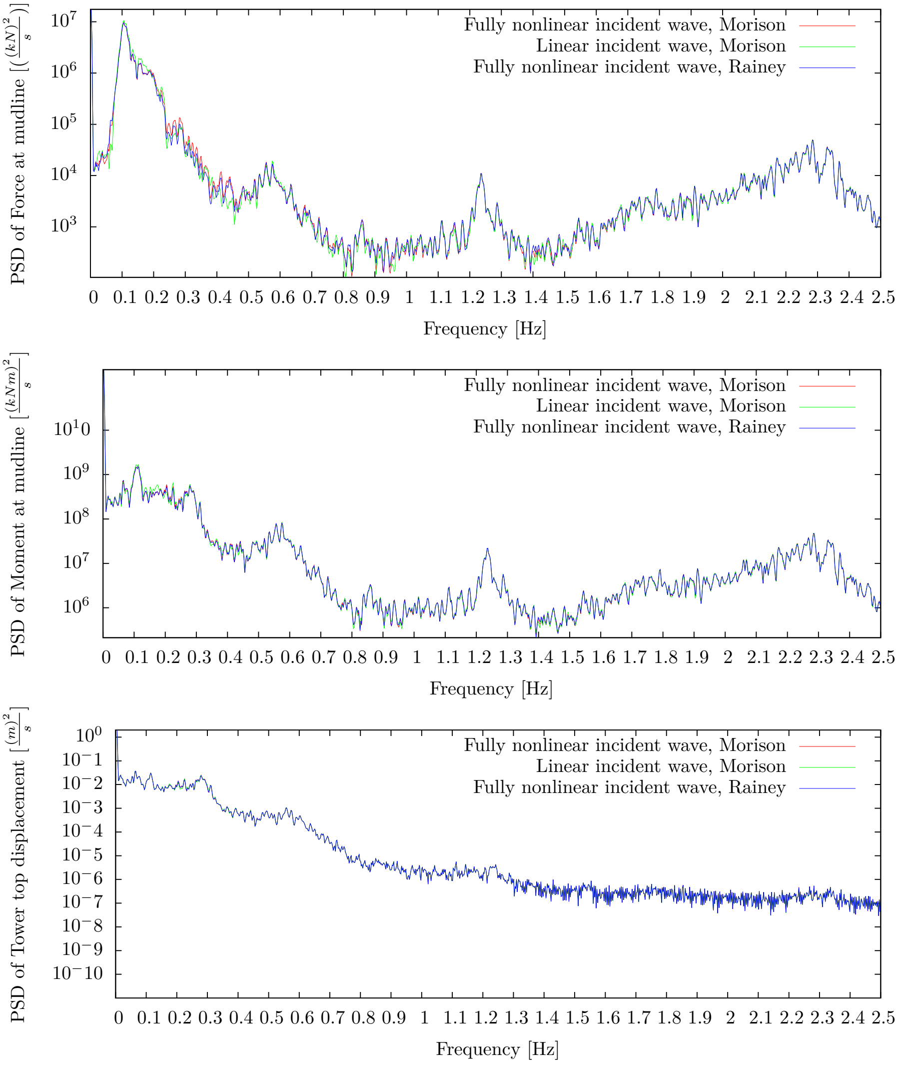

Figure 10.18: Comparison of the power spectral density for the shear force, bending moment and tower top deflection, for the SS 6.

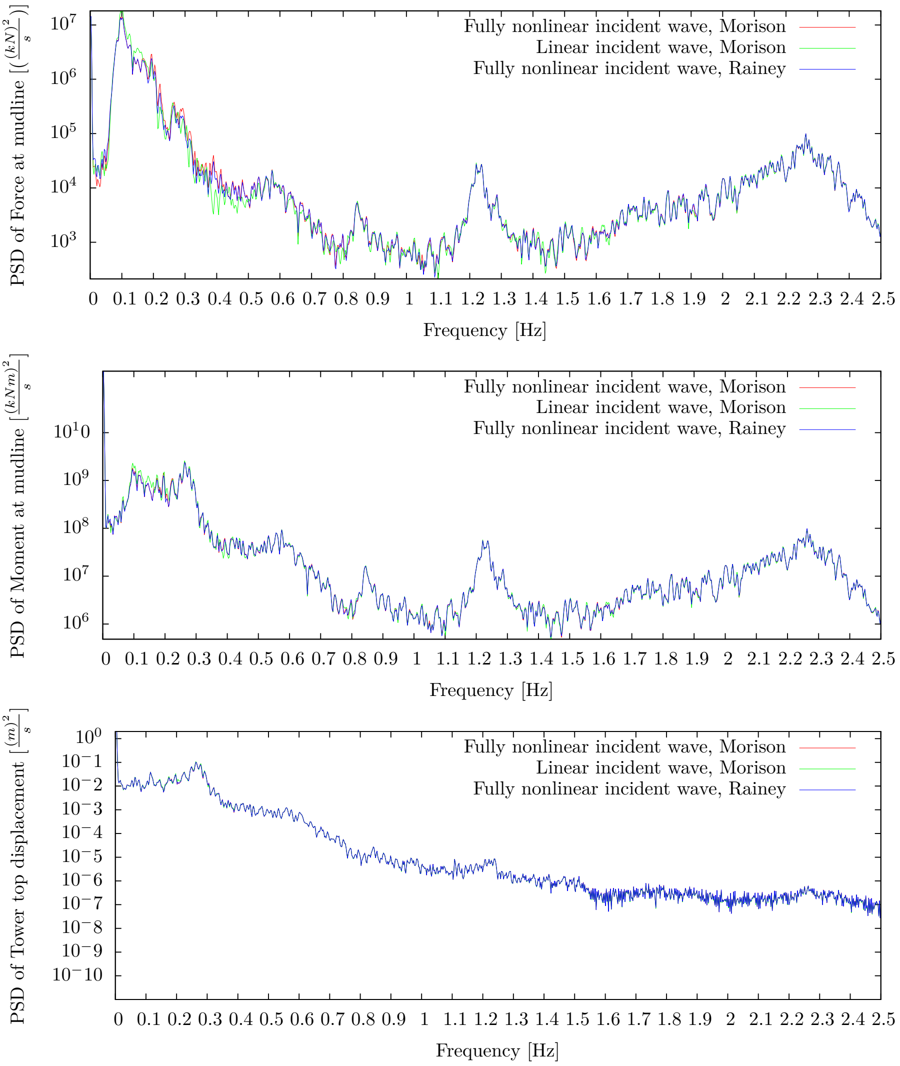

Figure 10.19: Comparison of the power spectral density for the shear force, bending moment and tower top deflection, for the SS 7.

The PSD of the tower top deflection shows some, but very small differences.

On a total basis small differences between the linear and nonlinear incident waves are seen. There is however expected to be seen significant differences in the loading if one investigates the steepest waves. Figures 10.20 and 10.21 show examples from the simulations where a steep wave interacts with the structure.

Investigating the shear force, important differences appear for the three different cases. There are also differences at the bending moment and the tower top deflection. The biggest differences occur when comparing fully nonlinear and the linear incident waves. Here the differences appear when there is a large difference in the free surface wave elevation for the two wave models. There appears to be only small differences between the load formulation for the case of fully nonlinear waves.

No definite rule can be given on the differences between the two load models. For some time instances Rainey's expressions produce the largest loads and larger motions in the tower top, and at another time Morison produces the largest loads. The difference is however smaller than the difference between the incident wave model. This is in line with the results obtained in chapter 9 where it also was found that the nonlinearities in the incident waves where more important than the nonlinearities from the load formulation.

The wave at 920 [s] in SS 7 is $\approx$ 6 [m], and should be an excellent candidate for producing ringing; it is steep, tall and seems very different from the linear solution. However no ringing occurs, and there are no signs of the secondary load cycle. This is an indication that the wave load model, and the force load model, are not able to produce all aspects of this feature.

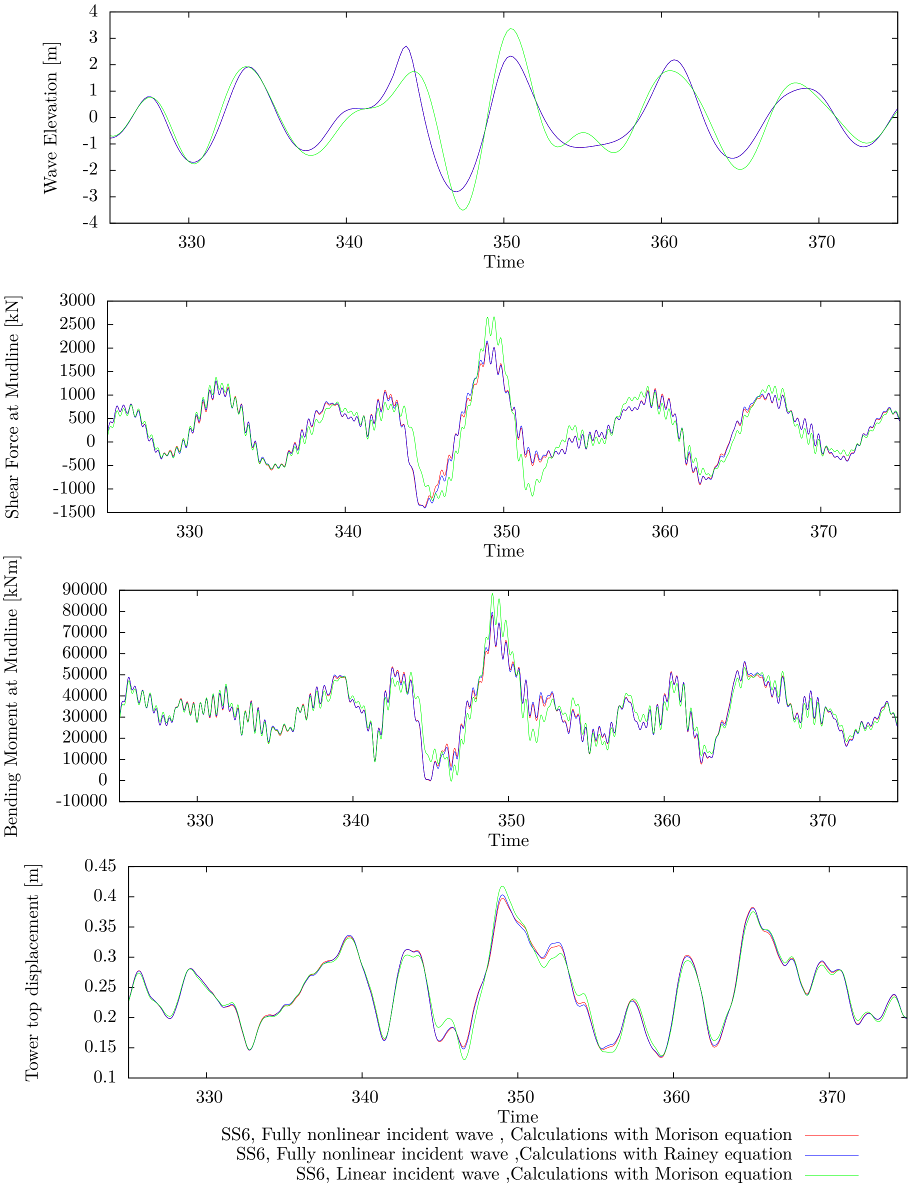

Figure 10.20: Comparison of relevant quantities around large wave event in SS 6.

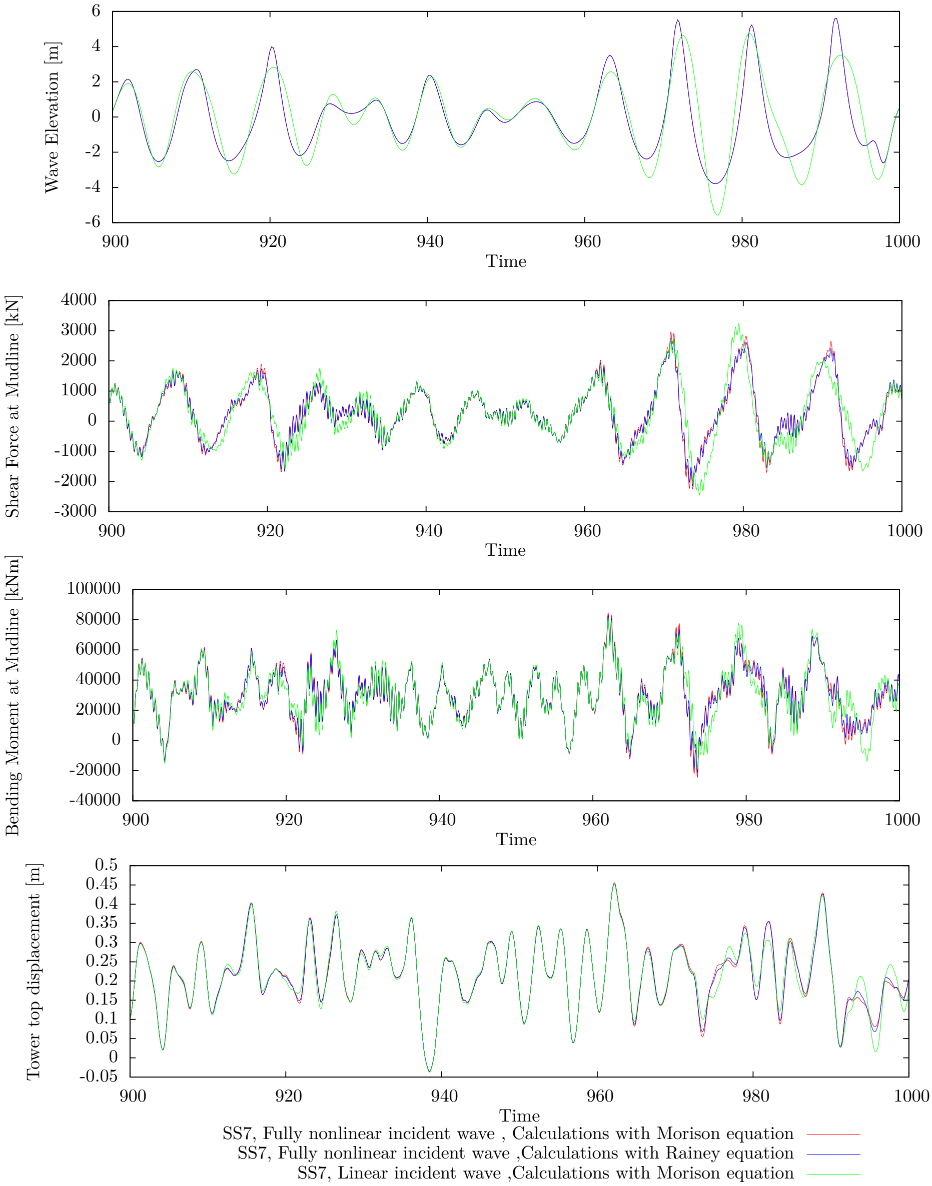

Figure 10.21: Comparison of relevant quantities around large wave event in SS 7.

10.2.2 Resonant Phenomena

The behaviour with slight bursts of resonant behaviour in strong wind was also encountered for the simulations with fully nonlinear waves. As for linear waves the resonant oscillations disappeared when the incident wind speed was reduced. This topic will not be covered here, due to the belief that it is related to some kind of coupling between strong winds and the control system.

Simulations were also performed with the reduced wind speed for the two cases, but no clear signs of ringing was shown. This does not mean that it cannot happen in a running wind turbine, but that it has not been encountered in these simulations. However, due to the strong aero-elastic damping, it is believed to be a rare event.

In the linear analyses, clear springing was observed when the turbine was set in the parked condition. The same is also observed here with fully nonlinear waves.

Figure 10.22 shows simulations in SS 6 with a parked turbine. Several surprising results are present here, especially that the amplitude of the oscillations in the tower is larger when forces are calculated by Morison, than with Rainey. For linear waves in SS 5, the amplitude of the oscillations of the two load models were similar, which is clearly different from the results obtained here with fully nonlinear waves.

One possible solution is that Rainey's expressions, which contains additional terms (the axial divergence term, and the free surface intersection force), which are dependent on the relative velocity between the structure and the incident water particles. The force component in these forces that is dependent on the structural velocity will then be additional hydrodynamic damping terms, which Morison's equation does not have.

With the nonlinear Fenton waves in section 9 it was shown that the difference between the two load models are in the higher harmonic terms. The second harmonic load was generally overpredicted by both Rainey and Morison, with Rainey generally predicting higher loads. The third harmonic term provided very good agreement with Rainey's expressions while Morison's equation slightly underpredicted the differences. For the linear waves almost no third harmonic load was present for either of the load models. It is possible that the differences seen here between results from both the load models, and also the wave models are due to the differences in these terms.

However, as can bee seen by the comparisons of the two load models, for instance in figure 9.15, the difference between them for the second harmonic load is approximately the same for both linear incident waves and nonlinear waves. This

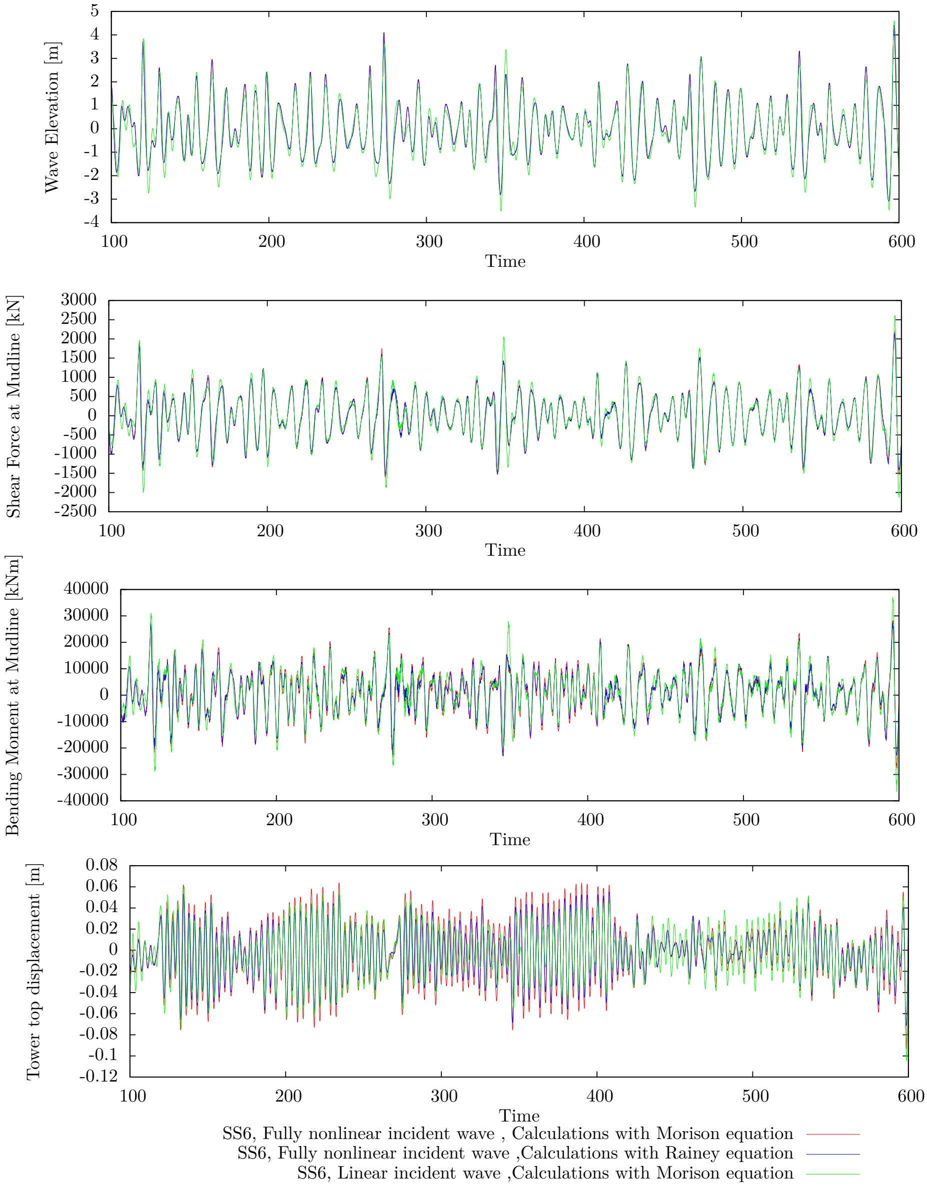

Figure 10.22: Comparison between Wave elevation, shear force, bending moment and tower top deflection for springing in SS 6 with a parked turbine.

means that the different behaviour of the load models in linear and nonlinear waves, should not be caused by the second harmonic load. This means that the difference observed in the amplitude for the resonant oscillations are due to the difference in the third harmonic load. Since Rainey predicted the third harmonic forces with better experimental comparison, it is believed that results obtained by the new load formulation is the closest to the real solution.

Another noteworthy observation is that for parts of the time series, there are actually observed larger oscillations of the tower top when the forces are calculated by linear waves than with fully nonlinear waves.

The time series also show some instances where the amplitude of oscillation increases with a burst like behaviour, from one oscillation to the next. This behaviour is seen, in for instance SS 7, presented in figure 10.23. It can be seen that the amplitude of the oscillations is near doubling in relation to the steep incident wave.

This behaviour occurs for several time instances, and is the closest thing to a ringing response seen in the simulations. It seems to be the same response also from the linear wave with Morison loading. The response is not very similar to the classical ringing case, but it definitely have a burst like appearance.

Regarding the frequency content, a HHS has been made for the three time instances in question and presented in figs. 10.24 to 10.26.

All three figures show a clear transition where the resonant oscillations becomes more intense at a specific point in time. The simulations with a fully nonlinear incident wave, and forces by Rainey shows perhaps the most clear transition, where one IMF dominates before the burst, when suddenly another IMF starts to oscillate with the resonant frequency. For the other two it is the same IMF that already oscillates with the resonant frequency, but then the intensity is suddenly increased. The IMF of the three cases are presented in figs. 10.27 to 10.29.

From the IMFs it is clear that the case where the forces are calculated by Rainey's expression, there is a sudden transition to the oscillations in the second mode function. At the same time instance there is an reduction in amplitude of the third mode function. For the two cases with Morison's equation there is merely a amplitude increase of the second modefunction. The case with nonlinear waves shows a much faster increase in the amplitude of the modefunction, than the case with linear waves. However, the IMFs are notoriously difficult to interpret, and in order for them to be valid, they need to be close to orthogonal. The orthogonality index for the calculations with Rainey has been calculated to 0.067 and for the calculations with fully nonlinear waves and Morison's equation 0.023. According to Huang et al. (1998), if the decomposition is orthogonal then the

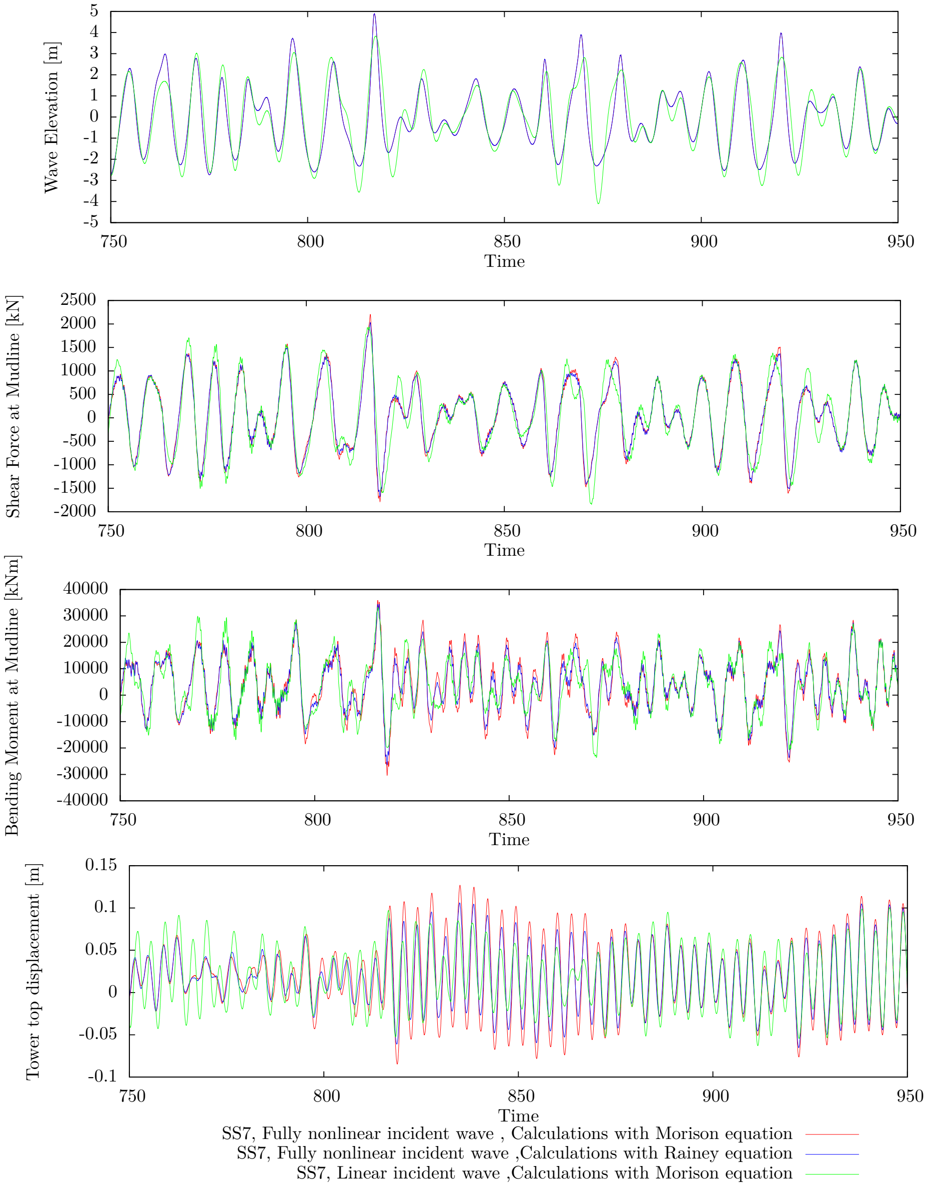

Figure 10.23: Comparison between Wave elevation, shear force, bending moment and tower top deflection for springing in SS 7 with a parked turbine.

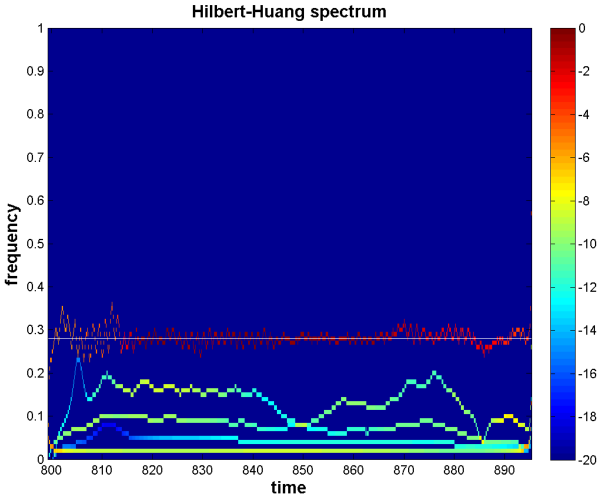

Figure 10.24: Hilbert-Huang-spectrum for the tower top deflection, for a transient resonant oscillation event around 800 [s] in SS 7 with fully nonlinear incident waves, a parked turbine, and forces by Morison.

orthogonality index should be zero. There is thus some signs that the resonant oscillations predicted by the different load models have slightly different origin, but the data are not conclusive.

By investigating the load history there does not seem to be a marked secondary load cycle after the main load. This is the second instance with a steep fully nonlinear waves without seeing the secondary load cycle. It appears then that the secondary load cycle may not be caused solely by higher order forces. This is an indication that the next step in the problem should be to include the wave-structure interactions, to try and predict hydraulic jumps travelling around the structure. Another possibility is the inclusion of some kind of impact force.

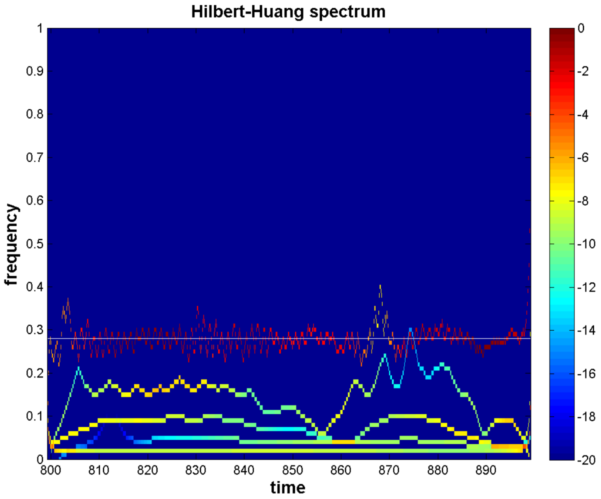

Figure 10.25: Hilbert-Huang-spectrum for the tower top deflection, for a transient resonant oscillation event around 3500 [s] in SS 7 with linear incident waves, a parked turbine, and forces by Moriso.n

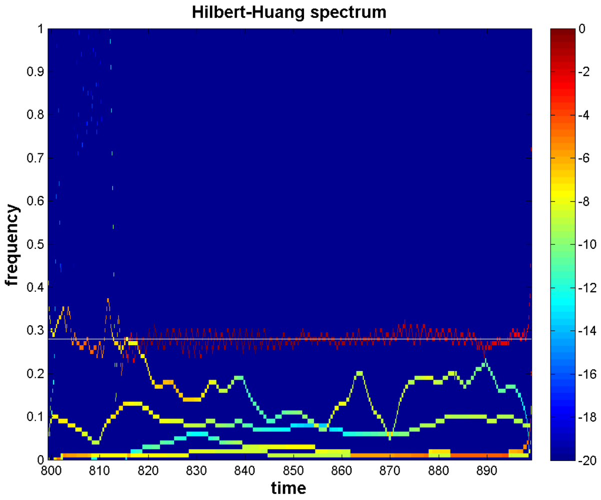

Figure 10.26: Hilbert-Huang-spectrum for the tower top deflection, for a transient resonant oscillation event around 3500 [s] in SS 7 with fully nonlinear incident waves, a parked turbine, and forces by Rainey.

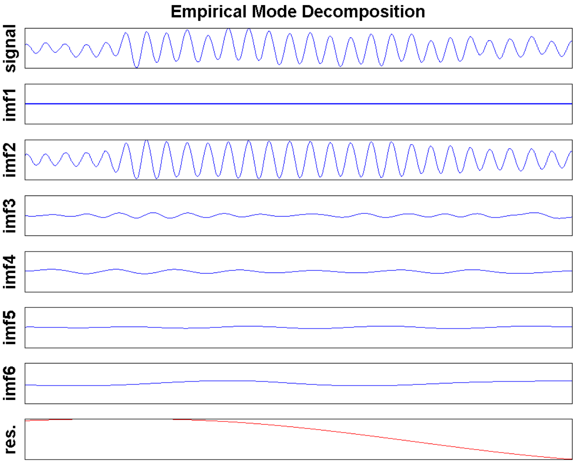

Figure 10.27: IMFs used to produce the HHS for the calculations with Morison's equation and fully nonlinear waves.

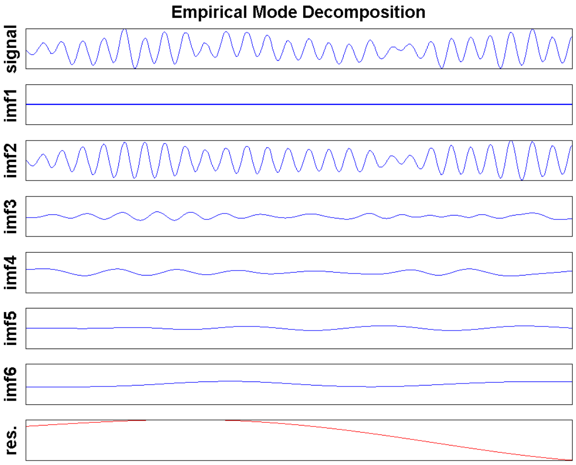

Figure 10.28: IMFs used to produce the HHS for the calculations with Morison's equation and linear waves.

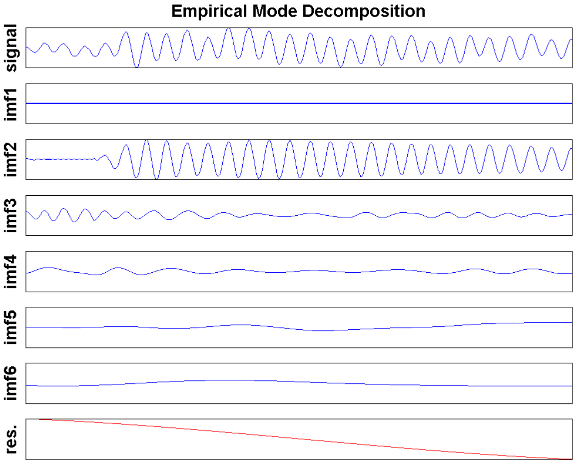

Figure 10.29: IMFs used to produce the HHS for the calculations with Rainey's expression and fully nonlinear waves.

10.3 Summary of Findings

In this chapter it has been found that for a bottom fixed wind turbine with a working rotor, the hydrodynamic loads are not as important as the aerodynamic loads for the motion of the tower top. The bending moment at the mudline is also governed by the aerodynamic loads, due to the long arm the aerodynamic loads have to the seabed.

For the shear force/horizontal force at the mudline, the wave loads are actually dominating. This has been seen by the fact that when calculations are performed with reduced wind speed, this has a very little effect on the horizontal force.

For the case of linear incident waves, the effect of a different load model has virtually no effect on the motions of the tower top, and only a slight affect on the shear force.

The difference between the load models are larger for the fully nonlinear waves, where the different load formulations actually have a small difference on the tower top deflection. Still the largest differences are seen in the horizontal force. The differences observed are still quite small compared to the maximum of the different quantities.

The difference between using a fully nonlinear and a linear incident wave model are actually larger than the differences between the load models, indicating that it is more important to satisfy the incident waves properly.

Transient resonant oscillations have been found in SS 6 and SS 7. However by comparing with simulations without waves the oscillations are still present, and only disappear if the wind speed is reduced. The oscillations then seems to be caused by strong winds and the way the control system tries to keep the rotor speed under control. In SS 7 it was found that the incident waves had an important effect on the amplitude of the resonant oscillations, leading to the belief that there might be a coupling between the strong winds, the control system, wave loads and resonant oscillations.

In a parked condition, severe springing is observed in the tower. This phenomenon occurs for all combinations of wave models and load models. Investigation has led to the belief that the system is lacking damping when the rotor is parked, and that the aero-elastic damping is inhibiting this motion in a running turbine. The resonant oscillations are more or less present throughout the whole simulations, but it will sometimes have a burst-like increase in amplitude. This is close to a ringing effect, and it is believed that if the structure had not already been in resonant oscillations, this could be an instance of ringing.

When the tower undergoes springing, important differences have been found for the amplitude of the tower top deflection, between the load formulations and also between the incident waves for this condition. An effort has been made, in section 10.2.2, to try and argue that the difference in amplitude is caused by third harmonic forces. This indicates that when the rotor is parked, it is important to both have an accurate wave model and also an accurate load model.

The burst-like increase in the amplitude has been found for all combinations of wave and load models.

For a running turbine, no clear ringing incidents have been observed, even for the case with fully nonlinear waves.

For steep waves, the secondary load cycle mentioned as a possible cause for ringing has not been observed, which leads to the belief that a more sophisticated model may be needed.

11 | Conclusion

In this thesis a general review of bottom fixed wind turbines has been performed, with the focus on nonlinear wave loads and the structural effects of ringing and springing. By comparing to previous research on the cause of ringing , it was found that a bottom fixed wind turbine with a monopile foundation might experience ringing. By investigating the natural frequency of the tower, it was concluded that springing might also be a problem for the structure.

In order to investigate nonlinear effects, an improved load model derived by Rainey has been implemented into FAST. Comparison between the loads calculated by the existing feature of Morison's equation, and loads calculated by Rainey's expressions has been performed. Further, comparison has been made with experiments on a cylinder in regular waves and for fully coupled calculations.

From the comparison with experiments and nonlinear Fenton waves, it was observed that Rainey's expressions provided better agreement with the experimental values than Morison's equation for the third harmonic force. When using linear incident waves and Wheeler stretching, the third harmonic loads are seriously underpredicted.

A clear overprediction was present in the second harmonic load with both Morison and Rainey when Fenton generated incident waves was used. The error increases with increasing kr values, as expected since the theory is a slender body theory. The error appears to be growing with a close to linear or weakly exponential dependence on kr. With linear incident waves there was a fairly good agreement between experiments and Rainey's expressions, while Morison's equation seems to slightly underpredict.

The first harmonic load is slightly underpredicted by both load models, regardless of the incident wave model.

The comparison has shown that for a general load calculation, it might be beneficial to use Rainey's slender body expressions over Morison's equation, since it will in general have better agreement with experimental values. However, the difference between the two load formulation for the third harmonic load was smaller than the third harmonic load produced by Morison's equation and Fenton generated waves. This has lead to the conclusion that the nonlinearities in the incident waves are more important than the nonlinearities that originate in the load formulation.

The reference turbine has been subjected to fully coupled aero-hydro-servo-elastic simulations, in both linear irregular sea, and fully nonlinear sea. The shear force at the mudline, the bending moment at the mudline and the tower top deflection have been studied. It was found that the shear force is dominated by the wave loads, but that the two others are dominated by aerodynamic loads. Investigations into the subject has revealed that the aero-elastic effects are dominating the structural motions. This has been contributed to the long distance between the mudline and the tower top, giving the aerodynamic forces a long arm.

For linear waves, there are generally small differences between the load models, for the three quantities studied.

For the fully nonlinear incident waves, larger differences between the load models were found, but not as large as the differences between simulations with a fully nonlinear and a linear incident wave. Hence, for a running turbine it can also be concluded that the nonlinearities in the incident waves are dominating over nonlinearities from the load formulation.

Some transient resonant oscillations were found in simulations with strong winds. By investigation it was found that they are not caused by the waves, as they still occurred when no incident waves were present. It was however found that the waves might affect the amplitude of the oscillations. The resonant oscillations disappeared when a lower incident wind speed was used. It is thus believed that these oscillations are caused by the winds being much stronger than the rated maximum wind speed. This might introduce some kind of coupling between the control system, the wind loads and the wave loads.

The fact that there is little difference between the two load models is only valid for the case of a running turbine. If the rotor is parked, so that there is little aerodynamic forces acting on the structure, larger differences between the two load models are found, both by studying the time series and the power spectral density.

In the simulations with a parked turbine, severe springing occurred. This has been found in SS 5 for the case of linear waves, but it is believed to be present also for smaller and larger sea states. The steady state resonant oscillations are contributed to the lack of aero-elastic damping which is present when the turbine is running. This allows what is believed to be the higher order wave loads to excite the tower at it's first natural frequency.

SS 6 and SS 7 have been investigated with fully nonlinear incident waves for the parked rotor. The simulations show significant springing, and it occurs for all load and wave models. However the amplitude of the tower top deflection shows considerable differences between both the different load models and also between a linear incident wave and a fully nonlinear waves. This means that for the case of a parked wind turbine it is important to model both forces and incident waves accurately.

The springing appears to have a burst-like increase in amplitude when interacting with steep waves. This behaviour is the closest observed to the classical time evolution of ringing. It occurs for all different models, but appears to be largest for the fully nonlinear wave model.

The fact that springing occurs is a sign that parking the rotor when bad weather is encountered, might actually be dangerous from a fatigue point of view. The rotor should ideally be able to rotate and thereby alter the characteristics of the oscillations.

No ringing or springing occurred in the simulations with a running turbine.

Regarding ringing, the secondary load cycle which is believed to be important, was not observed, even for steep fully nonlinear waves. This indicates that a wave load model that includes the heavy wave-structure interaction might be necessary.

Considering the questions stated in the outline of the thesis:

- Yes, there exist important differences between a linear incident wave model and a fully nonlinear wave model. The differences are small for a running turbine, but could have an affect on the whole life cycle of the turbine. Much larger differences are present in a turbine with a parked rotor, and here the chosen wave model has an impact on the maximum tower top deflection.

- Differences are present for the two different load models. Considering the linear incident waves, the effect is small, even for the horizontal force which is governed by the wave loads. Larger differences are present for the non-linear incident waves. The largest differences are found when the turbine is parked, where the chosen load model affects the amplitude of resonant oscillations.

- For a running turbine in normal conditions, the nonlinear effects have small significance for the operation of the turbine. This is because the motion of the tower top and the bending moment at the seabed are governed by the aerodynamic loads. It is however important to note that if bad weather is encountered it might actually be more dangerous to park the rotor than to let the rotor have some freedom to absorb forces. In a parked condition, the nonlinear effects have been shown to be important.
- The structure can experience springing, and a behaviour close to ringing when put in a parked condition. No transient behaviour caused solely by wave loads is observed in simulations with a running turbine. This does not prove that ringing cannot occur, since it is not certain that all aspects of the phenomenon are included in the calculations.

12 | Further Work

The two different load models have been compared with experimental results solely with respect to the amplitude of the load components. Also the phase of the load in relation to the incident wave should be studied, as it might be important for the onset of resonant oscillations.

More work should be put in studying the effect of the differences between the load models when a fully nonlinear incident wave is used. The work should focus on the long term effects of using different formulations. Some differences in terms of the power spectral density and the time evolution was found here, but this study cannot be said to be complete.

The reference turbine experiences heavy springing when set in the parked condition. Only a few cases have been studied here, so more time should be spend on investigating this effect. The finding, that with fully nonlinear waves Rainey predicted smaller amplitude of the springing than Morison while with linear incident waves no difference was present for the amplitude, needs further investigation. Further work on the topic should preferably be compared with experiments trying to reproduce the springing observed in the simulations.

Increasing the structural damping showed a clear reduction in the amplitude of the resonant oscillations. Further work on the subject should, if possible, include a more realistic boundary condition at the seabed, in order to be certain that the damping in the system is correct. The total damping of the structure when the rotor is parked is believed to be very important for the effect that the nonlinear loads have on the structure.

The possible coupling between strong winds, wave loading and the effect of the control system seems to be able to create transient resonant oscillations. This feature might have a significant role on the life span of an offshore wind turbine and needs further investigation. It is believed that the resonant motion is caused by the control system trying to reduce the loads on the turbine to decrease the rotor speed. This would introduce an important possibility for coupling between the control system and wave loads. Further work on the topic of resonant oscillations caused by waves should include a detailed study of how the control system operates and the possible coupling with wave loads.

References

Chaplin, J.R.; Rainey, R.C.T., and Yemm, R.W. Ringing of a vertical cylinder in waves. *Journal of Fluid Mechanics*, 350, 1997.

Cordle, A. and Jonkman, Jason M. State of the Art in Floating Wind Turbine Design Tools. In *Proceedings of the 21st International Offshore and Polar Engineering Conference* , 2011.

Dean, Robert G. and Dalrymple, Robert A. *Water Wave Mechanics for Engineers and Scientists.* Prentice-Hall Inc., 1984.

Emmerhoff, Ole Johannes. *The slow drift Motions of Offshore Structures.* PhD thesis, Massachusetts Institute of Technology, 1994.

Faltinsen, O.M. *Sea Loads on Ships and Offshore Structures.* Cambridge, 1990.

Faltinsen, O.M.; Newman, J.N., and Vinje, T. Nonlinear Wave loads on a slender vertical cylinder. *Journal of Fluid Mechanics*, 289:179–198, 1995.

Fenton, J.D. The numerical solution of steady water wave problems . *Computers & Geosciences*, 14(3):357–368, 1988.

Fenton, John D. Use of the program Fourier for steady waves, 2012.

Greco, Marilena. Lecture Notes TMR4215:Sea Loads, 2011.

Grue, John. On Four highly nonlinear phenomena in wave theory and marine hydrodynamics. *Applied Ocean Research*, 24:264–274, 2002.

Grue, John and Huseby, Morten. Higher-Harmonic wave forces and ringing of vertical cylinders. *Applied Ocean Research*, 24:203–214, 2002.

Gudmestad, Ove T. and Connor, Jerome J. Linearization methods and the influence of current on the nonlinear hydrodynamic drag force. *Applied Ocean Research*, 52:184–194, 1983.

Hogben, N.; Olliver, G.F., and Dacunha, N.M.C. *Global Wave Statistics*. Published for British Maritime Technology, 1986.

Huang, Norden E.; Shen, Zheng; Long, Steven R.; Wu, Manli C.; Shih, Hsing H.; Zheng, Quanan; Yen, Nai-Chyuan; Tung, Chi Chao, and Liu, Henry H. The empirical mode decomposition and the Hilber spectrum for nonlinear and non-stationary time series analysis. *Proc. R. Soc. Lond. A*, 1998.

Huseby, Morten. *Experiments on ringing loads and higher harmonic wave forces*. PhD thesis, University of Oslo, 2000.

Huseby, Morten and Grue, John. An experimental investigation of higher-harmonic wave forces on a vertical cylinder. *Journal of Fluid Mechanics*, 414: 75–103, 2000.

Iwanowski, Bogdan; Astrup, Søren; Lefranc, Marc, and Hansson, Rolf. Identification of Ringing Events for a Slender Tubular Marine Structure. In *Proceedings of the ASME 30th International Conference on Ocean, Offshore and Arctic Engineering*, 2011.

Jefferys, E.R. and Rainey, R.C.T. Slender Body Models of TLP and GBS 'Ringing'. In *BOSS '94 - Behaviour of Offshores structures '94*, 1994.

Jonkman, J.; Butterfield, S.; Musial, W., and Scott, G. Definition of a 5-MW reference Wind Turbine for Offshore System Development. Technical report, NREL, 2009.

Jonkman, Jason M. *Dynamics Modeling and Loads Analysis of an Offshore Floating WInd Turbine*. PhD thesis, University of Colorado, 2007.

Jonkman, Jason M. and Buhl, Marshall L. FAST User's Guide. Technical report, NREL, 2005.

Jonkman, Jason M. and Musial, Walt. Final Report Subtask 2 - IEA Wind Task 23. Technical report, IEA Wind, 2010.

Kelley, N.D. and Jonkman, B.J. Overview of the TurbSim Stochastic Inflow Turbulence Simulator. Technical report, NREL, 2007.

Langen, Ivar and Sigbjørnsson, Ragnar. *Dynamisk Analyse av Konstruksjoner*. NTNU, 2011.

Lighthill, James. Waves and hydrodynamic loading. In *Proc. 2nd Intl Conf. on the Behaviour of Offshore Structures*, 1979.

Longuet-Higgins, M.S. and Cokelet, E.D. The Deformation of steep surface waves on water I. A numerical method of computation. *Proc. R. Soc. Lond. A*, 1976.

Malenica, S. and Molin, B. Third-harmonic wave diffraction by a vertical cylinder. *Journal of Fluid Mechanics*, 302:203–229, 1995.

Manners, W. and Rainey, R.C.T. Hydrodynamic Forces on Fixed Submerged Cylinders. *Proc. R. Soc. Lond. A*, 436:13–32, 1992.

Marino, Enzo. *An Integrated nonlinear wind-waces model for offshore wind turbines*. PhD thesis, University of Florence, 2011.

Marino, Enzo; Borri, Claudio, and Peil, Udo. A fully nonlinear wave model to account for breaking wave impact loads on offshore wind turbines. *Journal of Wind Engineering and Industrial Aerodynamics*, 99, 2011.

Marino, Enzo; Lugni, Claudio, and Borri, Claudio. A novel numerical strategy for the simulation of irregular nonlinear waves and their effects on the dynamic response of offshore wind turbines. *Computer Methods in applied mechanics and engineering*, 2013.

Moriarty, Patrick J. and Hansen, A. Craig. AeroDyn Theory Manual. Technical report, NREL, 2004.

Myrhaug, Dag. Lecture Notes TMR4180 - Marin Dynamikk, 2007.

Nakayama, Tsukasa. A computational method for simulating transient motions of an incompressible inviscid fluid with a free surface. *International Journal For numerical Methods in Fluids*, 10, 1990.

Newman, J.N. *Marine Hydrodynamics*. MIT Press, 1977.

Newman, J.N. Nonlinear scattering of long waves. In *Waves and Nonlinear Processes in Hydrodynamics*, 1996.

Rainey, R.C.T. A new equation for calculating wave loads on offshore structures. *Journal of Fluid Mechanics*, 204:295–324, 1989.

Rainey, R.C.T. Slender-Body Expressions for the Wave Load on Offshore Structures. *Proc. R. Soc. Lond. A*, 450(1939):391–416, 1995a.

Rainey, R.C.T. The Hydrodynamic load at the intersection of a Cylinder with the water surface. In *Proceedings of the 10th International Workshop on Water Waves and Floating Bodies*, 1995b.

Rainey, R.C.T. Weak or Strong nonlinearity: The vital Issue. *Journal of Engineering Math*, 58:229–249, 2007.

Rilling, G.; Flandrin, P., and Gonçalves, P. On empirical mode decomposition and its algorithms. In *Proceedings of IEEE-EURASIP Workshop on Nonlinear Signal and Image Processing NSIP-03*, Grado (Italy), June 2003. URL `http://perso.ens-lyon.fr/paulo.goncalves/pub/NSIP03_GRPFPG.pdf`.

Rottmann, Karl. *Matematisk Formelsamling*. Spektrum Forlag, 2008.

Sclavounos, Paul; Tracy, Christopher, and Lee, Sungho. Floating Offfshore Wind Turbines: Responces in a Seastate Pareto Optimal Designs And Economic Assessment, 2007.

Stansberg, Carl Trygce and Gudmestad, Ove T. Non-Linear Random Wave Kinematics Models Verified Against Measurments in Steep Waves. In *Proceedings of the 15th International Conference on Offshore Mechanics and Arctic Engineering - Volume 1 -Part 1*, 1996.

Stansberg, Carl Trygve; Gudmestad, Ove T., and Haver, Sverre K. Kinematics Under Extreme Waves. *Journal of Offshore Mechanics and Arctic Engineering*, 130, 2008.

Taylor, R. Eatock; Rainey, R.C.T., and Dai, F.N. Non-Linear Hydrodynamic analysis of TLP's in extreme Waves: Slender Body and Diffraction Theories Compared. In *Proceedings of the sixth International Conference: Behaviour of offshore structures*, 1992.

Tromans, Peter; Swan, Chris, and Masterton, Stephen. Nonlinear Potential Flow Forcing: The ringing of concrete gravity based structures. Technical report, HSE - Health & Safety Executive, 2006.

Veritas, Det Norske. Recommended Practise DNV-RP-C205 - Enviromental conditions and enviromental Loads. Technical report, Det Norske Veritas, 2010.

Veritas, Det Norske. Design of Offshore Wind Turbine Structures. Technical report, Det Norske Veritas, 2011.

Welch, S.; Levi, C.; Fontaine, E., and Tulin, M.P. Experimental Study of the Ringing Response of a Vertical Cylinder in Breaking Wave Groups. *International Journal of Offshore and Polar Engineering*, 9(4), 1999.

Wheeler, J.D. Method for Calculating Forces Produced by Irregular Waves. *Journal of Petroleum technology*, 22:359–367, 1970.

White, Frank M. *Fluid Mechanics*. McGraw Hill, 6 edition, 2008.

A

A.1 Morison's Equation and Wheeler Stretching

Morison's equation is a semi-empirical load formula divided into two parts. The first part is related to the forces from potential flow, and the second part is an empirical relation which shall take into account the viscous drag forces. The potential flow part of the equation can be derived by assuming a slender structure in linear incident waves, and the details can be found in for instance Faltinsen (1990).

The potential load term is given in equation A.1

$$\mathrm{d}F = \rho\pi\frac{D^2}{4}C_M dz a_x \tag{A.1}$$

Where C_m is the mass coefficient given as $C_m = (1 + C_A)$, C_A is the added mass coefficient and a_x is the acceleration of water particles at the cylinder centre. When the drag part of the equation is included, it reads:

$$\mathrm{d}F = \rho\pi\frac{D^2}{4}(1 + C_A)dz a_x + \frac{\rho}{2}C_D D dz|u|u \tag{A.2}$$

Where C_D is the drag coefficient, and u is the velocity of the water particles at the cylinder centre.

The two coefficients C_A and C_D needs to be decided empirically, and are affected by for instance the Keuligan-Carpenter number and Reynolds number. The drag coefficient is usually highly dependent on the Reynolds number, and according to Veritas (2010) may vary from as low as 0.3 to 1.2. The added mass of a structure is generally frequency dependent, so the added mass coefficient is highly dependent on the Keuligan-Carpenter number. According to Veritas (2010) it may be as low as 0.2 for a rough cylinder to 1.0 for the case of low KC number. The case of $C_A = 1.0$ is the theoretical result, obtained by long wave approximations.

It is possible to expand the equation to take into account the relative motion between the turbine and the water particles. When this is taken into account, it can be written as (Faltinsen, 1990):

$$\mathrm{d}F = \rho\pi\frac{D^2}{4}(1+C_A)dza_x - \rho C_A\pi\frac{D^2}{4}dz\dot{U}_x + \frac{\rho}{2}C_D D dz|u-U_x|(u-U_x) \quad \text{(A.3)}$$

Where u is the horizontal velocity of the water particles, $\dot{U}_x$ is the local structure acceleration in and U_x is the local structure velocity.

It can be shown by writing the drag term as a Fourier series, that the drag term will include odd harmonics ($\omega, 3\omega, 5\omega,...$) and is thereby a source of nonlinear forcing. This could also be seen on the square dependency of the water particle velocity. When current is present it would also give even terms (Gudmestad and Connor, 1983).

By studying the source code of FAST, it appears that this version of Morison's equation has been implemented.

The second term is a coupling between the elasticity of the structure and the hydrodynamic loads. The deformation of the structure caused by the aerodynamic forces will generate forces on the structure from the water by account of this term.

Stretching of the linear wave kinematics seems to be more or less standard procedure, if one is to use what the solvers in Jonkman and Musial (2010) use as standard. For neither of the techniques there seems to be a sound physical reasoning, but they are used as “engineering-approximations”. It appears that a popular stretching technique is Wheeler stretching. Here the wave kinematics are stretched, so that the velocity valid at $z = 0$ according to linear theory is applied at the free surface. This is in reality a shift in the coordinates so that the stretched vertical coordinate z’ is written as:

$$z' = \frac{z-\zeta}{1+\frac{\zeta}{h}} \quad \text{(A.4)}$$

(Stansberg and Gudmestad, 1996).

The method is applied by integrating the sectional force to the instantaneous free surface, but with a substituted coordinate in the “decay-function” for the wave kinematics. Since the integration over the wetted surface is to the time varying free surface elevation, this should give a force proportional to ζ^2, where one order is from the wave kinematics, and the second is from the integration to a moving free surface. More importantly a force proportional to ζ^2 should also give higher harmonic force.

This can be shown by the following. Assume a stiff vertical cylinder in finite water with water depth h. The wave profile of a linear regular incident wave is given as:

$$\zeta = \zeta_a \sin(\omega t - kx) \tag{A.5}$$

The inertia force on a section is then given by Morison's equation:

$$dF = \rho \frac{\pi D^2}{4}(1 + C_A)a_x dz = \rho\pi r^2(1 + C_A)a_x dz \tag{A.6}$$

The acceleration from a regular first order incident wave is given as:

$$a_x = \omega^2 \zeta_A \frac{\cosh(k(z + h))}{\sinh(kh)} \cos(\omega t - kx) \tag{A.7}$$

Placing the origin in the centre of the cylinder with the vertical axis pointing upwards, the force on a section is given as:

$$dF = \rho\pi r^2(1 + C_A)\omega^2 \zeta_A \frac{\cosh(k(z + h))}{\sinh(kh)} \cos(\omega t) dz \tag{A.8}$$

If wheeler stretching is employed, this can be integrated up to the free surface wave elevation, but the vertical coordinate must be "shifted", introducing this shift, the force on a section is:

$$\begin{aligned} dF &= \rho\pi r^2(1 + C_A)\omega^2 \zeta_A \frac{\cosh(k(\frac{z-\zeta}{1+\frac{\zeta}{h}} + h))}{\sinh(kh)} \cos(\omega t) dz \\ &= \rho\pi r^2(1 + C_A)\omega^2 \zeta_A \frac{\cosh(k\frac{z+h}{1+\frac{\zeta}{h}})}{\sinh(kh)} \cos(\omega t) dz \end{aligned} \tag{A.9}$$

Then the force on a pile is given as

$$\begin{aligned} F &= \rho\pi r^2(1 + C_A)\omega^2 \zeta_A \frac{\cos(\omega t)}{\sinh(kh)} \int_{-h}^{\zeta} \cosh(k\frac{z + h}{1 + \frac{\zeta}{h}}) dz \\ &= \rho\pi r^2(1 + C_A)\omega^2 \zeta_A \frac{\cos(\omega t)}{\sinh(kh)} \frac{1}{k}(1 + \frac{\zeta}{h})[\sinh(k\frac{z + h}{1 + \frac{\zeta}{h}})]_{-h}^{\zeta} \end{aligned} \tag{A.10}$$

$$\begin{aligned} F &= \rho\pi r^2(1+C_A)\omega^2\zeta_A\frac{\cos(\omega t)}{\sinh(kh)}\frac{1}{k}(1+\frac{\zeta}{h})[\sinh(kh)-\sinh(0)] \\ &= \rho\pi r^2(1+C_A)\omega^2\zeta_A\cos(\omega t)\frac{1}{k}(1+\frac{\zeta}{h}) \end{aligned} \tag{A.11}$$

Introducing the wave profile:

$$F = \rho\pi r^2(1+C_A)\omega^2\frac{\zeta_A}{k}\cos(\omega t) + \rho\pi r^2(1+C_A)\omega^2\frac{\zeta_A^2}{kh}\cos(\omega t)\sin(\omega t) \tag{A.12}$$

$$F = \rho\pi r^2(1+C_A)\omega^2\frac{\zeta_A}{k}\cos(\omega t) + \rho\pi r^2(1+C_A)\omega^2\frac{\zeta_A^2}{2kh}\sin(2\omega t) \tag{A.13}$$

It is apparent that this method will give rise to sum frequency forces for the case of finite water depths.

The method was presented by Wheeler (1970) and seems to be used regularly when calculating wave forces from irregular sea. It is based on observation that fluid velocity at the still water level is reduced in the real world compared to predictions from linear theory (Veritas, 2010).

In the original paper the author states that when the coordinate shift is introduced, the solution to the incident waves no longer satisfy Laplace's equation.

Stansberg et al. (2008) have compared various methods for predicting kinematics with results obtained by laser-doppler-velocimetry. Among them wheeler stretching. They have found that in steep waves the wheeler method significantly underpredicts the velocities in steep waves on all depth levels when used with wave elevation calculated as a sum of linear waves . The error is in the range $0.5k_0A_0 - 0.75k_0A_0$ where k_0A_0 is the local wave steepness.

According to the same paper, if wheeler stretching is based on a measured time series, or a second order wave kinematics model, then accuracy is improved at the free surface. The same range of errors are still present below $z = 0$.

B

In this appendix much of the calculations in section 5.7 are performed.

B.1 Simplification

First the simplification of equation 5.16 is performed.

Equation 5.16 is:

$$\begin{gathered}
\mathrm{d}F_x = (\rho\frac{\pi D^2}{4} + m_x)\omega^2\zeta_A\frac{\cosh(k(z+h))}{\sinh(kh)}\cos(\omega t - kx) + \\
(\rho\frac{\pi D^2}{4} + m_x) * \omega\zeta_A\frac{\cosh(k(z+h))}{\sinh(kh)}\sin(\omega t - kx) * -k\omega\zeta_A\frac{\cosh(k(z+h))}{\sinh(kh)}\cos(\omega t - kx) + \\
(\rho\frac{\pi D^2}{4} + m_x) * \omega\zeta_A\frac{\sinh(k(z+h))}{\sinh(kh)}\cos(\omega t - kx) * k\omega\zeta_A\frac{\sinh(k(z+h))}{\sinh(kh)}\sin(\omega t - kx) + \\
m_x * k\omega\zeta_A\frac{\cosh(k(z+h))}{\sinh(kh)}\cos(\omega t - kx) * \omega\zeta_A\frac{\cosh(k(z+h))}{\sinh(kh)}\sin(\omega t - kx)
\end{gathered} \tag{B.1}$$

By simply pulling together the correct terms into powers we obtain

$$\begin{aligned}
\mathrm{d}F_x = (\rho\frac{\pi D^2}{4}+m_x)\omega^2\zeta_A\frac{\cosh(k(z+h))}{\sinh(kh)}\cos(\omega t-kx)+ \\
-(\rho\frac{\pi D^2}{4}+m_x)*\omega^2\zeta_A^2\frac{\cosh^2(k(z+h))}{\sinh^2(kh)}\sin(\omega t-kx)k\cos(\omega t-kx)+ \\
(\rho\frac{\pi D^2}{4}+m_x)*\omega^2\zeta_A^2\frac{\sinh^2(k(z+h))}{\sinh^2(kh)}\sin(\omega t-kx)k\cos(\omega t-kx)+ \\
m_x*k\omega^2\zeta_A^2\frac{\cosh^2(k(z+h))}{\sinh^2(kh)}\cos(\omega t-kx)\sin(\omega t-kx)
\end{aligned} \tag{B.2}$$

The second and third line might be pulled together, so the following is given:

$$\begin{aligned}
&\mathrm{d}F_x = \\
&(\rho\frac{\pi D^2}{4}+m_x)\omega^2\zeta_A\frac{\cosh(k(z+h))}{\sinh(kh)}\cos(\omega t-kx) \\
&+(\rho\frac{\pi D^2}{4}+m_x)*k\omega^2\zeta_A^2\frac{1}{\sinh^2(kh)}\sin(\omega t-kx)\cos(\omega t-kx)(-\cosh^2(k(z+h))+\sinh^2(k(z+ \\
&+m_x*k\omega^2\zeta_A^2\frac{\cosh^2(k(z+h))}{\sinh^2(kh)}\cos(\omega t-kx)\sin(\omega t-kx)
\end{aligned} \tag{B.3}$$

A relation between cosh and sinh is used:

$$\cosh^2(x)-\sinh^2(x)=1 \tag{B.4}$$

By introducing this for the last parenthesis in line two:

$$\begin{aligned}
\mathrm{d}F_x = (\rho\frac{\pi D^2}{4}+m_x)\omega^2\zeta_A\frac{\cosh(k(z+h))}{\sinh(kh)}\cos(\omega t-kx)+ \\
(\rho\frac{\pi D^2}{4}+m_x)*k\omega^2\zeta_A^2\frac{1}{\sinh^2(kh)}\sin(\omega t-kx)\cos(\omega t-kx)(-1)+ \\
m_x*k\omega^2\zeta_A^2\frac{\cosh^2(k(z+h))}{\sinh^2(kh)}\cos(\omega t-kx)\sin(\omega t-kx)
\end{aligned} \tag{B.5}$$

By writing line two into expressions

$$\begin{aligned}
\mathrm{d}F_x = (\rho\frac{\pi D^2}{4} + m_x)\omega^2\zeta_A\frac{\cosh(k(z+h))}{\sinh(kh)}\cos(\omega t - kx) + \\
-\rho\frac{\pi D^2}{4} * k\omega^2\zeta_A^2\frac{1}{\sinh^2(kh)}\sin(\omega t - kx)\cos(\omega t - kx) + \\
-m_x * k\omega^2\zeta_A^2\frac{1}{\sinh^2(kh)}\sin(\omega t - kx)\cos(\omega t - kx) + \\
m_x * k\omega^2\zeta_A^2\frac{\cosh^2(k(z+h))}{\sinh^2(kh)}\cos(\omega t - kx)\sin(\omega t - kx)
\end{aligned} \tag{B.6}$$

Line three and four can be simplified:

$$\begin{aligned}
\mathrm{d}F_x = (\rho\frac{\pi D^2}{4} + m_x)\omega^2\zeta_A\frac{\cosh(k(z+h))}{\sinh(kh)}\cos(\omega t - kx) + \\
-\rho\frac{\pi D^2}{4} * k\omega^2\zeta_A^2\frac{1}{\sinh^2(kh)}\sin(\omega t - kx)\cos(\omega t - kx) + \\
m_x * k\omega^2\zeta_A^2\frac{1}{\sinh^2(kh)}\cos(\omega t - kx)\sin(\omega t - kx)(\cosh^2(k(z+h)) - 1)
\end{aligned} \tag{B.7}$$

By utilising that

$$\cosh^2(x) - 1 = \sinh^2(x) \tag{B.8}$$

The following is found:

$$\begin{aligned}
\mathrm{d}F_x = (\rho\frac{\pi D^2}{4} + m_x)\omega^2\zeta_A\frac{\cosh(k(z+h))}{\sinh(kh)}\cos(\omega t - kx) + \\
-\rho\frac{\pi D^2}{4} * k\omega^2\zeta_A^2\frac{1}{\sinh^2(kh)}\sin(\omega t - kx)\cos(\omega t - kx) + \\
m_x * k\omega^2\zeta_A^2\frac{\sinh^2(k(z+h))}{\sinh^2(kh)}\cos(\omega t - kx)\sin(\omega t - kx)
\end{aligned} \tag{B.9}$$

Which is the same as:

$$\mathrm{d}F_x = (\rho\frac{\pi D^2}{4} + m_x)\omega^2\zeta_A\frac{\cosh(k(z+h))}{\sinh(kh)}\cos(\omega t - kx)+$$
$$(m_x \sinh^2(k(z+h)) - \rho\frac{\pi D^2}{4}) * k\omega^2\zeta_A^2\frac{1}{\sinh^2(kh)}\sin(\omega t - kx)\cos(\omega t - kx) \tag{B.10}$$

For a circular cylinder $m_x = C_A\rho\frac{\pi D^2}{4}$ where C_A is the added mass coefficient. By also setting $x = 0$, and introducing $\sin(2x) = 2\cos(x)\sin(x)$ The result can then be further simplified to:

$$\begin{gathered}\mathrm{d}F_x = (1 + C_A)\rho\frac{\pi D^2}{4}\omega^2\zeta_A\frac{\cosh(k(z+h))}{\sinh(kh)}\cos(\omega t)+ \\ (C_A \sinh^2(k(z+h)) - 1)\rho\frac{\pi D^2}{4}k\omega^2\zeta_A^2\frac{1}{\sinh^2(kh)}\frac{1}{2}\sin(2\omega t)\end{gathered} \tag{B.11}$$

B.2 Integration

The next part is the integration over the structure, which is the integral in equation 5.19

$$F = \rho\pi r^2 k\omega^2\zeta_A^2\frac{1}{\sinh^2(kh)}\frac{1}{2}\sin(2\omega t)\int_{-h}^{\zeta}(C_A \sinh^2(k(\frac{z-\zeta}{1+\frac{\zeta}{h}} + h)) - 1)\mathrm{d}z \tag{B.12}$$

By using standard expressions for the integral of $\sinh^2(x)$ from Rottmann (2008) the integral turns out to be:

$$\int_{-h}^{\zeta}(C_A \sinh^2(k(\frac{z-\zeta}{1+\frac{\zeta}{h}}+h))-1)\mathrm{d}z = [C_A(\frac{1}{4k}(1+\frac{\zeta}{h})\sinh(2k(\frac{z-\zeta}{1+\frac{\zeta}{h}}+h))-\frac{z}{2})-z]_{-h}^{\zeta} \tag{B.13}$$

$$\begin{aligned}\int_{-h}^{\zeta}(C_A\sinh^2(k(\frac{z-\zeta}{1+\frac{\zeta}{h}}+h))-1)\mathrm{dz} &= C_A\frac{1}{4k}(1+\frac{\zeta}{h})\sinh(2kh)-C_A\frac{\zeta}{2}-C_A\frac{h}{2}-\zeta-h\\ &= C_A\frac{1}{4k}(1+\frac{\zeta}{h})\sinh(2kh)-\zeta(\frac{C_A}{2}+1)-h(\frac{C_A}{2}+1)\end{aligned} \tag{B.14}$$

This gives the force on the cylinder:

$$F=\rho\pi r^2k\omega^2\zeta_A^2\frac{1}{\sinh^2(kh)}\frac{1}{2}\sin(2\omega t)(C_A\frac{1}{4k}(1+\frac{\zeta}{h})\sinh(2kh)-\zeta(\frac{C_A}{2}+1)-h(\frac{C_A}{2}+1)) \tag{B.15}$$

The wave profile is given as $\zeta_A\sin(\omega t)$, by introducing this into the equation we obtain:

$$\begin{aligned}F=\rho\pi r^2k\omega^2\zeta_A^2\frac{1}{\sinh^2(kh)}\frac{1}{2}\sin(2\omega t)(C_A\frac{1}{4k}(1+\frac{\zeta_A\sin(\omega t)}{h})\sinh(2kh)\\ -\zeta_A\sin(\omega t)(\frac{C_A}{2}+1)-h(\frac{C_A}{2}+1))\end{aligned} \tag{B.16}$$

Now the part of collecting terms, comes to play. An identity that will be used is $2\sin(2x)\sin(x)=cos(x)-cos(3x)$.

$$\begin{aligned}F=\rho\pi r^2k\omega^2\zeta_A^2\frac{1}{\sinh^2(kh)}\frac{1}{2}C_A\frac{1}{4k}\sinh(2kh)\sin(2\omega t)\\ +\rho\pi r^2k\omega^2\zeta_A^2\frac{1}{\sinh^2(kh)}\frac{1}{2}C_A\frac{1}{4k}\sinh(2kh)\frac{\zeta_A\sin(\omega t)}{h}\sin(2\omega t)\\ -\rho\pi r^2k\omega^2\zeta_A^2\frac{1}{\sinh^2(kh)}\frac{1}{2}\zeta_A\sin(\omega t)(\frac{C_A}{2}+1)\sin(2\omega t)\\ -\rho\pi r^2k\omega^2\zeta_A^2\frac{1}{\sinh^2(kh)}\frac{1}{2}h(\frac{C_A}{2}+1))\sin(2\omega t)\end{aligned} \tag{B.17}$$

By using the identity above:

$$\begin{aligned}F = \frac{1}{8}C_A\rho\pi r^2 k\omega^2\zeta_A^2\frac{1}{\sinh^2(kh)}\frac{1}{k}\sinh(2kh)\sin(2\omega t)\\
+\frac{1}{16}\rho\pi r^2 k\omega^2\zeta_A^3\frac{1}{\sinh^2(kh)}C_A\frac{1}{kh}\sinh(2kh)(\cos(\omega t)-\cos(3\omega t))\\
-\frac{1}{4}\rho\pi r^2 k\omega^2\zeta_A^3\frac{1}{\sinh^2(kh)}(\frac{C_A}{2}+1)(\cos(\omega t)-\cos(3\omega t))\\
-\frac{1}{2}\rho\pi r^2 k\omega^2\zeta_A^2\frac{1}{\sinh^2(kh)}h(\frac{C_A}{2}+1))\sin(2\omega t)\end{aligned} \tag{B.18}$$

Restructuring gives us:

$$\begin{aligned}F = \rho\pi r^2 k\omega^2\zeta_A^3\frac{1}{\sinh^2(kh)}(\frac{1}{16}C_A\frac{1}{kh}\sinh(2kh)-\frac{1}{4}(\frac{C_A}{2}+1))\cos(\omega t)\\
+\rho\pi r^2 k\omega^2\zeta_A^2\frac{1}{\sinh^2(kh)}(\frac{1}{8}C_A\frac{1}{k}\sinh(2kh)-\frac{1}{2}h(\frac{C_A}{2}+1))\sin(2\omega t)\\
+\rho\pi r^2 k\omega^2\zeta_A^3\frac{1}{\sinh^2(kh)}(\frac{1}{4}(\frac{C_A}{2}+1)-\frac{1}{16}C_A\frac{1}{kh}\sinh(2kh))\cos(3\omega t)\end{aligned} \tag{B.19}$$

B.3 Free Surface Intersection Force

For the free surface intersection force there are two cases, first the case on the left side of figure 5.1 will be expanded, and then the expressions on the right side.

Inserting the correct values into equation 5.22

$$\begin{aligned}F_{SI} = \frac{1}{2}\frac{\partial\zeta}{\partial x}[(\begin{bmatrix}-1\\0\\0\end{bmatrix}\cdot\begin{bmatrix}u-U_x\\v-U_y\\w-U_z\end{bmatrix})\begin{bmatrix}m_x&0&0\\0&m_y&0\\0&0&0\end{bmatrix}\begin{bmatrix}u-U_x\\v-U_y\\w-U_z\end{bmatrix}-\\
(\begin{bmatrix}-1\\0\\0\end{bmatrix}\cdot(\begin{bmatrix}0\\0\\1\end{bmatrix}\times\begin{bmatrix}m_x&0&0\\0&m_y&0\\0&0&0\end{bmatrix}\begin{bmatrix}u-U_x\\v-U_y\\w-U_z\end{bmatrix}))(\begin{bmatrix}0\\0\\1\end{bmatrix}\times\begin{bmatrix}u-U_x\\v-U_y\\w-U_z\end{bmatrix})\end{aligned} \tag{B.20}$$

Since the cylinder is assumed stiff for this specific case, and all waves are long crested, which propagates in the x direction, this reduces to:

$$\begin{aligned} F_{SIx} = \frac{1}{2}\frac{\partial \zeta}{\partial x}[(\begin{bmatrix}-1\\0\\0\end{bmatrix} \cdot \begin{bmatrix}u\\0\\w\end{bmatrix})\begin{bmatrix}m_x & 0 & 0\\0 & m_y & 0\\0 & 0 & 0\end{bmatrix}\begin{bmatrix}u\\0\\w\end{bmatrix} - \\ (\begin{bmatrix}-1\\0\\0\end{bmatrix} \cdot (\begin{bmatrix}0\\0\\1\end{bmatrix} \times \begin{bmatrix}m_x & 0 & 0\\0 & m_y & 0\\0 & 0 & 0\end{bmatrix}\begin{bmatrix}u\\0\\w\end{bmatrix}))(\begin{bmatrix}0\\0\\1\end{bmatrix} \times \begin{bmatrix}u\\0\\w\end{bmatrix}) \end{aligned} \tag{B.21}$$

Working out the matrix operations, the result is:

$$F_{SI} = \frac{1}{2}\frac{\partial \zeta}{\partial x}[(-u\begin{bmatrix}m_x u\\0\\0\end{bmatrix}) - (\begin{bmatrix}-1\\0\\0\end{bmatrix} \cdot (\begin{bmatrix}0\\-m_x u\\0\end{bmatrix}))(\begin{bmatrix}0\\-u\\0\end{bmatrix})] \tag{B.22}$$

$$F_{SI} = -\frac{1}{2}\frac{\partial \zeta}{\partial x} m_x u^2 \tag{B.23}$$

For the case on the right side, by inserting the changes to α and $\boldsymbol{t}$-vector into equation B.21, the following is obtained:

$$\begin{aligned} F_{SIx} = \frac{1}{2} - \frac{\partial \zeta}{\partial x}[(\begin{bmatrix}1\\0\\0\end{bmatrix} \cdot \begin{bmatrix}u\\0\\w\end{bmatrix})\begin{bmatrix}m_x & 0 & 0\\0 & m_y & 0\\0 & 0 & 0\end{bmatrix}\begin{bmatrix}u\\0\\w\end{bmatrix} - \\ (\begin{bmatrix}1\\0\\0\end{bmatrix} \cdot (\begin{bmatrix}0\\0\\1\end{bmatrix} \times \begin{bmatrix}m_x & 0 & 0\\0 & m_y & 0\\0 & 0 & 0\end{bmatrix}\begin{bmatrix}u\\0\\w\end{bmatrix}))(\begin{bmatrix}0\\0\\1\end{bmatrix} \times \begin{bmatrix}u\\0\\w\end{bmatrix}) \end{aligned} \tag{B.24}$$

Which again reduces to

$$F_{SI} = -\frac{1}{2}\frac{\partial \zeta}{\partial x} m_x u^2 \tag{B.25}$$

The last part of the force, will be zero for all vertical cylinders with isotropic added mass.

C

This appendix describes the changes made to the source code of FAST as a part of this thesis.

C.1 Implementing the Changes in FAST

In FAST the waves are generated as a time series in the initialisation of the program. The Wave elevation is calculated at the platform reference point/ centre line ($x = 0$). The kinematics of the incident waves are also calculated at this point for the various depths. The fact that the waves are calculated before the time stepping procedure, means that it is not possible to take into account an eventual movement of the element where it should actually be subjected to kinematics from a slightly different position.

C.1.1 Additions to Linear Wave Generation

In the current load model, the acceleration is used without the convective terms, so not all the necessary wave kinematics for Rainey's expressions are calculated. There is thus a need to extend the calculations for the linear waves.

As it is, FAST is only calculating the local accelerations $\frac{\partial u}{\partial t}$ and $\frac{\partial w}{\partial t}$. For the inertia load and axial divergence load the convective accelerations of the incident wave, and also the velocity gradient matrix are needed. This sections describes the mathematics behind the implementation.

The velocity gradient matrix is defined as

$$\begin{bmatrix} \frac{\partial u}{\partial x} & \frac{\partial u}{\partial y} & \frac{\partial u}{\partial z} \\ \frac{\partial v}{\partial x} & \frac{\partial v}{\partial y} & \frac{\partial v}{\partial z} \\ \frac{\partial w}{\partial x} & \frac{\partial w}{\partial y} & \frac{\partial w}{\partial z} \end{bmatrix} \tag{C.1}$$

And the convective accelerations which are needed can be defined as:

$$a_x = \frac{\partial u}{\partial t} + u\frac{\partial u}{\partial x} + v\frac{\partial u}{\partial y} + w\frac{\partial u}{\partial z} \tag{C.2}$$

$$a_y = \frac{\partial v}{\partial t} + u\frac{\partial v}{\partial x} + v\frac{\partial v}{\partial y} + w\frac{\partial v}{\partial z} \tag{C.3}$$

$$a_z = \frac{\partial w}{\partial t} + u\frac{\partial w}{\partial x} + v\frac{\partial w}{\partial y} + w\frac{\partial w}{\partial z} \tag{C.4}$$

Since FAST is only implementing a plane wave, the time series of the free surface elevation is first calculated in a local coordinate system (x', z'). Afterwards it is transformed into a three-dimensional coordinate system (x, y, z), allowing for a general propagation direction of the incident waves. All the parts of the velocity gradient matrix is to be calculated in the local (x', z') coordinate system which is rotated β degrees to the global. In order to represent the waves in the calculations, a transformation to the global (x, y, z) system is needed.

Since the transformation is merely a rotation of the x- and y-axis, the z-axis will not be transformed. A purely rotation of the coordinate system (x, y, z) around the origin into the system (x', y', z'), with a rotation angle given by β, leads to the following relations:

$$x' = x\cos(\beta) + y\sin(\beta) \tag{C.5}$$

$$x = x'\cos(\beta) - y'\sin(\beta) \tag{C.6}$$

$$y' = y\cos(\beta) - x\sin(\beta) \tag{C.7}$$

$$y = x'\sin(\beta) + y'\cos(\beta) \tag{C.8}$$

$$z' = z \tag{C.9}$$

The partial derivatives of x' with respect to x and y will be needed.

$$\frac{\partial x'}{\partial x} = \cos(\beta) \tag{C.10}$$

$$\frac{\partial x'}{\partial y} = \sin(\beta) \tag{C.11}$$

Since the velocities (u, v, w) are parallel with the directions (x, y, z), and the velocities (u', v', w') are parallel with the directions (x', y', z'), the transformations of the velocities from one coordinate system to the other is similar to the above expressions.

In the local coordinate system the velocities (u', v', w') are in fact only two dimensional, with no component v' in the y' direction, leading to the following expressions for the velocity transformations:

$$u = u'\cos(\beta) \tag{C.12}$$

$$v = u'\sin(\beta) \tag{C.13}$$

$$w = w' \tag{C.14}$$

With the given relationships it can be shown that the the partial derivatives can be written as:

$$\frac{\partial u}{\partial x} = \frac{\partial u'}{\partial x}\cos(\beta) = \frac{\partial u'}{\partial x'}\frac{\partial x'}{\partial x}\cos(\beta) = \frac{\partial u'}{\partial x'}\cos^2(\beta) \tag{C.15}$$

And similarly for the other components:

$$\frac{\partial u}{\partial y} = \frac{\partial u'}{\partial x'}\cos(\beta)\sin(\beta) \tag{C.16}$$

$$\frac{\partial u}{\partial z} = \frac{\partial u'}{\partial z}\cos(\beta) \tag{C.17}$$

$$\frac{\partial v}{\partial x} = \frac{\partial u'}{\partial x'}\cos(\beta)\sin(\beta) \tag{C.18}$$

$$\frac{\partial v}{\partial y} = \frac{\partial u'}{\partial x'}\sin^2(\beta) \tag{C.19}$$

$$\frac{\partial v}{\partial z} = \frac{\partial u'}{\partial z'}\sin(\beta) \tag{C.20}$$

$$\frac{\partial w}{\partial x} = \frac{\partial w'}{\partial x'}\cos(\beta) \tag{C.21}$$

$$\frac{\partial w}{\partial y} = \frac{\partial w'}{\partial x'}\sin(\beta) \tag{C.22}$$

$$\frac{\partial w}{\partial z} = \frac{\partial w'}{\partial z'} \tag{C.23}$$

The velocity components (u', z') are determined from standard expressions from linear theory.

They way FAST generates time series are with an Inverse Fourier transform of Fourier coefficients. The theory takes advantage of the way the velocity potential for an incident linear wave at finite depth can be defined using complex numbers:

$$\phi = \mathrm{Re}\{\frac{ig\zeta_A}{\omega}\frac{\cosh(k(z'+h))}{cosh(kh)}e^{-ikx'}e^{i\omega t}\} \tag{C.24}$$

The free surface is given as:

$$\zeta' = \mathrm{Re}\{\zeta_A e^{-ikx'}e^{i\omega t}\} \tag{C.25}$$

The velocities can be found by differentiation with respect to x and z. Taking the real part is implied in all the following expressions.

$$u' = \frac{\partial \phi}{\partial x} = \omega\zeta_A\frac{\cosh(k(z'+h))}{\sinh(kh)}e^{-ikx'}e^{i\omega t} \tag{C.26}$$

$$w' = \frac{\partial \phi}{\partial z} = i\omega\zeta_A\frac{\sinh(k(z'+h))}{\sinh(kh)}e^{-ikx'}e^{i\omega t} \tag{C.27}$$

The linear dispersion relationship for finite water has been utilised in order to simplify the expressions.

$$\omega^2 = kg\tanh(kh) \tag{C.28}$$

The Fourier coefficients for the velocities are the above expressions, except for the time dependence part.

From these expressions it is straight forward to obtain the relevant convective accelerations:

$$\frac{\partial u'}{\partial x'} = -iku' \tag{C.29}$$

$$\frac{\partial u'}{\partial z'} = k\omega\zeta_A \frac{\sinh(k(z'+h))}{\sinh(kh)} e^{-ikx'} e^{i\omega t} \tag{C.30}$$

$$\frac{\partial w'}{\partial x'} = -ikw' \tag{C.31}$$

$$\frac{\partial w'}{\partial z'} = k\omega\zeta_A \frac{\cosh(k(z'+h))}{\sinh(kh)} e^{-ikx'} e^{i\omega t} \tag{C.32}$$

Again the Fourier coefficients are simply the expressions except for the $e^{i\omega t}$ part.

For the oblique slam load also the surface slope, and velocity at the free surface are needed. The expressions for the velocity are in principle only valid up to the mean free surface, but various stretching techniques can be applied in FAST. In this implementation vertical stretching and Wheeler stretching has been enabled. Both of these models use the velocity at $z = 0$ at the instantaneous free surface.

The wave slope for a linear wave is simply

$$\frac{\partial \zeta'}{\partial x'} = -ik\zeta_A e^{-ikx'} e^{i\omega t} \tag{C.33}$$

Since FAST is not considering the wave kinematics at the actual position of the tower, i.e. that the tower displacement is small, all the quantities should be evaluated at the platform centre, $x = 0$. This means that the exponential term including x is 1. The total expressions implemented as the Fourier coefficients in FAST is then:

$$\frac{\partial u}{\partial x} = -ik\omega\zeta_A \frac{\cosh(k(z'+h))}{\sinh(kh)} \cos^2(\beta) \tag{C.34}$$

$$\frac{\partial u}{\partial y} = -ik\omega\zeta_A \frac{\cosh(k(z'+h))}{\sinh(kh)}\cos(\beta)\sin(\beta) \tag{C.35}$$

$$\frac{\partial u}{\partial z} = k\omega\zeta_A \frac{\sinh(k(z'+h))}{\sinh(kh)}\cos(\beta) \tag{C.36}$$

$$\frac{\partial v}{\partial x} = -ik\omega\zeta_A \frac{\cosh(k(z'+h))}{\sinh(kh)}\cos(\beta)\sin(\beta) \tag{C.37}$$

$$\frac{\partial v}{\partial y} = -ik\omega\zeta_A \frac{\cosh(k(z'+h))}{\sinh(kh)}\sin^2(\beta) \tag{C.38}$$

$$\frac{\partial v}{\partial z} = k\omega\zeta_A \frac{\sinh(k(z'+h))}{\sinh(kh)}\sin(\beta) \tag{C.39}$$

$$\frac{\partial w}{\partial x} = k\omega\zeta_A \frac{\sinh(k(z'+h))}{\sinh(kh)}\cos(\beta) \tag{C.40}$$

$$\frac{\partial w}{\partial y} = k\omega\zeta_A \frac{\sinh(k(z'+h))}{\sinh(kh)}\sin(\beta) \tag{C.41}$$

$$\frac{\partial w}{\partial z} = ik\omega\zeta_A \frac{\cosh(k(z'+h))}{\sinh(kh)} \tag{C.42}$$

$$\frac{\partial \zeta}{\partial x} = -ik\zeta_A e^{-ikx'} e^{i\omega t}\cos(\beta) \tag{C.43}$$

$$\frac{\partial \zeta}{\partial y} = -ik\zeta_A e^{-ikx'} e^{i\omega t}\sin(\beta) \tag{C.44}$$

With the given expressions, the calculation of the components in the velocity matrix is implemented in the wave initialisation part of FAST. The implementation has been made so it is merely an extension of the current calculations.

FAST has the possibility to use one of the four possibilities for kinematic stretching: no stretching, i.e consistent linear theory, Vertical stretching, extrapolation stretching and wheeler stretching. The new wave features has been implemented for all methods, except for the extrapolation stretching. The reason for dropping support for this technique is that it will not be used in the studies, and it is a bit more complex than the others.

All the above expressions are for a single regular wave, in order to generate irregular seas FAST is simply performing a summation over the the various frequencies. The wave amplitude then needs to be decided based on a wave spectrum, and a random phase angle. FAST has the possibility of utilising a Pierson-Moskowitz spectrum, a JONSWAP-spectrum or a user defined spectrum. To incorporate a random phase, FAST uses a white-Gaussian-noise process. The irregular sea states are then generated as described in (Emmerhoff, 1994, section 6.3).

C.1.2 Fenton Generated Waves

As part of the validation of the solver in chapter 8 and verification of the load model in chapter 9, nonlinear regular waves was needed. Section 6.1 shows a procedure in which nonlinear regular waves may be generated by a Fourier approximation to the problem of steady waves.

An external Fenton program is first run to generate the wave input file. An example of the file can be found in appendix D. The actual implementation into FAST is found in the source code of FAST, given in the digital appendix.

This file is then read by FAST, and a time series of the following quantities are generated for all element nodes below the instantaneous free surface elevation at the actual position of the calculation node. If the free surface elevation is such that the node of an element is above the free surface, but the element is partly submerged, then the kinematics at the free surface is used for this node. This has been implemented this way to avoid the inherent errors in the way FAST calculates the wave kinematics for linear waves and applies it to calculate forces. These errors will be explored in section C.1.5.

As for the linear case, all quantities are first calculated in a local coordinate system (x', z') and then transformed back to the global (x, y, z) system.

The input file from the Fenton program gives the user several non-dimensional characteristics and Fourier coefficients for the free surface elevation and Fourier coefficients for the solution in the fluid domain i.e the wave kinematics. The number of Fourier coefficients is determined by the user as an input to the program and might be denoted by N. The mathematical expressions is given as:

$$\zeta' = \frac{1}{k} \sum_{j=1}^{N} {}^{\prime} E_j \cos(jk(x' - ct)) \tag{C.45}$$

E_j is the j'th component of the Fourier transform of the free surface elevation, x' is the position along the local x-axis, k the wave number which is given in the output file, t the time and c' is the local wave speed. the sign Σ‘ means that in the summation the contributions from $j = 0$ and $j = N$(if they should be included) are multiplied with 0.5.

The velocity in local x' direction

$$u' = c' - \bar{u}' + \sqrt{\frac{g}{k}} \sum_{j=1}^{N} jB_j \frac{\cosh(jk(h+z'))}{\cosh(jkh)} \cos(jk(x'-ct))) \tag{C.46}$$

where u' is the velocity component in the local x' direction, c' the local wave direction, $\bar{u}'$ the local mean fluid speed in the frame of the wave, g the gravitational constant set to 9.81, k wave number, B_j the Fourier coefficient for the fluid solution for component j, h is the water depth.

The velocity in z' direction might be found by:

$$w' = \sqrt{\frac{g}{k}} \sum_{j=1}^{N} jB_j \frac{\sinh(jk(h+z'))}{\cosh(jkh)} \sin(jk(x'-ct))) \tag{C.47}$$

The rest of the needed quantities are easily found by differentiation of the given expressions, but are omitted here.

To transform the local variables into the global coordinate system, the same relations as in section C.1.1 has been used.

All in all the implementation is quite similar to the linear case, except that all the data must be read from an input file which has been made in advance. The name of the input file is given in one of the input files to FAST, where there is already a place for the input file of wave data calculated in the style of another simulation tool called GH Bladed.

In the FAST input files, there is a field to specify which wave theory that should be utilised. A slight modification to the input/output routine has made it possible to extend the possibilities of this field, so that Fenton generated waves are a possible entry. A similar modification was also necessary so that the file name was actually read when this was chosen.

C.1.3 Fully Nonlinear Waves

FAST has the possibility to input externally calculated waves, a feature that will be used for the fully nonlinear MEL generated waves. For the case of Morison's equation, there is not necessary to make any changes to FAST in order to include these forces. However, Rainey's expressions requires the spacial derivatives, and also the slope of the free surface. The way this has been implemented is that the needed quantities are generated externally, and then a slight modification has been made to the way FAST reads the needed files. The change has been made so that only when wave forces are to be calculated by Rainey's expressions, the extra files are read.

The fully nonlinear solver does not calculate the spacial derivatives directly, but it calculates the velocity at a position just before the turbine, and just after. In this way a grid of points where the velocity is known has been calculated. The spacial derivatives can then be calculated by a central difference formula. These calculations must be performed before running FAST. The routine for performing the calculations can be found in appendix E

C.1.4 Force Calculations

The new force calculations has been implemented in FAST in the same style as the existing Morison calculations. Therefore the following section stands as both a description of how FAST is currently calculating, and also how the new features has been implemented.

FAST is dividing the tower into a user selected number of elements, and allocates a node to the centre of each element. All elements has equal length in the version of FAST that I have worked on.

Hydrodynamically the structure is considered as only a line, so all kinematics are calculated at the centre line and for each calculation node. Also how much of an element that is submerged is calculated based on the wave elevation at the centre line.

All forces on a element fully submerged is applied at the calculation node in the centre of the element as a force in x, y or z -direction. The force is calculated based on the kinematics at the calculation node. There is also an additional moment around each of the three axes. For a fully submerged element this will however be zero since the load is assumed constant over the element, which gives symmetric contribution above and below the calculation node.

For the force on a partly submerged element, the basic assumption is again that the force per length over an element is constant, and equal to the force calculated at the calculation node. However to represent that such an element would be subject to a moment due to the centre of pressure being below the centre of the element, the centre of pressure is set to be the point halfway between the the free surface and the submerged end of the element. The force is then applied at the calculation node, but since the centre of pressure is at a distance from the middle of the element, there will also be a non-zero moment applied to this node. The arm in the moment is just the length from the centre of pressure to the calculation node.

Figure C.1 shows how the structure is discretised.

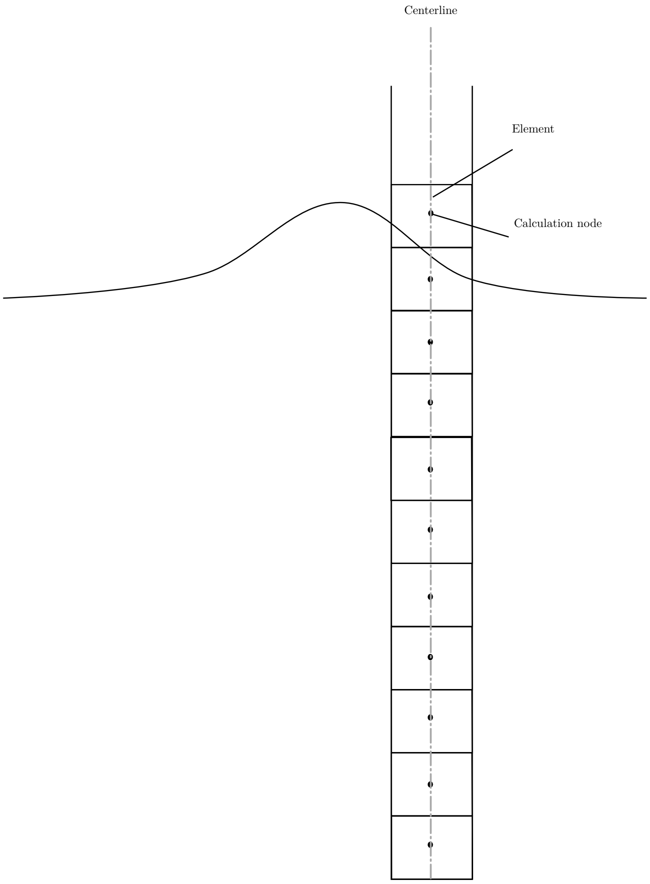

Figure C.1: Discretisation of structure into elements and nodes

This way of implementing the force is of course an approximation since a finite number of elements are used. At the deepest elements the variation of the force over the element will not be as great as in the free surface zone where the kinematics of the incident waves have large spatial variations. In this zone it is necessary with smaller elements than at the seabed. FAST does not have a possibility to cluster elements, so it is necessary to use sufficiently small elements on the whole structure.

The force on a submerged element is implemented as expression 5.2, except for the last three terms, which for the case studied here will be zero. In the implementation of the force itself, no assumptions have been made regarding the structure, but in the implementation of the $\boldsymbol{l}$ and $\boldsymbol{t}$ vectors, the structure has been assumed totally stiff.

Since this is a steel structure it will be quite stiff, so it might be assumed that the structure is undeflected, causing $\boldsymbol{l}$ - and $\boldsymbol{t}$ -vectors to remain the same for all deflections. This is an simplification, but it is in line with how the wave kinematics are calculated, where the kinematics at the un-deflected centre line is used to calculate forces for all time steps.

It is important to stress that even if the structure is assumed stiff, the actual element velocity is used to calculate the relative velocity between the structure and the water particles.

The term that gives a forces from the structural acceleration(term 3 in equation 5.2) is already implemented in FAST, at a different point in the calculations. Therefore it is not necessary to implement this in the calculations.

For the oblique slam force there is no established way of implementing it, since the existing load calculations does not include any point force. The value of the force is calculated using the kinematics of the water at the free surface, the velocity of the structure at the free surface, and the instantaneous slope of the free surface, all quantities at the platform centre line.

The force is applied at the calculation node of the element at the free surface. In order for the moment applied to the node to be correct, the arm is the actual arm between the free surface and the calculation node. There is however a small trick to the implementation in FAST. Presently it is assuming that the forces calculated is the cross sectional force and should be equal over the whole element, thus it will multiply the force calculated with the element length. This force is not a distributed force, so in order to obtain the correct force on an element, the calculated force needs to be divided by the element length in the routine.

In the routine the total cross sectional load on the structure is made by summation of the force components, and then at a later time this total force will be multiplied with the element length. Since the oblique slam load has been divided by the element length, and the total force is just a summation of the components it follows that the oblique slam will end up with the correct value.

C.1.5 Error in Wave Implementation in FAST

There is an error in how FAST implements the calculation of linear wave kinematics and how it uses it to calculate forces. This error is briefly mentioned in the source code of FAST, but without explanation. This aspect will be shortly presented here.

When calculating the wave kinematics FAST uses the calculation node to decide if an element is submerged or not. If an calculation node is above the free surface elevation, then kinematics are not calculated for this element. It might be that an element is partly submerged, but the calculation node is above the wave elevation, so this element will be wrongly set as completely dry when calculating the kinematics.

Later in the process the forces are calculated using the previously calculated kinematics. FAST interpolates into the data of the needed quantity to obtain the kinematics used to calculate the force. They way FAST decides if an element is submerged is no longer to look if the node is submerged, but if some part of the element is below the free surface elevation. The force is then calculated based on the kinematics of the element's node. Since it is to interpolate into the data, but the position where the value is wanted is above the range where values exists, it is set to the nearest value. For the case discussed here it will mean that for the element in question, the force is calculated using kinematics from the next element. When then the calculation node of the partly submerged element comes below the free surface elevation at a later time, there will be a jump in the force, since suddenly the kinematics have been calculated at another position.

A workaround for this error mentioned in the source code of FAST is to use a lot of elements. This will lead to smaller errors, since the distance between nodes where kinematics are calculated is small. If for instance 200 elements are used on the reference turbine, then each element is $\approx 5.4[cm]$ long. When talking about frequencies, these jumps in the force will be found as higher order disturbances, and depending on the size can make it more difficult to perform an decomposition of the force into it's harmonics.

This error is not present when Fenton generated waves are used, because care has been taken to also anticipate this case. In this case the kinematics for an element where the node is not submerged, but some part of it is, kinematics are calculated at the free surface. This is done to create a seamless transition to when the node becomes submerged, and kinematics are calculated at the node.

The error is not thought to give significant errors for a full size turbine. However when using the waves to validate against experiments, it can have an effect when performing a Fourier transform of the result to obtain harmonics. Due to the small jumps, a Fourier transform will give some spurious non physical higher order force components.

D

```
# Test wave: the program does not reqire data to be annotated − it
    could be of this form:
# Height/Depth: 0.071, Dimensionless Period:  2.64 Current criterion
    : Euler,  Magnitude: 0.00
# (This has a height 43% of the maximum value of H/d=0.163 for this
    wavelength)

# Solution by Fourier approximation:  1 terms in series

# Integral quantities − notation from Fenton (1988)
# (1) Quantity, (2) symbol, solution non−dimensionalised by (3) g &
    wavenumber, and (4) g & mean depth

# Water depth                         (d)        5.4597   1.0000
# Wave length                    (lambda)        6.2832   1.1508
# Wave height                         (H)        0.3852   0.0705
# Wave period                       (tau)        6.1671   2.6394
# Wave speed                          (c)        1.0188   0.4360
# Eulerian current                  (u1_)        0.0000   0.0000
# Stokes current                    (u2_)        0.0068   0.0029
# Mean fluid speed in frame of wave (U_)         1.0188   0.4360
# Volume flux due to waves            (q)        0.0373   0.0029
# Bernoulli constant                  (r)        0.5009   0.0917
# Volume flux                         (Q)        5.5251   0.4331
# Bernoulli constant                  (R)        5.9606   1.0917
# Momentum flux                       (S)       20.3180   0.6816
# Impulse                             (I)        0.0373   0.0029
# Kinetic energy                      (T)        0.0190   0.0006
# Potential energy                    (V)        0.0185   0.0006
# Mean square of bed velocity     (ub2_)        −0.0362  −0.0066
# Radiation stress                  (Sxx)       −0.1770  −0.0059
# Wave power                          (F)       −0.0809  −0.0012

# Dimensionless coefficients in Fourier series
# Potential/Streamfn    Surface elevations
# j, B[j], & E[j], j=1..N

 1        1.9262880e−01    3.8516143e−01
EOF
```

E

E.1 Matlab Script for Calculating Spatial Derivatives

```
clear all
close all
clc

%Read in important charachteristics
DX = textread('FNL_DX.txt','%f');
tmp = textread('FNL_FAST.txt','%f');
nnodes = tmp(1);
ypos = tmp(2:end);
dy=zeros(nnodes,1);
for i=1:nnodes-1
    dy(i) = ypos(i+1)-ypos(i);
end



%Read in free surface
[vx_f vy_f vz_f] = textread('vx_vy_f.txt','%f␣%f␣%f');
[vx_f_l vy_f_l vz_f_l] = textread('vx_vy_f_left.txt','%f␣%f␣%f');
[vx_f_r vy_f_r vz_f_r] = textread('vx_vy_f_right.txt','%f␣%f␣%f');

%Read in submerged
[v_x v_y v_z tmp tmp tmp tmp]= textread('FNL_kinematics.txt','␣%f␣%f
    ␣%f␣%f␣%f␣%f␣%f');
[v_x_l v_y_l v_z_l tmp tmp tmp tmp]= textread('vx_vy_left.txt', '%f␣
    %f␣%f␣%f␣%f␣%f␣%f');
[v_x_r v_y_r v_z_r tmp tmp tmp tmp]= textread('vx_vy_right.txt', '%f
    ␣%f␣%f␣%f␣%f␣%f␣%f');
```

```
clear tmp;
n = length(v_x);

dudx = zeros(n,1);
dudy = zeros(n,1);
dudz = zeros(n,1);

dvdx = zeros(n,1);
dvdy = zeros(n,1);
dvdz = zeros(n,1);

dwdx = zeros(n,1);
dwdy = zeros(n,1);
dwdz = zeros(n,1);

dudx = (v_x_r-v_x_l)./(2*DX);
dwdx = (v_z_r-v_x_l)./(2*DX);
teller = 0;
for i = 1:n
teller = teller+1;

if v_x(i) ~= 0.0 && v_z(i) ~=0.0
if teller == 1
    dudz(i) = (v_x(i+1)- v_x(i))/dy(teller);
    dwdz(i) = (v_z(i+1)-v_z(i))/dy(teller);

elseif teller == nnodes
    dudz(i) = (v_x(i)- v_x(i-1))/dy(teller-1);
    dwdz(i) = (v_z(i)-v_z(i-1))/dy(teller-1);
else
    dudz(i) = (v_x(i+1)- v_x(i-1))/(dy(teller)+dy(teller-1));
    dwdz(i) = (v_z(i+1)-v_z(i-1))/(dy(teller)+dy(teller-1));

end
end

if teller == nnodes
     teller = 0;
end
end

dlmwrite('FNL_extra.txt',[dudx dudy dudz dvdx dvdy dvdz dwdx dwdy dwdz],'delimiter','\t','precision','%8.6E');
dlmwrite('FNL_f.txt',[vx_f vy_f vz_f],'delimiter','\t','precision','%8.6E');
```

calcgrad.m